UNIVERSITY OF OKLAHOMA

GRADUATE COLLEGE

INVESTIGATION OF DESIGNS FOR TUNING OF MUTUAL COUPLING AND OPERATING FREQUENCY IN HIGH-POWER SLOT ANTENNA ARRAYS

A THESIS

SUBMITTED TO THE GRADUATE FACULTY

in partial fulfillment of the requirements for the

Degree of

MASTER OF SCIENCE

By

ANDREW SCHAEFFER
Norman, Oklahoma
2020

INVESTIGATION OF DESIGNS FOR TUNING OF MUTUAL COUPLING AND OPERATING FREQUENCY IN HIGH-POWER SLOT ANTENNA ARRAYS

A THESIS APPROVED FOR THE
SCHOOL OF ELECTRICAL AND COMPUTER ENGINEERING

BY THE COMMITTEE CONSISTING OF

Dr. Jessica Ruyle, Chair

Dr. Shahrokh Saeedi

Dr. Hjalti Sigmarsson

© Copyright by ANDREW SCHAEFFER 2020
All Rights Reserved.

Table of Contents

List of Tables

List of Figures

Abstract

Today's congested frequency spectrum calls for frequency agile arrays and antennas that can avoid the interference of the myriad of RF sources, from satellites to amateur radio, that take up the same bandwidths. Previous work has been done developing tunable slot antennas for this purpose using varactor tuning methods, but a high power tunable slot array has not yet been developed.

This thesis presents work aimed at enabling the creation of this high-power tunable slot array. The development of a miniaturized coplanar waveguide to slotline transition and the simulation of several tunable antenna designs are intended to enable frequency tuning in the array at the element level. The transition is based off of previously developed coplanar waveguide to slotline transitions, but will also be miniaturized to achieve easier implementation into the tunable slot array. This transition will also be used to investigate the effects of different loading mechanisms on the slots, based on a previous tunable slot design. The mutual coupling behavior of a two-element tunable slot array is investigated and a method of tuning the mutual coupling between these tunable slots is developed. From there, a transmission line model of this coupling mechanism is created to aid in further understanding of the design and achieve better understanding of the process of mutual coupling in tunable slot arrays.

Chapter 1

Introduction

Today's frequency spectrum is congested due to a wide variety of applications, from mobile signals to amateur radio [1]. In order to navigate this landscape, antenna arrays must have some form of tuning to avoid in-use frequencies to prevent interference. This thesis discusses several projects designed to work towards the goal of a high-power-capable, tunable slot antenna array equipped to navigate this frequency spectrum. These projects include a slotline to coplanar waveguide transition for use in tunable antennas (and potentially other array applications), as well as its miniaturization, several tunable antenna designs meant to increase understanding of the cavity loading behavior of slot antennas, and a method for tuning the mutual coupling between slot antenna elements in a phased array, as well as a circuit model for this design.

Previous work established the ability to tune the resonant frequency of a slot antenna using a varactor-based setup [2]. The original design exhibited tuning from 1.65 GHz to 2.9 GHz and maintained radiation efficiency above 50% across its frequency tuning band. However, varactors (the main tuning method for this design) typically operate from 1 mW to 1000 mW of power, and power levels significantly higher than that cause the varactors to exhibit distortion due to nonlinear behavior, potentially even causing breakdown of the varactor [3]. This behavior, and these power handling levels, is insufficient for the 50 W of power handling needed for the tunable slot array. Thus, a tuning method with higher power

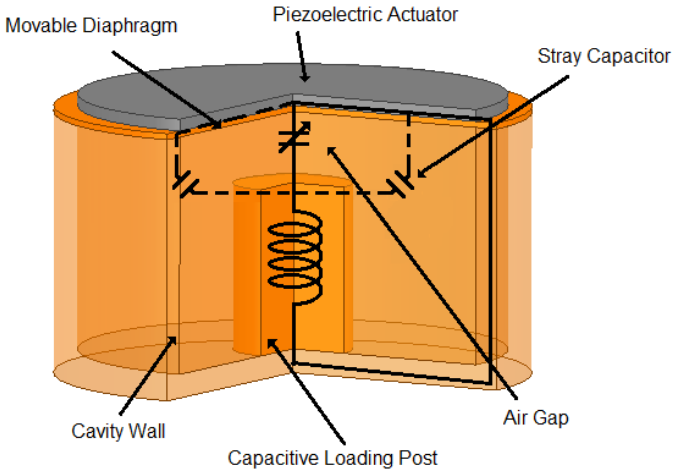

Figure 1.1: The tunable cavity resonator proposed for use in high-power tunable slot array applications [6].

handling capabilities was needed.

A tunable cavity resonator that exhibited power handling of over 26 W (with theorized handling of up to 50 W) from 3 GHz to 3.6 GHz had already been developed and can be seen in Figure 1.1 [4]. This cavity could replace the varactors in the original design as the slot's tuning mechanism with a device capable of handling higher power, with a few adjustments in terms of connection to the slot, with the cavity also having the capability of tuning across S-band [5]. The cavity's resonant frequency can be tuned using an adjustable gap distance between a center post in the cavity and the top of the cavity. This gap could be changed using a piezoelectric mechanism on the top of the cavity. By flexing the ceiling of the cavity, the change in gap size led to a change in the cavity's capacitance. Using this cavity as a load on a slot antenna would allow tuning across S-band by using this changing capacitance to load the slot.

Adjustments were made to the cavity dimensions and the cavity was connected to a slot antenna using slotline to create a frequency agile antenna. This antenna can be seen in Figure 1.2 [7]. This antenna was capable of tuning from 1.75 GHz to 3.67 GHz with a

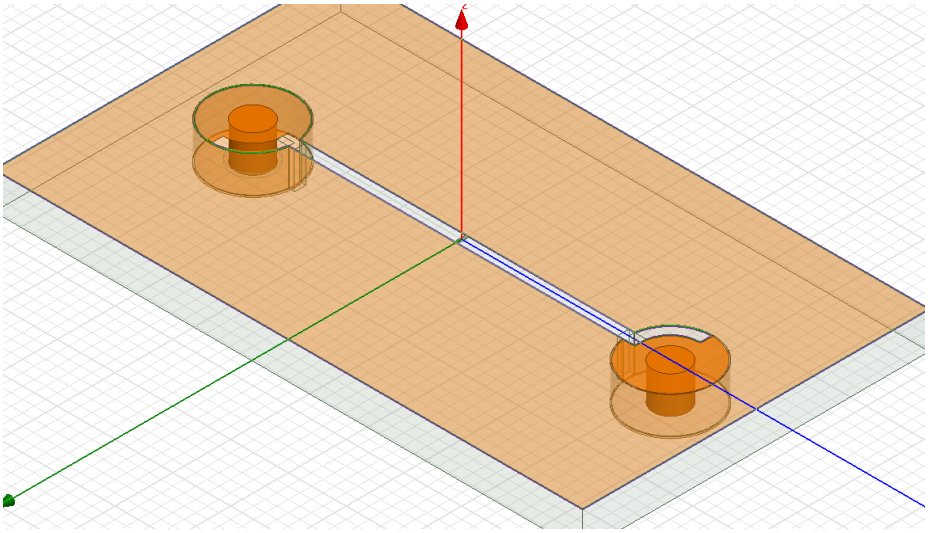

Figure 1.2: A previously developed frequency-agile antenna design that utilizes slotline coupling between the slot antenna and the cavity resonator from [7].

capacitive gap swing of 40 μm, covering almost all of S-band. However, this antenna had significant issues with radiation efficiency. The efficiency stayed above 90% across S-band except at the antenna resonance, where it dropped down to less than 20% efficiency. This behavior can be seen in Figure 1.3 (note that the traces are coarse and these dips likely extend lower than the displayed value). In order to try and fix this radiation efficiency issue, it was theorized that a different method of coupling between the slot and the cavity resonator was needed.

In order to fully understand the effects going on with this antenna, the basics of slot behavior need to be discussed. The theory of slot antennas is based on Booker's extension of Babinet's Principle, which states that the addition of the light pattern left by a screen with a cutout and the light pattern by the inverse of that screen gives a pattern the same as if there were no screen to begin with [8]. Booker's extension included polarization, making the principle more applicable to RF applications. A consequence of Booker's work was the development of the slot antenna. This antenna is, in its base physical shape, a shape cut out of a ground plane intended to radiate [9]. This type of antenna can be understood

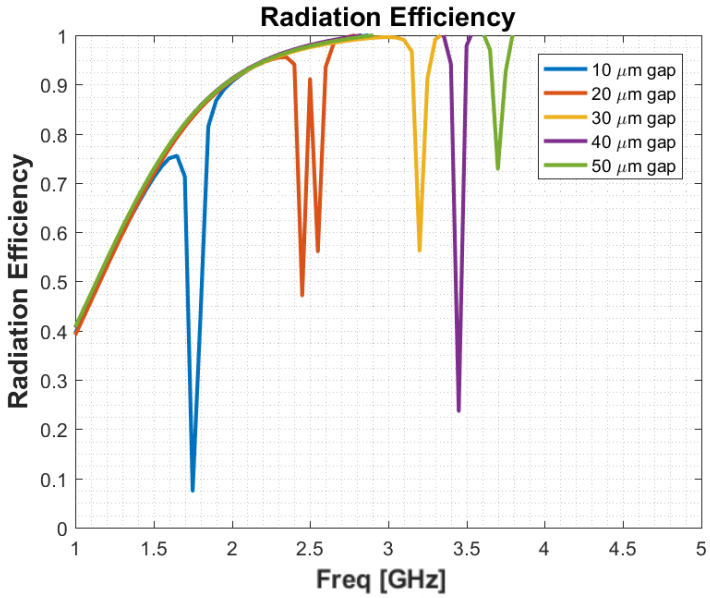

Figure 1.3: The radiation efficiency response of the slotline loaded tunable slot; The radiation efficiency has a null at the antenna resonance, preventing the design from radiating as desired.

through Booker's work as the dual of a dipole antenna. The slot antenna effectively 'fills the spaces' the dipole antenna leaves, as described with Babinet's Principle. This results in the slot radiating in an 'opposite' manner to the dipole: the electric field behavior of the slot closely matches the magnetic field behavior of the dipole, and vice versa. This results in an effective antenna that has the added benefit of being easily implemented into devices, as it can be cut out of most metal surfaces on an object. This is especially useful for implementation into waveguide structures. For more context on the slot antenna and its implementation, Figure 1.4 shows the typical feeding method of the slot, and Figure 1.5 shows the currents on a slot operating in its first mode [9].

The cavity behavior also needs to be discussed to explain how it can load the slot antenna. By attaching the cavity to the slot antenna, a shunt RLC element can effectively be introduced. This load can adjust the effective length of the antenna, allowing it to radiate at a frequency other than the one the physical dimensions naturally radiate at. The basic

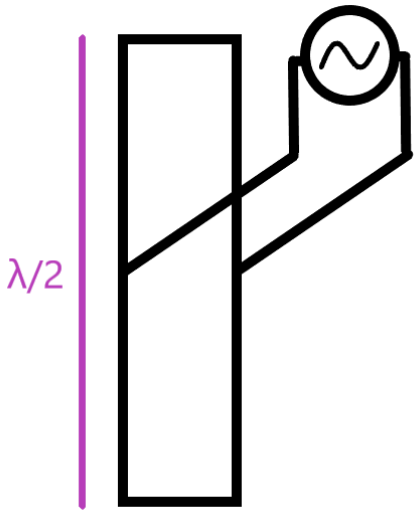

Figure 1.4: The feed location on the slot

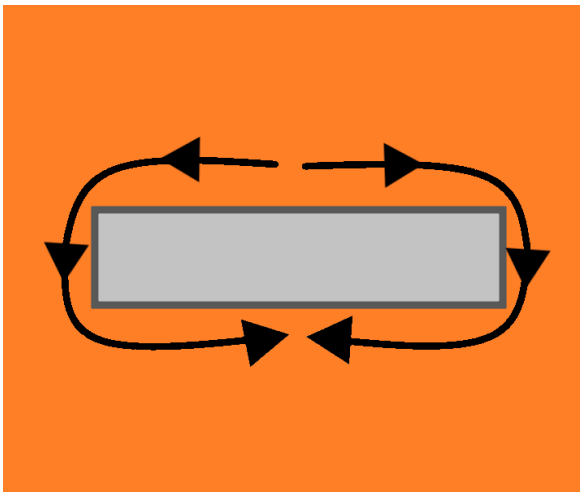

Figure 1.5: The currents on the slot

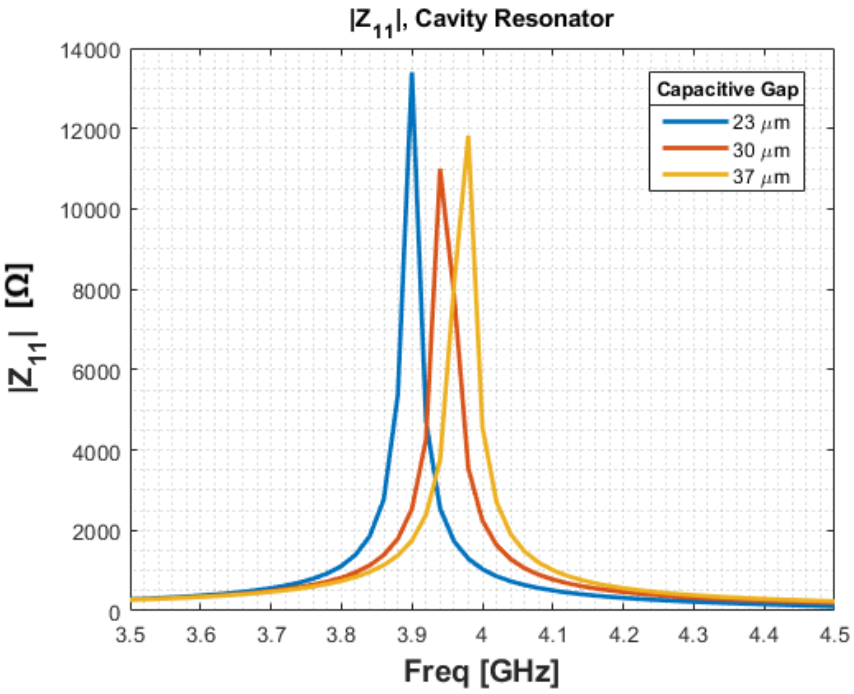

Figure 1.6: The cavity resonator tuning input impedance

behavior of the cavity can be seen when looking back at Figure 1.1. Between the center post and the piezoelectric ceiling of the cavity, a capacitance is produced, while the length of the center post produces an inductance. Coupling into this cavity and looking at the input impedance of the cavity in Figure 1.6 shows that this causes the cavity to act as a tunable load, with the changing gap width between the top of the cavity and the post changing the input impedance seen by the slot.

Coplanar waveguide had already been shown to be a viable method of coupling into the cavity [10], but was not able to couple directly into the end of the slot antenna. However, as previously shown, slotline was able to couple directly into the end of the slot, so a coplanar waveguide to slotline transition was necessary for transitioning between the slotline and the coplanar waveguide. These transitions also, ideally, needed to be planar to avoid fabrication issues once the tunable slot was to be expanded into a full tunable array. This transition is investigated in Chapter 2 of this thesis, with implementation of this transition into a tunable

slot discussed in Chapter 3.

Initial investigation into transition methods yielded several designs, the first of which involved the use of a circular stub on one end of the coplanar waveguide [11]. This stub shifted the phase of the signal on one side of the coplanar waveguide or slotline, allowing for transition between the two with minimal loss. This design was shown to have losses of less than approximately 2 dB across S-band [11]. The maximum transmission loss allowed for use in the tunable antenna was 3 dB, corresponding to at least half of the input power being transmitted through the transition, with the preferred loss being less than 1 dB, corresponding to more than 90% of the power being transmitted.

Previous work used coplanar waveguide to feed slot antennas and hollow patch antennas, which could potentially be used to either achieve a low-loss coplanar waveguide to slotline transition or to bypass the need for a coplanar waveguide to slotline transition by directly coupling to both the slot antenna and cavity using coplanar waveguide [12], [13].

After this transition was developed and implemented into a tunable slot, the slots needed to be simulated as an array, as the goal of the overall project was to eventually produce a phased array of high-power capable, tunable slot antennas. With this array, issues developed that individual slot elements did not have to face, namely mutual coupling between slot antennas. In phased arrays, antenna elements can couple into one another (whether through surface waves, radiation, or direct coupling), leading to signal cancellation and producing a phenomenon called scan blindness. This leads to blind angles in detection, preventing the array from functioning as needed by missing detections or losing tracking targets. In order to fix this, especially in a tunable slot array, a method of tuning mutual coupling to avoid this behavior is needed.

Previous work on tuning mutual coupling between array elements dealt primarily with patch antenna arrays [14], [15]. These arrays made use of tunable baffles, which are structures located between array elements that affect the coupling between the elements, typi-

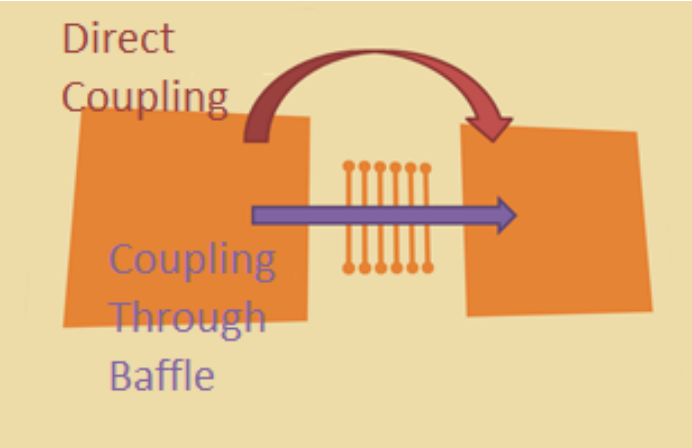

Figure 1.7: A tunable baffle design for mutual coupling tuning in patch antennas, adapted from [14].

cally by changing the effective distance between the antennas to put them at an apparent half wavelength apart. An example of this design can be seen in Figure 1.7. This distance minimizes mutual coupling, and as such is very desirable for arrays. However, these designs were designed for static patch antenna arrays, so new structures need to be developed for an array of tunable slot antennas.

This thesis will first discuss a coplanar waveguide to slotline transition and its miniaturization in Chapter 2. Then, this transition will be implemented into two simulated tunable antenna designs in Chapter 3, along with another tunable antenna design. In Chapter 4, focus will move away from an element level and shift to an array level, discussing a novel mutual coupling tuning mechanism for tunable slot antennas. Then, Chapter 5 will discuss a transmission line model for the mutual coupling tuning mechanism. First, the slotline to coplanar waveguide transition needs to be investigated.

Chapter 2

Coplanar Waveguide Coupling

2.1 Introduction

The initial challenge with developing a working, tunable, high-power slot antenna was dealing with the significant reduction in radiation efficiency at the operating frequency that previous designs had seen [7]. This issue was preventing the tunable slot element from being useful as an antenna element, and as such would not be suitable for use in an array. The suspected cause of these radiation efficiency dips for the end-loaded slot design was the current path in Figure 2.1 that acted as a short across the slotline, so a different method of connecting to the cavity was needed. There had been work with the tunable cavity resonator that had shown that coplanar waveguide was capable of coupling into the cavity, but in order to accomplish that, a method of transitioning between slotline and coplanar waveguide was necessary [10].

2.1.1 Balanced and Unbalanced Transmission Lines

Coplanar waveguide and slotline are not capable of directly connecting to each other without any sort of transition structure. This is because slotline is a balanced transmission line, while coplanar waveguide is an unbalanced transmission line. Balanced transmission lines have the same density of current on both the signal and ground areas of the trans-

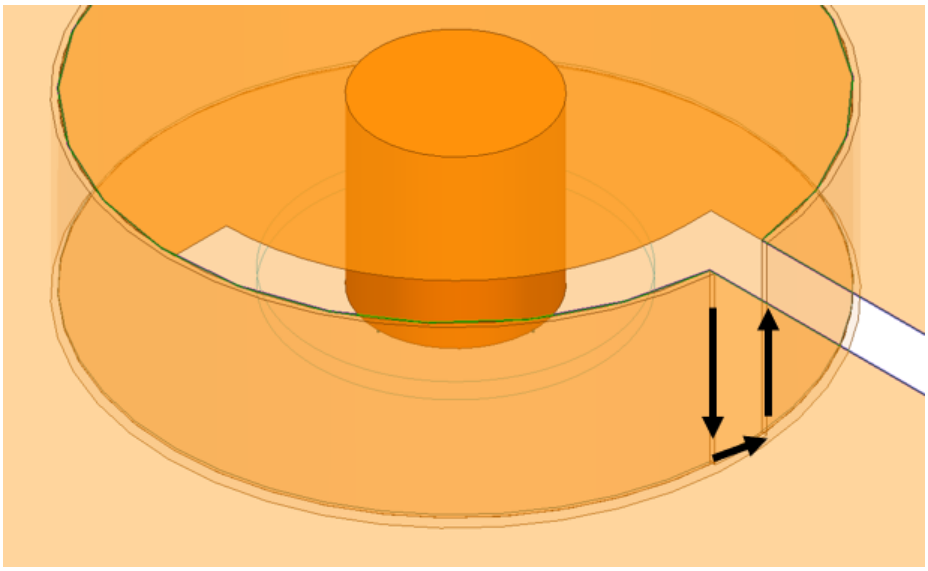

Figure 2.1: A short found in the previous tunable slot antenna design across the connecting slotline through the cavity wall; This was the initial theory for the cause of the dip in radiation efficiency at resonance.

mission line, but each with a 180 degree shift in phase from the other, seen with slotline in Figure 2.2. Unbalanced transmission lines do not have the same current density on the signal and ground portions of the transmission line, as seen with coplanar waveguide in Figure 2.3, because the current is equal, but the current paths for the ground (in the case of coplanar waveguide) are more numerous. These differences in current density patterns on the transmission lines prevent direct transition from one line to another, and as such typically require a balun, a structure designed to transition between balanced and unbalanced transmission lines, in order to avoid significant transmission loss.

With coplanar waveguide to slotline specifically, the losses between the two transmission lines comes from the side of the coplanar waveguide that is not directly connected to the slotline. Current cancellation at this point in the transition, due to the opposite phases of the signal from the coplanar waveguide and the slotline, increases transmission loss. This current interaction can be seen in Figure 2.4. The current paths from the top line of the coplanar waveguide counteract the current paths from the slotline, yielding current

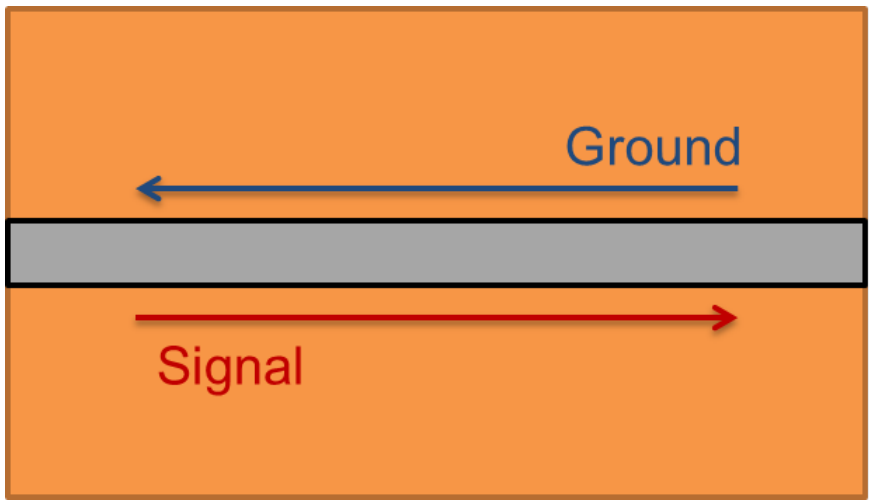

Figure 2.2: The balanced current paths on slotline; Both the signal and ground paths are essentially the same (just on different sides of the transmission line and 180 degrees out of phase from each other), so the current densities are the same.

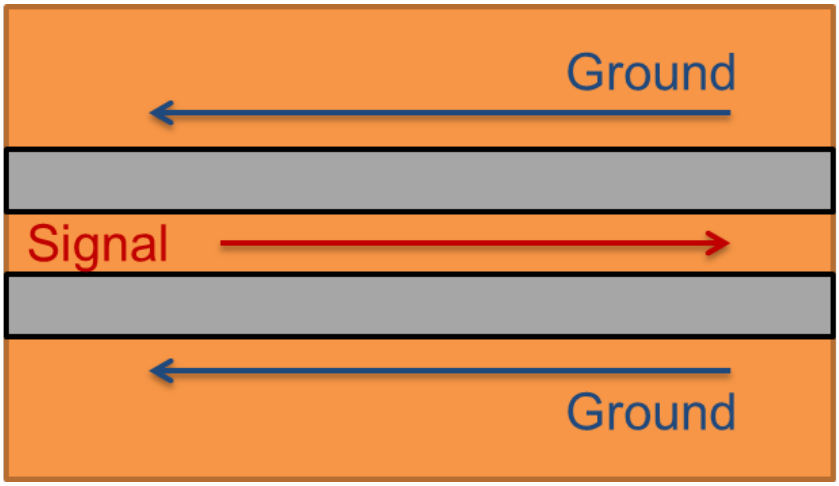

Figure 2.3: The unbalanced current paths on coplanar waveguide; There are more current paths for the ground of the coplanar waveguide with the same current as the signal line, thus the ground has a lower current density.

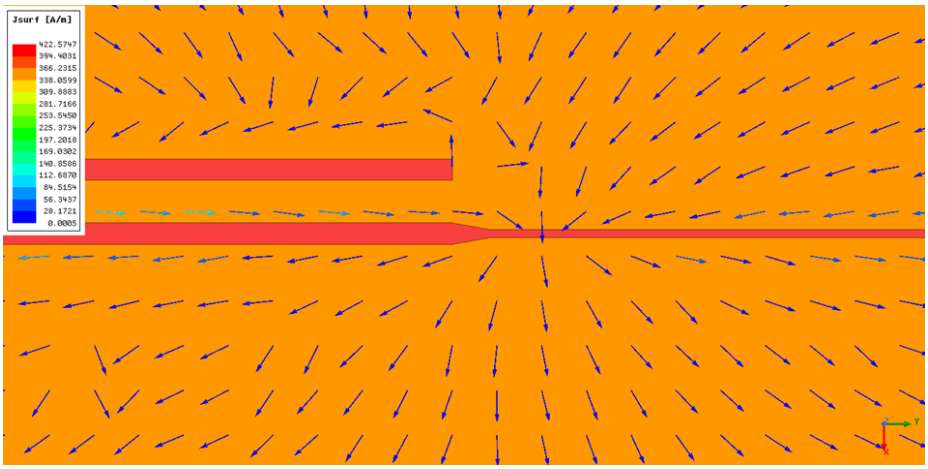

Figure 2.4: Conflicting currents when directly connecting coplanar waveguide to slotline; This prevents direct transition and necessitates a balun structure to pass power from the unbalanced coplanar waveguide to the balanced slotline.

cancellation.

2.2 Bent Coplanar Waveguide to Slotline Transition

2.2.1 Design and Simulation

The easiest way to fix this current cancellation issue is by shifting the phase of the current coming off of the coplanar waveguide to match the phase of the current on the slotline. This can be accomplished with a stub, as seen with the first simulated design [11]. This structure used a circular stub coming off of one side of the coplanar waveguide (see Figure 2.5), with the other side of the coplanar waveguide coupling directly into the slotline. Reconstructing this design in HFSS resulted in less than 3 dB of loss across S-band. This can be seen in Figure 2.6. At 3 dB of loss, half of the power provided to one end of the transition (either the slotline or the coplanar waveguide) is able to transmit from one transmission line to the other, which was necessary for properly coupling between the slot antenna and the cavity in later implementation. It is also important to note that the simulated design involved

two transitions back to back (from coplanar waveguide to slotline and back to coplanar waveguide), as HFSS can experience issues with using waveports on slotline. The ports for all of these simulations are at the ends of the coplanar waveguide connected to each respective transition, and ports one and two can be defined in either direction due to the symmetry of the design. However, this design required the edges of the ground plane to be relatively close to the transition, otherwise the response in Figure 2.7 would emerge with a peak in transmission loss within the 2 GHz to 4 GHz band. This transition's ground plane was 100 mm long, which is equal to a wavelength at 3 GHz (chosen because it was the center of the desired frequency band), while the original was 15 mm on the side parallel to the coplanar waveguide by 7 mm on the side parallel to the slotline. This bent design was also simulated when the transmission line widths were scaled up to the size in Figure 2.8 in order to connect to the cavity and slot antenna without needing large tapering of the lines. When this scaled design was simulated, it also had transmission problems, with losses over 14 dB around 3.4 GHz. This can be seen in Figure 2.9. This would not work for the tunable slot, as it would severely limit the ability for the antenna to properly couple to the cavity, limiting tuning range.

2.2.2 Loss Analysis

The reason for the loss in the larger transition needed to be analyzed. Looking at the S_{11} in Figure 2.10, it could be seen that there was some reflection around the same frequency as the main dip in S_{21}. Checking the impedances of both the slotline and the coplanar waveguide, it could be seen that the coplanar waveguide had an impedance of 50 Ω while the slotline had an impedance of 90 Ω. This was a significant contributor to the loss experienced in the transition. However, there was a much larger portion of the loss that was being radiated by the transition. The radiated power for 1 W of input power can be seen in

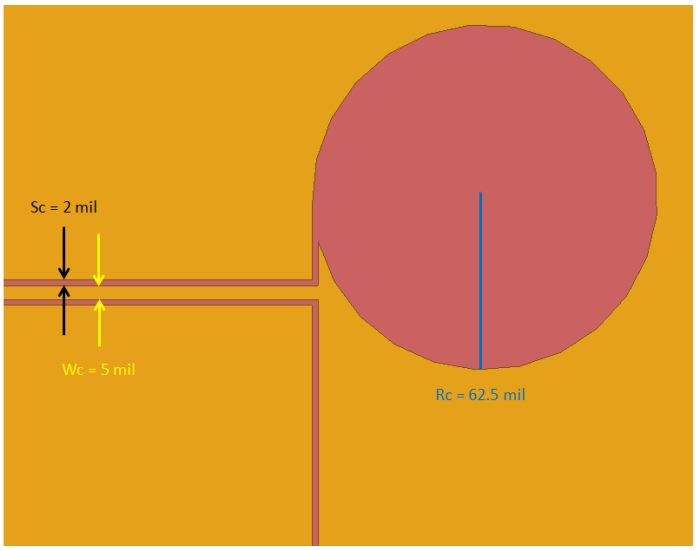

Figure 2.5: The first transition design based on [11]; This structure uses the circular stub to shift the phase of the current on one side of the coplanar waveguide to match the phase of the slotline.

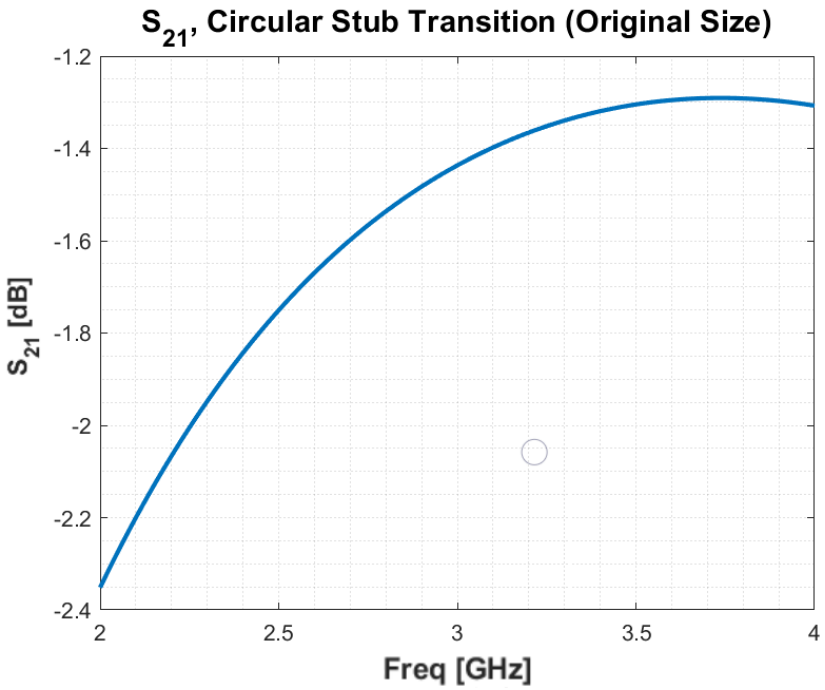

Figure 2.6: The S_{21} of the design from [11]; This matches up with the results of the paper and allows for over half of the input power to properly transition from one transmission line type to the other.

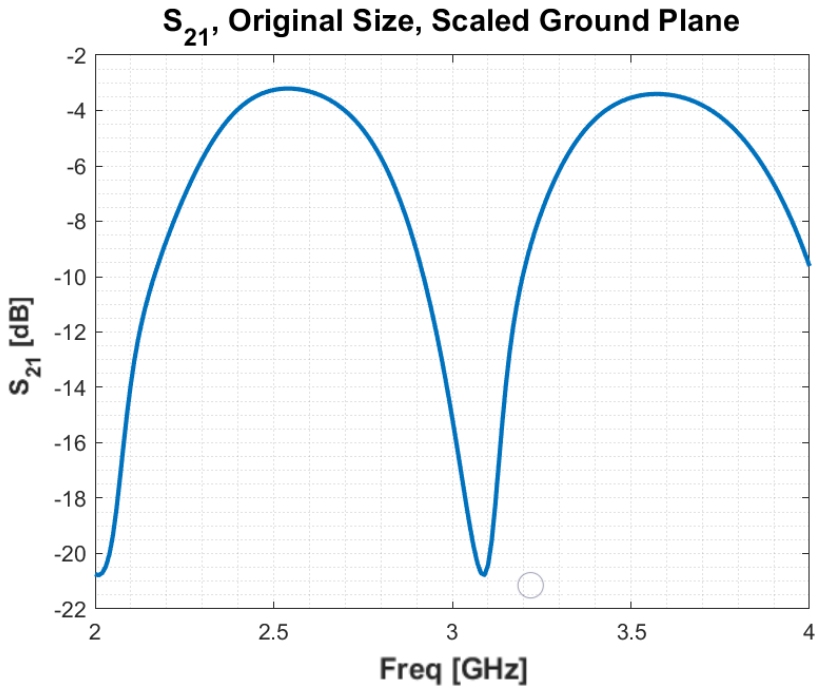

Figure 2.7: The S_{21} of the original design size with a scaled up ground plane

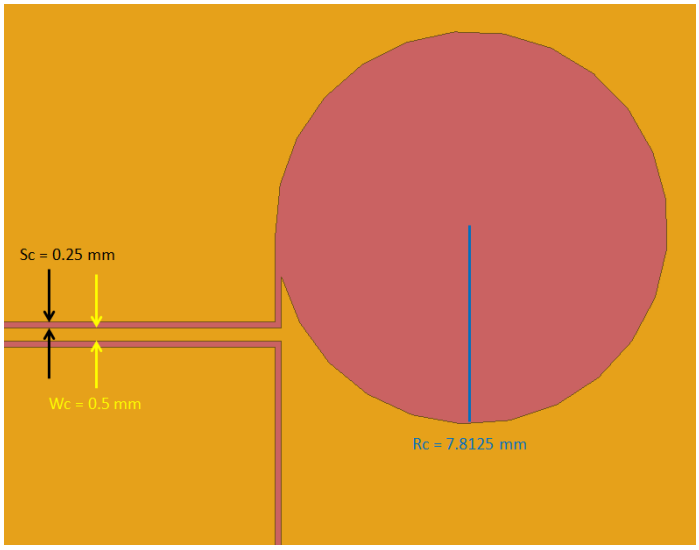

Figure 2.8: The dimensions of the same design scaled up to couple properly into the cavity resonator and the slot antenna without significant reflections; These are based on previous coplanar waveguide dimensions used with the cavity [10].

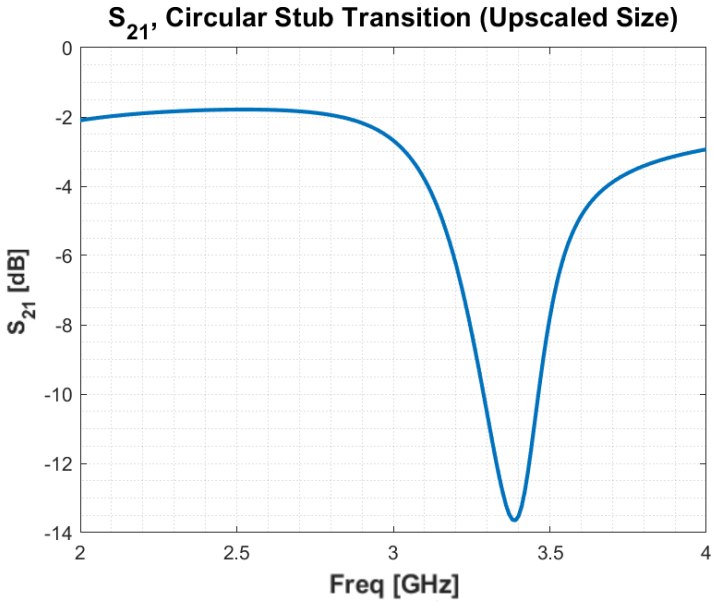

Figure 2.9: The S_{21} of the scaled design; The scaling of the parameters, as well as the adjustment of the ground plane size to one wavelength, causes a significant decrease in transmitted power that prevents this design from being functional as an S-band transition between the two transmission lines.

Figure 2.11. This high amount of power being radiated indicated that this was the major source of loss in the transition.

2.3 Straight-line Transition

2.3.1 Radial Stub Based, Straight-line Transition

The design seen in Figure 2.12 had a similar structure to the previous transition, but used a radial stub, rather than a circular stub, along a straight-line transition [16]. This design also included the addition of a jumper wire to connect the two sides of the ground plane across the coplanar waveguide. This design showed the response seen in Figure 2.13, managing less than 3 dB of loss across S-band. Both the coplanar waveguide and slotline were designed to operate with a characteristic impedance of 50 Ω, with the coplanar waveguide

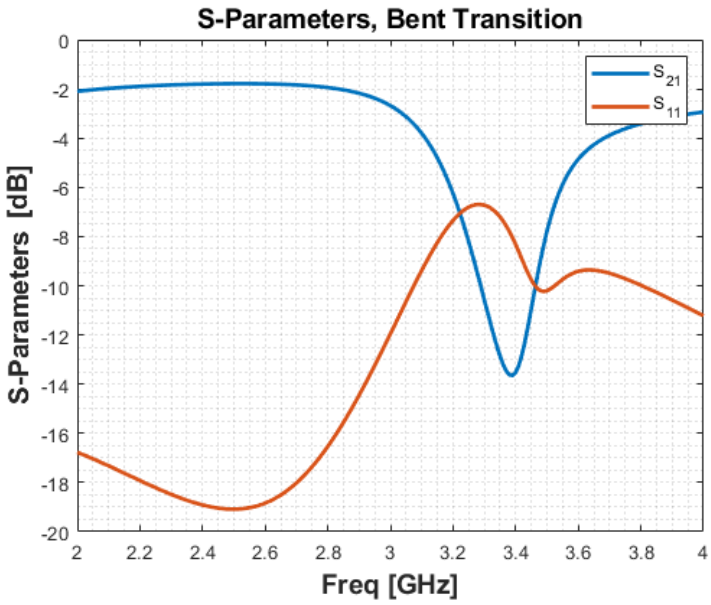

Figure 2.10: The S-Parameters of the transition; There is some loss across band and at the location in the dip in S_{21} due to mismatch between transmission line impedances.

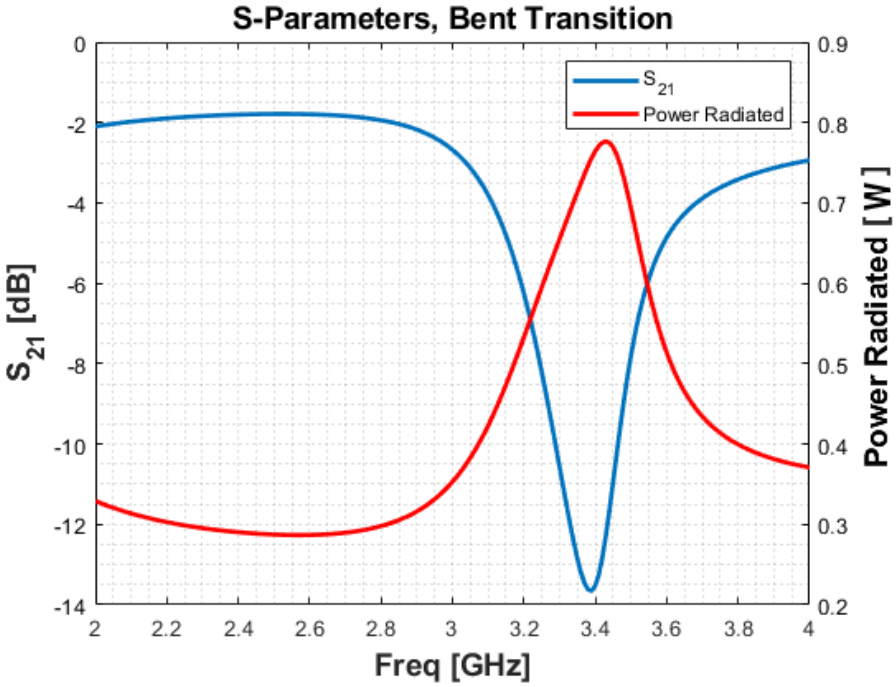

Figure 2.11: The radiated power with a peak at the same location as the dip in S_{21}

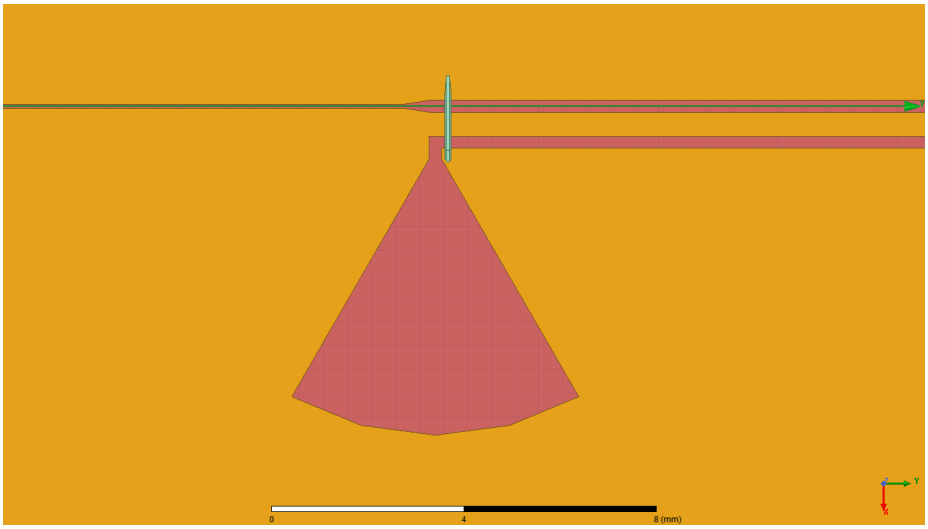

Figure 2.12: A radial-stub based straight-line design adapted from [16]

having a cutout width of 0.25 mm and a center strip width of 0.509 mm, and the slotline having a width of 0.059 mm.

Previous designs had also seen issues with increased loss as the length of the slotline between transitions increased, so the response of this design needed to be investigated as well. Fortunately, sweeping the length of the slotline with the straight-line design resulted in less than 3 dB of loss for all slotline lengths of up to $\lambda/4$. This can be seen in Figure 2.14. The reason for the shift in the frequency of the dip is explored further in the Null Analysis section (Section 2.3.3) later in this chapter.

2.3.2 Alternate Stub Shapes

After this design was shown to address the previous issues, several stub shapes were simulated to see if they were viable for the transition. Figure 2.15 and Figure 2.16 show this transition design with a circular and square-shaped stub, respectively. These gave a similar S_{21} response to the radial stub, indicating that the stub shape did not matter much for overall performance of the transition. These can be seen in Figure 2.17 for the circular stub and

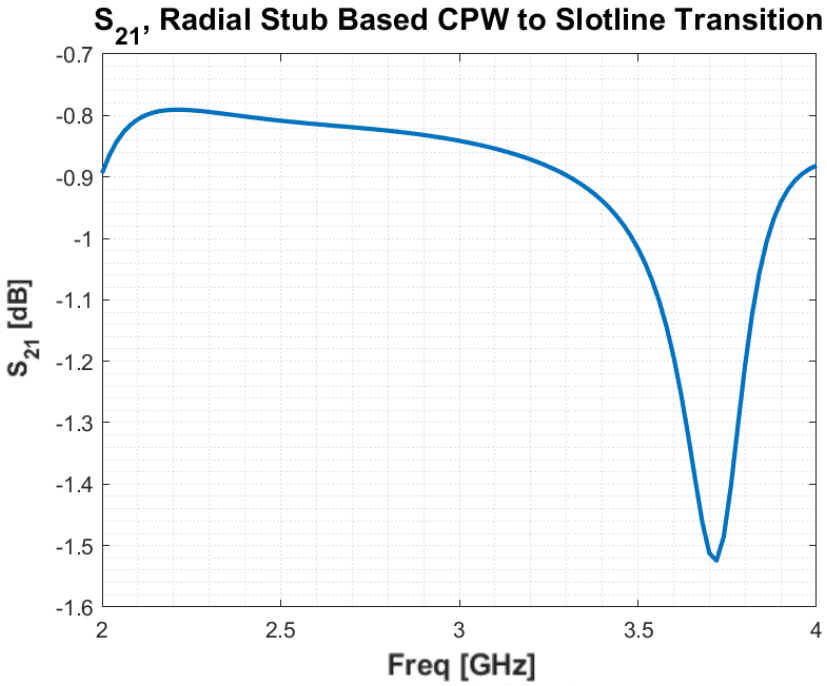

Figure 2.13: The S_{21} response of the radial-stub-based design; There is less than 2 dB of loss across S-band with this design, meaning more than 63% of the power is being transmitted through the transition.

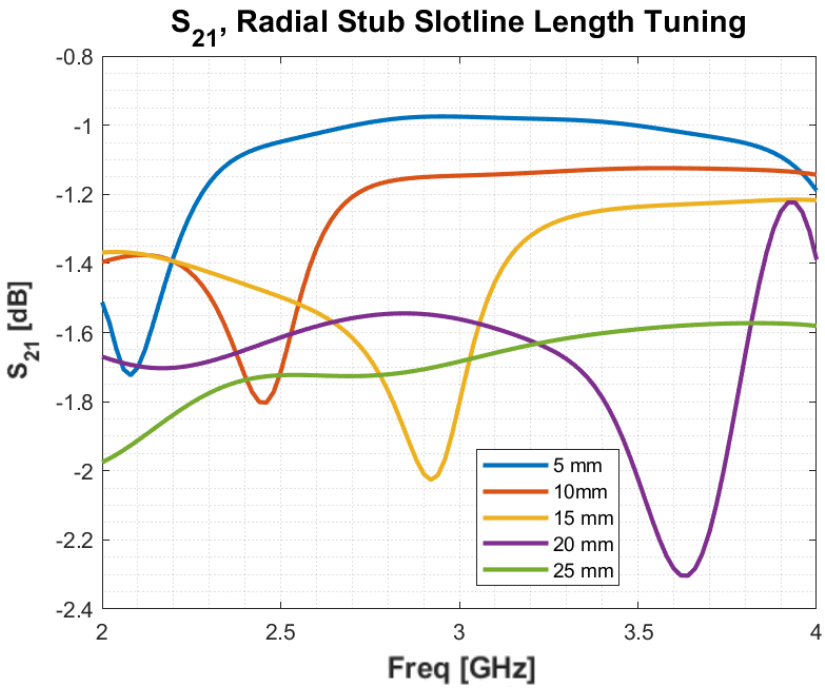

Figure 2.14: The changes in S_{21} as the slotline between transitions is lengthened; At all slotline lengths simulated, the transition maintained less than 3 dB of loss.

Figure 2.18 for the square stub.

2.3.3 Null Analysis

Looking at Figure 2.13, the transition seemed to work with less than a tenth of the power lost across the full 2 GHz to 4 GHz range except for a dip around 3.72 GHz. This dip was present in all simulated stub shapes, indicating that there was a consistent cause for the loss at this frequency. Initial suspicion pointed towards reflection within the transition, but the slotline and coplanar waveguide were matched at 50 Ω. Figure 2.19 shows the reflection of the transition, which lacks a peak in S_{11} that corresponds in frequency to the dip in S_{21}. This indicated that the reason for the loss was not reflection from the transition.

Next, the radiative properties of the transition were investigated. Looking at the radiated power in Figure 2.20, the transition is shown to be radiating power across S-band. For

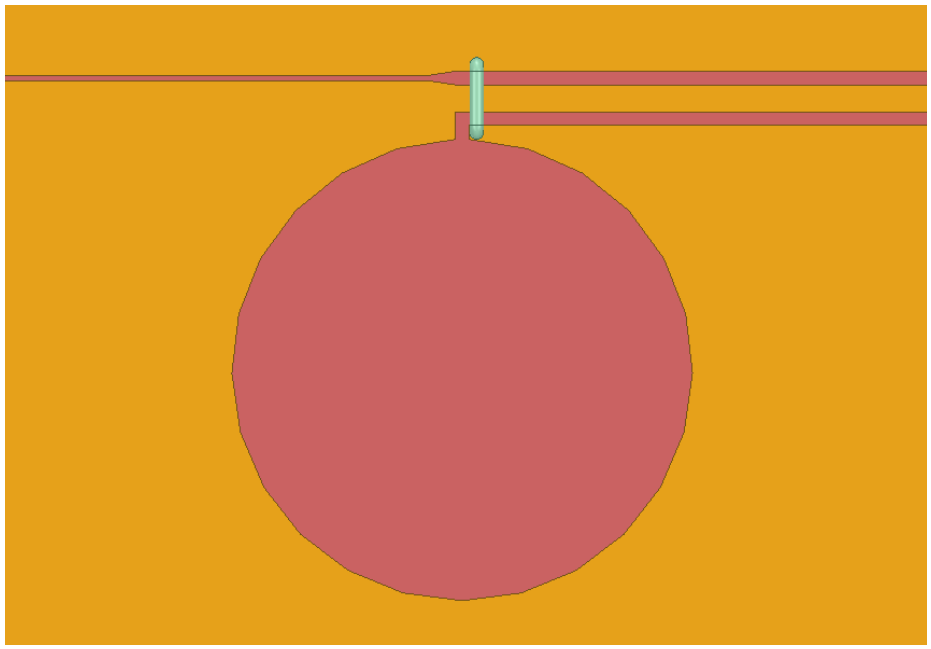

Figure 2.15: The straight-line coplanar waveguide to slotline transition with a circular stub

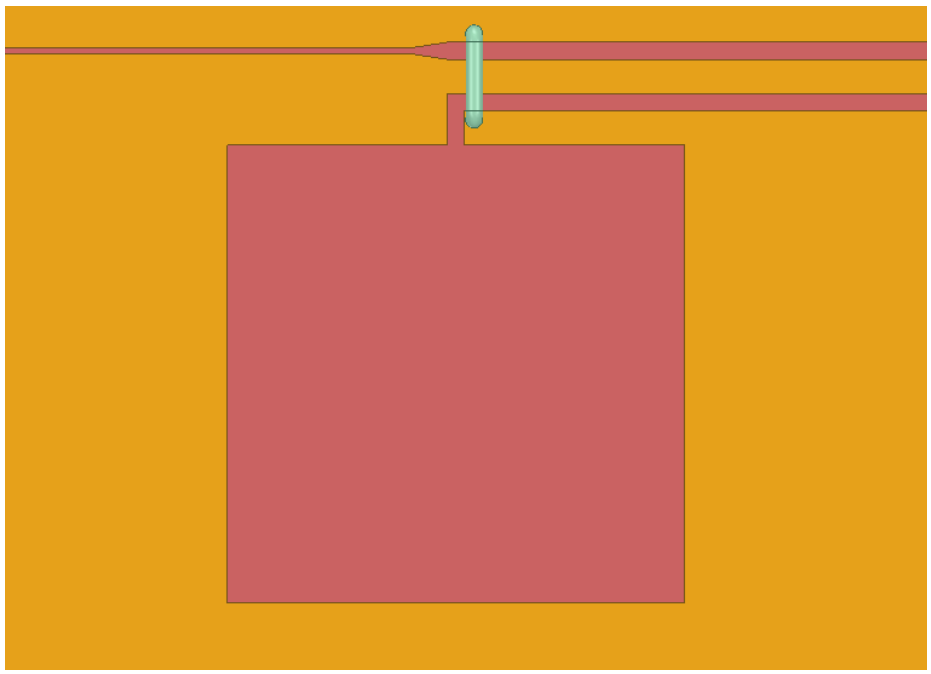

Figure 2.16: The straight-line coplanar waveguide to slotline transition with a square stub

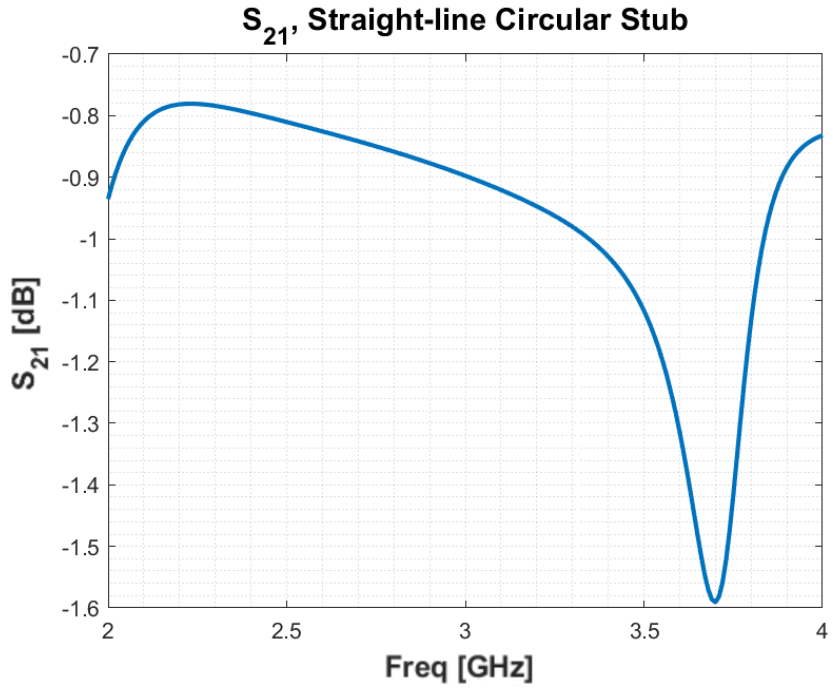

Figure 2.17: The S_{21} of the circular stub design; This design maintains less than 3 dB of loss across S-band.

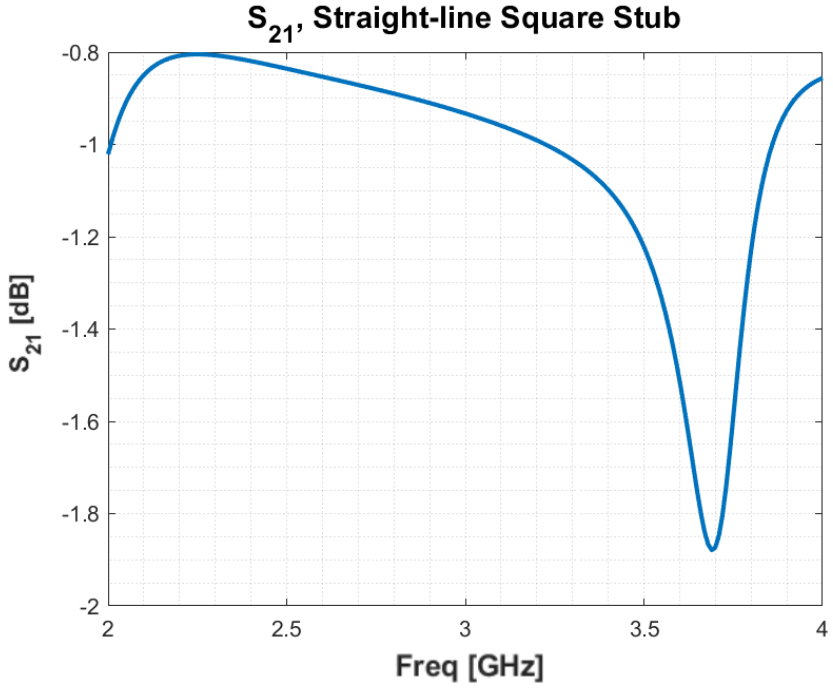

Figure 2.18: The S_{21} of the square stub design; This design maintains less than 3 dB of loss across S-band.

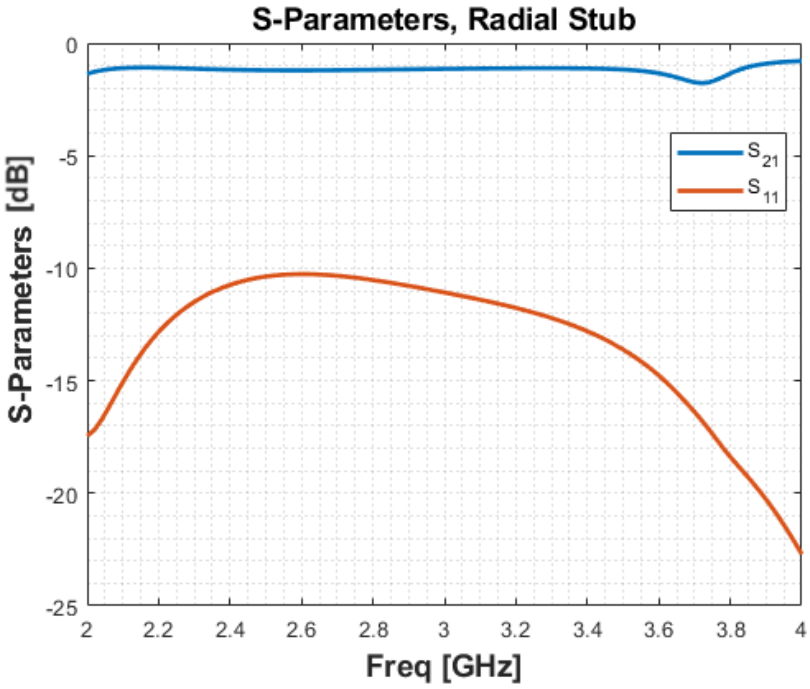

Figure 2.19: The S-Parameters of the radial stub design; It lacks a peak in S_{11} to match the dip in S_{21}, indicating that reflection is not the cause of the transmission loss.

most of the band, the radiated power was slightly less than 0.1 W. Because the power into port 1 of the transition was 1 W, this radiated power corresponded to the approximate 1 dB of transmission loss from 2 GHz to 4 GHz, with a peak in radiated power at 3.72 GHz, the same frequency as the dip in S_{21}. This indicated that something in the structure was radiating power, and looking at the electric fields on the structure in Figure 2.21 shows that the transition region is radiating, explaining the power loss in the transition. Looking at these fields, the behavior on each side of the coplanar waveguide is seen to be out of phase. This is due to common mode currents being excited on the coplanar waveguide, contributing to the radiative behavior of the transition. Thus, tuning the length of the coplanar waveguide changes the frequency of the dip in transmission. This makes sense with the results seen in Figure 2.14, as in order to tune the length of the slotline without changing the ground plane size, the length of the coplanar waveguide had to be changed as well. The frequency

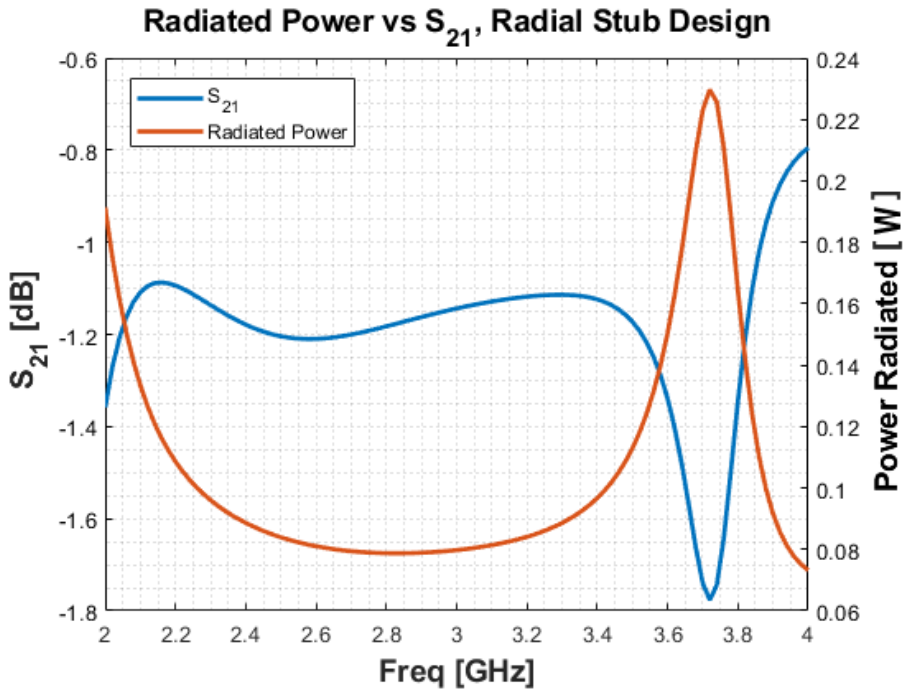

Figure 2.20: The radiated power of the straightline design; The peak in radiated power can be seen to line up with the dip in transmission,indicating that the loss in the transition was due to radiation from the transition structure.

decreased as the length of the slotline decreased, which is opposite the behavior that would be seen if the slotline was radiating. However, with this tuning, coplanar waveguide length is increasing, which does correspond to the behavior seen with the length tuning.

2.4 Stub Miniaturization

2.4.1 Radial Stub

The discoveries about the stub shape not significantly affecting the transmission loss of the transition indicated that the stub could be modified to reduce its size without increasing the transmission loss above 3 dB. This would allow the design to avoid any physical interference issues with other elements when put into an array later. These initial attempts at miniaturization used the radial stub design because it had the lowest transmission loss of

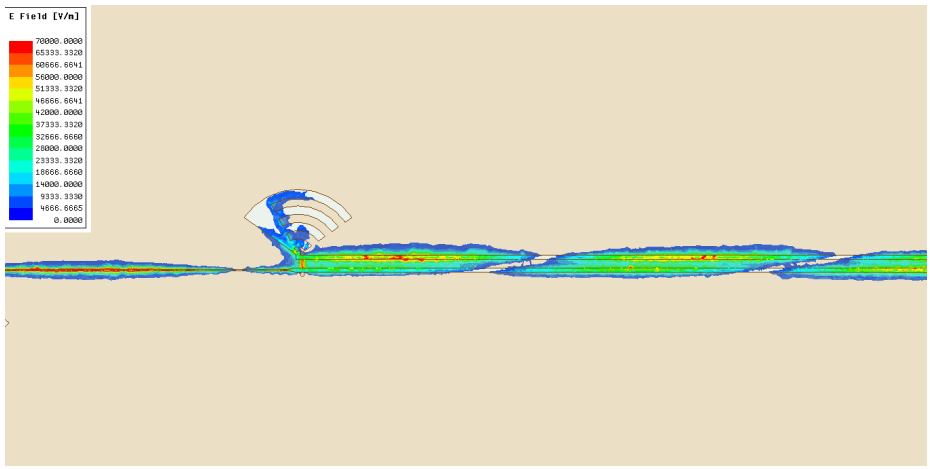

Figure 2.21: The electric fields along the straightline transition; The fields are out of phase between the sides of the coplanar waveguide, indicating the presence of common mode currents.

the three stub shapes.

The main method of miniaturizing the stub was to meander the perimeter. Because the stub was shifting the phase of the current to transition between coplanar waveguide and slotline, as long as the perimeter of the stub was maintained, the S_{21} remained about the same. The initial meandered radial stub from Figure 2.22 has the same perimeter as the non-meandered radial stub while reducing the radius. This design in particular managed to shrink the radius of the stub to 7.74 mm from 9 mm, a reduction of about 14%. Figure 2.23 shows that this modification did not significantly affect the S_{21} of the transition.

After the meandering was proven to be viable, the stub was meandered to the design seen in Figure 2.24, reducing the original stub radius of 9 mm by 55.88% to 3.97 mm. Figure 2.25 shows that the performance of this transition dropped slightly, from about 1.5 dB of loss to about 2.1 dB of loss. This slight increase in loss is likely due to current cancellation between the different cut-out sections of the 'comb-line' radial stub design, but the loss remained below 3 dB, which was acceptable for the transition.

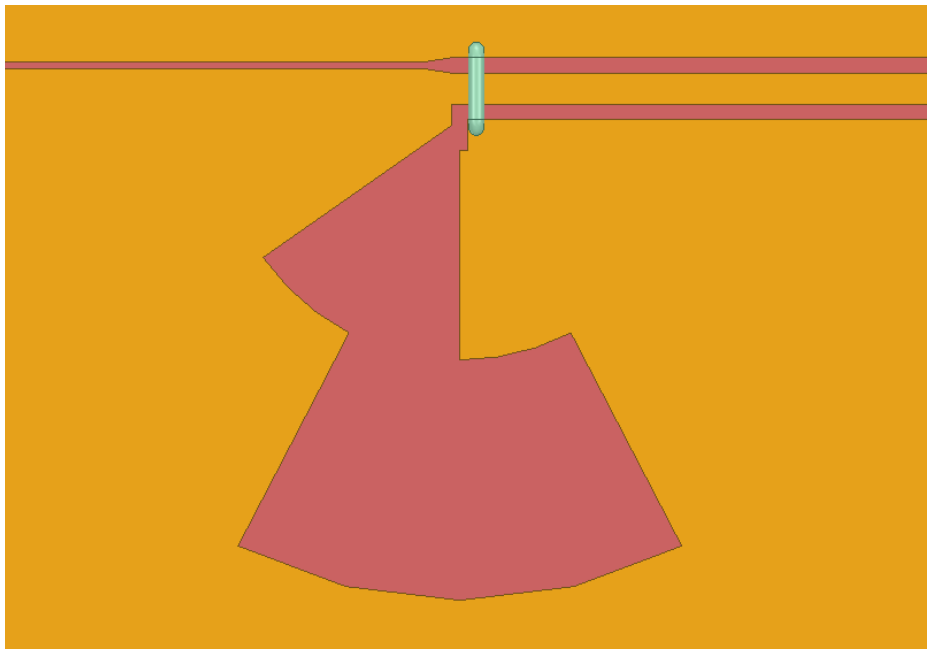

Figure 2.22: The shifted stub design; This radial stub has a radius of 7.74 mm, which is a 14% reduction in size from the original 9 mm stub.

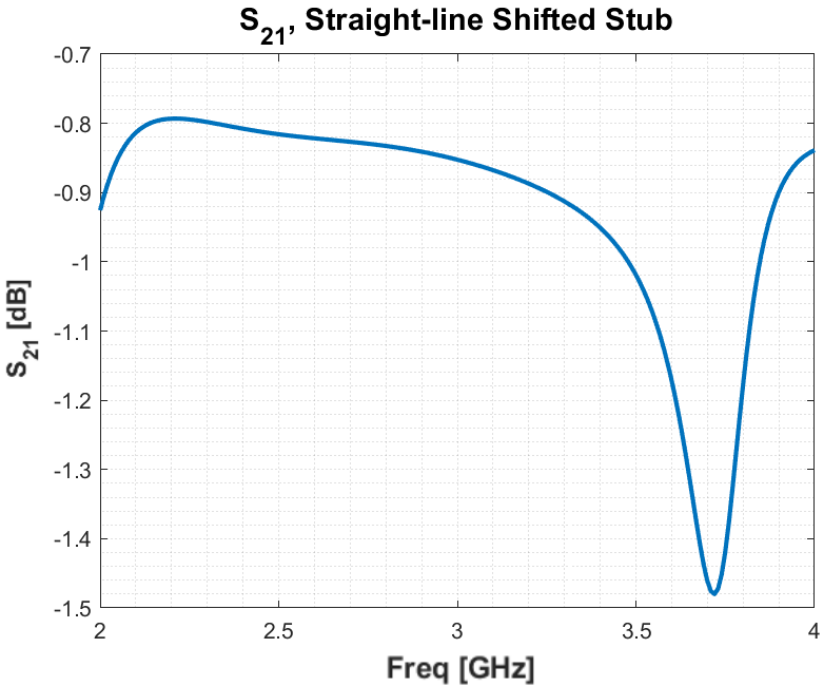

Figure 2.23: The S_{21} response of the first meandered radial stub; It maintains near-identical performance to the non-meandered radial stub.

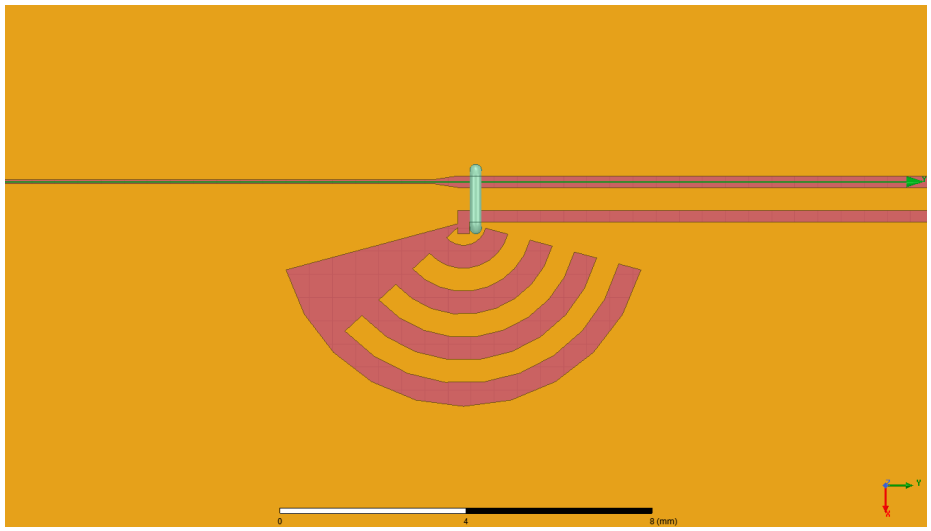

Figure 2.24: The final meandered design of the radial stub; This stub's radius is 3.97 mm, a 55.88% reduction in size from the original 9 mm stub.

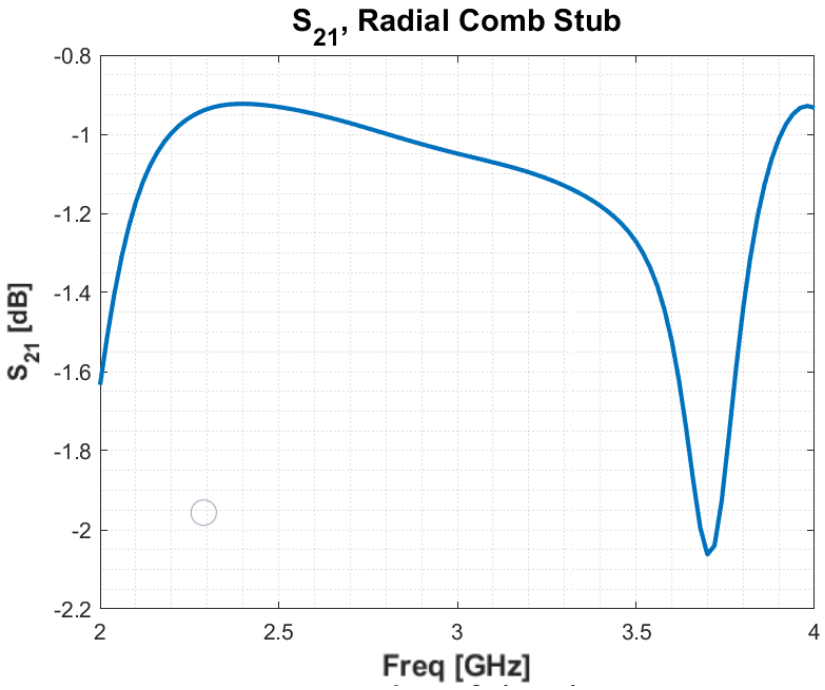

Figure 2.25: The S_{21} response of the final meandered radial stub; There is a slight increase in loss, about 0.5 dB, but the transition still maintains under 3 dB of loss.

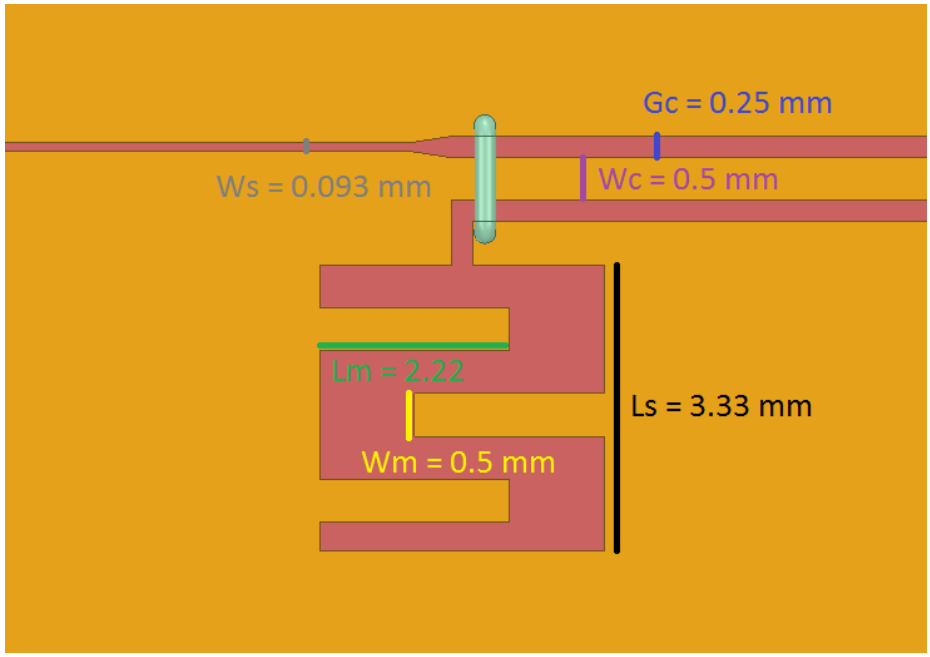

Figure 2.26: The meandered design of the square stub; This meandering reduced the side length of the square stub by 50% from 6.66 mm to 3.33 mm.

2.4.2 Other Stub Shapes

In order to verify that this method was useful for stubs in general rather than just radial stubs, the modified square stub seen in Figure 2.26 was also investigated. This stub reduced the length of the sides of the square by 50%, from 6.66 mm to 3.33 mm while yielding transmission losses of about 2.2 dB. This can be seen in Figure 2.27. This did have more loss than the larger square stub, which is likely due to current cancellations in a similar manner to the radial stub miniaturization, but is still effective as a transition between slotline and coplanar waveguide.

This result shows that meandering the perimeter of the stubs is possible for all stub shapes, not just radial stubs, making this method significantly more useful for miniaturizing these coplanar waveguide to slotline transitions.

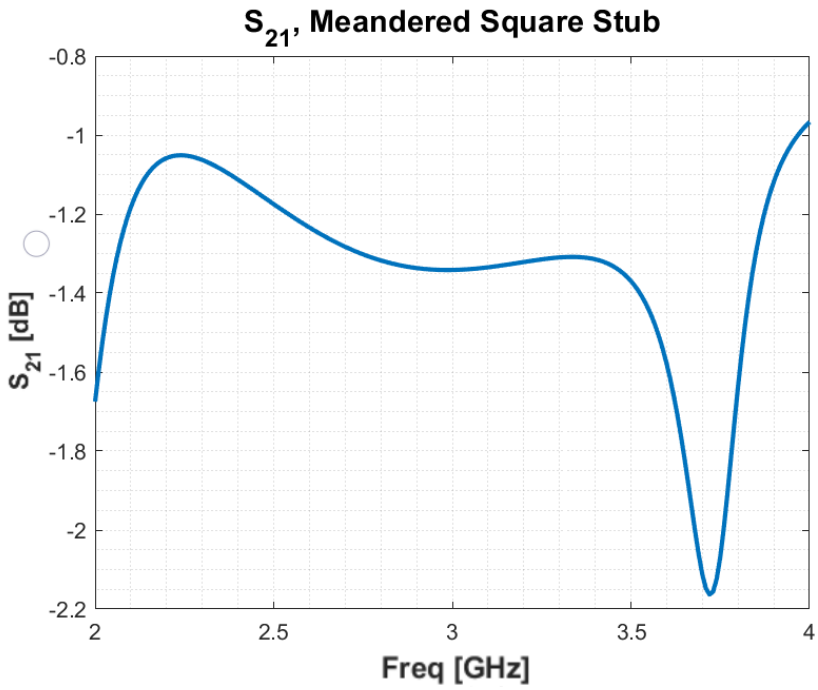

Figure 2.27: The S_{21} response of the meandered square stub; The loss is increased by about 0.3 dB with the meandered perimeter, but remains below 3 dB overall.

2.5 Comparisons

After all of these designs were simulated, comparisons could begin to be made between the different transition methods. Comparing the radial stub designs, both meandered and non-meandered gives insight into the effects of the meandering on the behavior of the transition. Figure 2.28 shows that the size reduction of the stub comes with some slight trade-offs in terms of both design and performance. Reducing the size of the stub decreases S_{21} by about 0.26 dB across two transitions. This phenomenon could be observed in the meandered square stub as well. Figure 2.29 shows the S_{11} of the transitions, which indicates that the reflection increases by meandering significantly, but reflection does not seem to be the main source of loss in any of these transitions.

The comparison between stub shapes yielded interesting results as well. Between the three transitions with a radial, circular, and square stub, with S_{21} of these designs compared

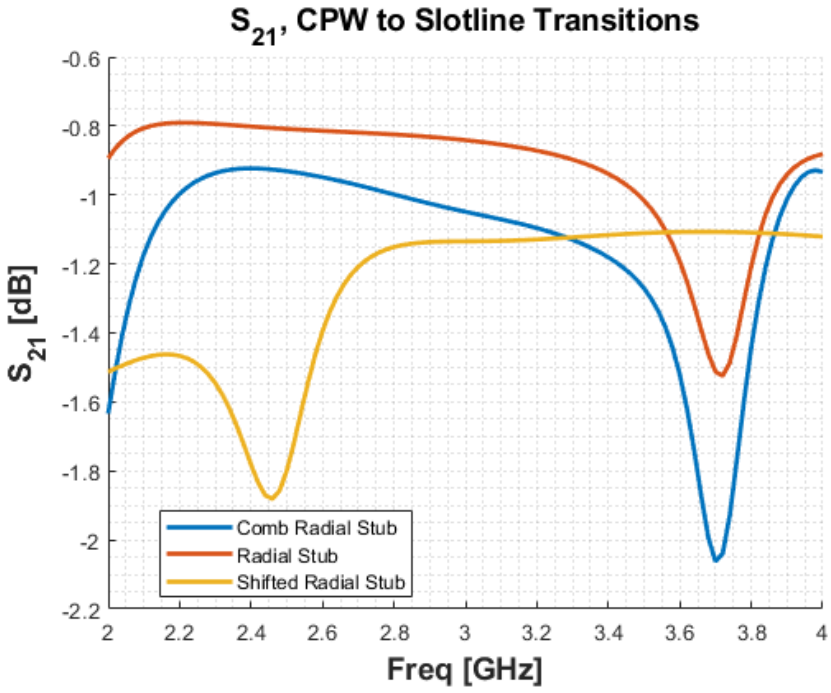

Figure 2.28: A comparison of the S_{21} of the original radial stub with the S_{21} of the meandered radial stubs

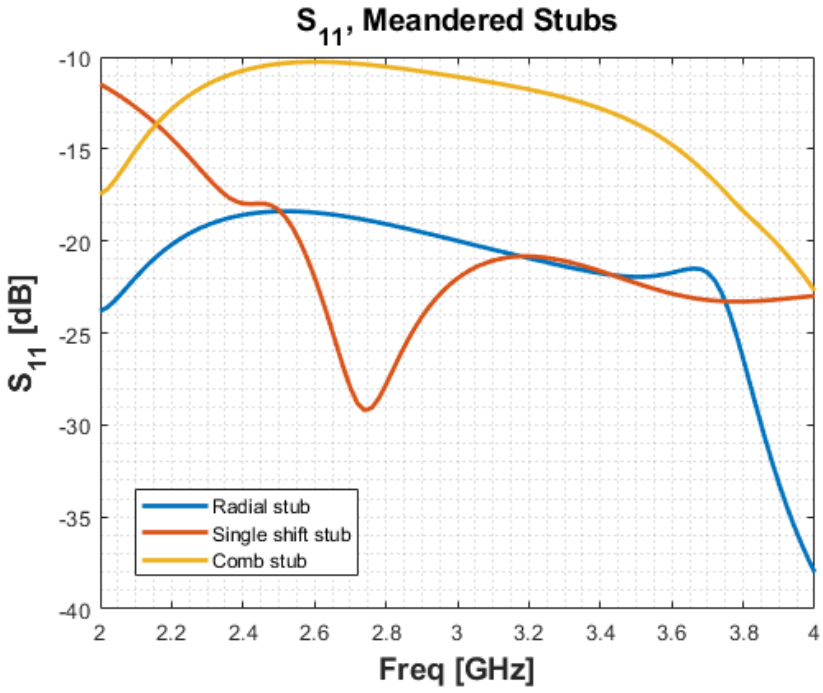

Figure 2.29: A comparison of the S_{11} of the original radial stub with the S_{11} of the meandered radial stubs

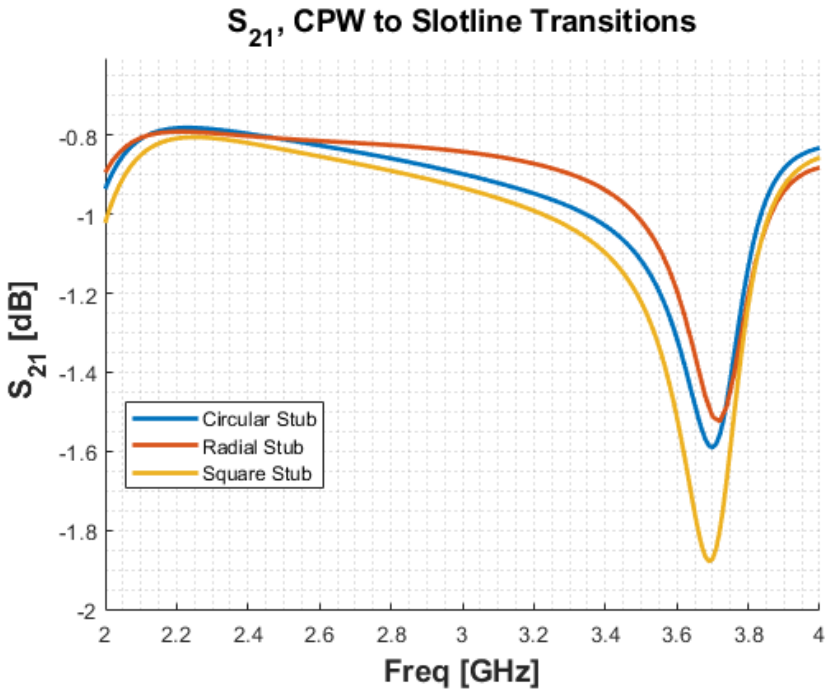

Figure 2.30: A comparison of the S_{21} of all the basic stub shapes

in Figure 2.30, there was some change in transmission loss between the transitions, with the circular and square stubs having greater loss than the radial stub, but all three designs remaining below 3 dB of loss. In fact, the greatest difference in transmission loss was 0.36 dB between the radial and square stubs. Figure 2.31 shows the S_{11} of the different transition shapes, which all perform in a relatively similar manner, with the radial stub having less reflection than the other two stubs for most of the band.

These results, from both the meandered stub comparison and the stub shape comparison, suggested that the stub shape was variable for the transition, opening up potential possibilities for other applications to use different stub shapes for applications. It was theorized that keeping the perimeter the same for any stub shape would result in similar transmission loss levels, pending losses due to current crowding, but in order to further investigate this theory, substantially more investigation would be needed across many different stub shapes and meandered designs.

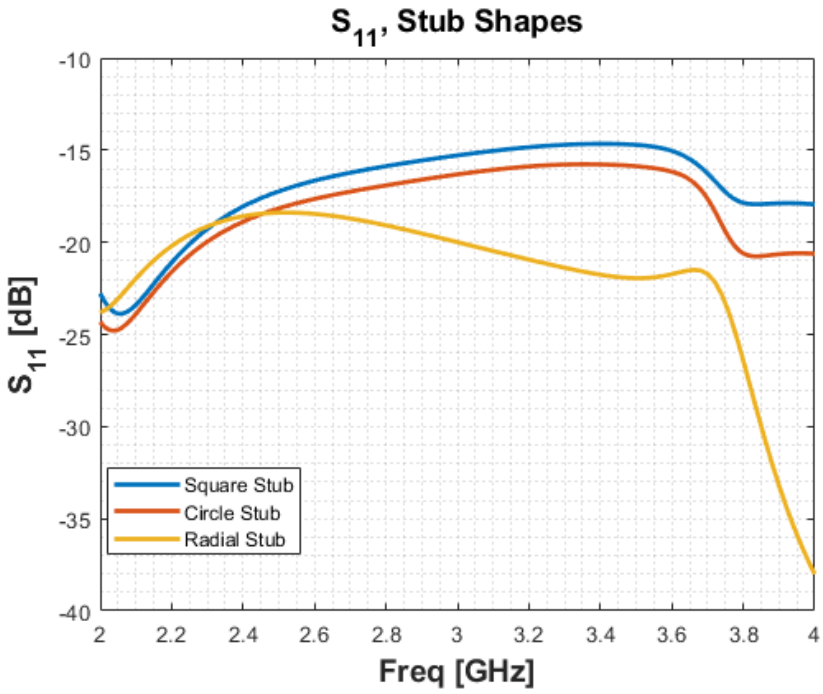

Figure 2.31: A comparison of the S_{11} of all the basic stub shapes

While this analysis was beyond the scope of this thesis, there was one alternate theory for the ability of the meandered stub to maintain similar levels of transmission as the non-meandered slot. With the meandering process, the angle of the radial stub was increased in order to reduce the size of the stub as much as possible, as the final meandered design could be reduced in size the most with a wider stub angle. However, with typical stubs of this nature, increasing the radius of the stub allows it to exhibit more broadband behavior [16]. The meandered stub could possibly be utilizing its more broadband construction to help maintain the transition rather than the perimeter of the stub being the primary factor. In order to investigate this, the meandered radial stub in Figure 2.32 was simulated with the same stub angle as the original stub. Comparing stub design to the original stub, as well as the previous meandered stub design, Figure 2.33 shows that the response from this meandered stub was close to that of the original radial stub and the prior meandered design. A comparison of S_{11} was also done in Figure 2.34, showing that these stubs had similar

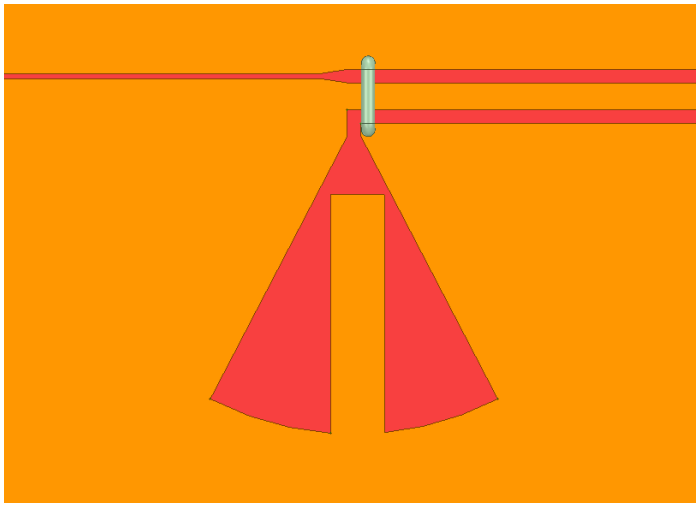

Figure 2.32: A meandering of the radial stub that preserves the stub angle

reflection loss.

Once these different designs were contrasted, a comparison between all simulated structures needed to be made. This comparison can be seen in Figure 2.35, with these S_{11} of these structures in Figure 2.36.

Some more investigation was warranted into whether the effect of perimeter on the performance of the stub. Two further stubs were investigated, one being the 9 mm radius stub with meandering seen in Figure 2.37, and the other as the 4 mm radius stub with no meandering seen in Figure 2.38. These were intended to be the counterparts (in terms of stub radii and angles) to the standard 9 mm stub seen in Figure 2.12 and the final meandered radial stub seen in Figure 2.24, respectively. The compared results of these simulations can be seen in Figure 2.39, with the compared S_{11} in Figure 2.40.

With these designs, the 9 mm meadered design had the lowest dip in transmission at 2.72 dB, but held the highest transmission in the lower portion of the band. This indicates that the stub is radiating better than the other stubs, and could be more useful across band for a transition if that radiation could be suppressed. The 4 mm nonmeandered stub exhibited similar performance when compared to the 4 mm meandered stub. However, when

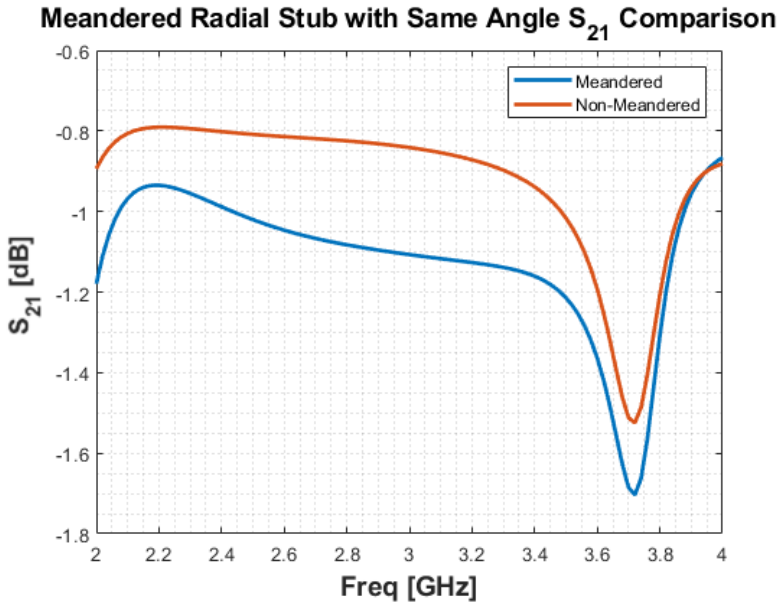

Figure 2.33: The S_{21} response of the same angle meandered stub compared to the regular stub

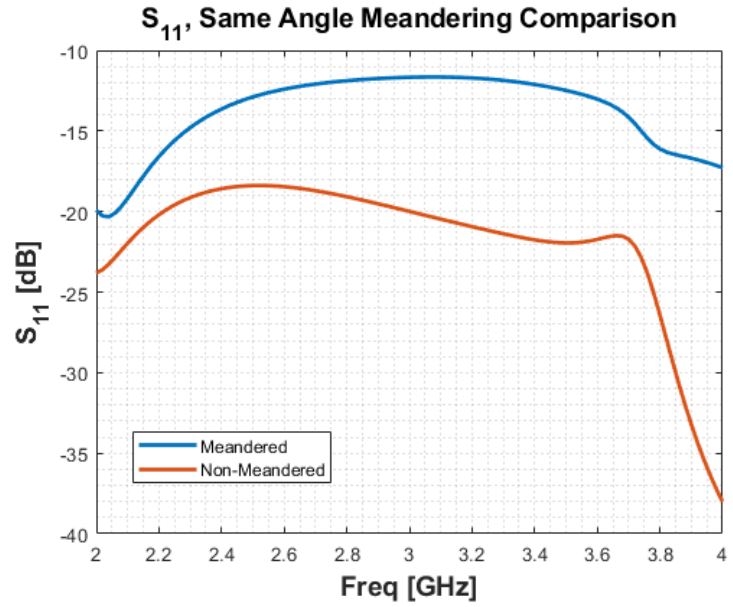

Figure 2.34: The S_{11} response of the same angle meandered stub compared to the regular stub

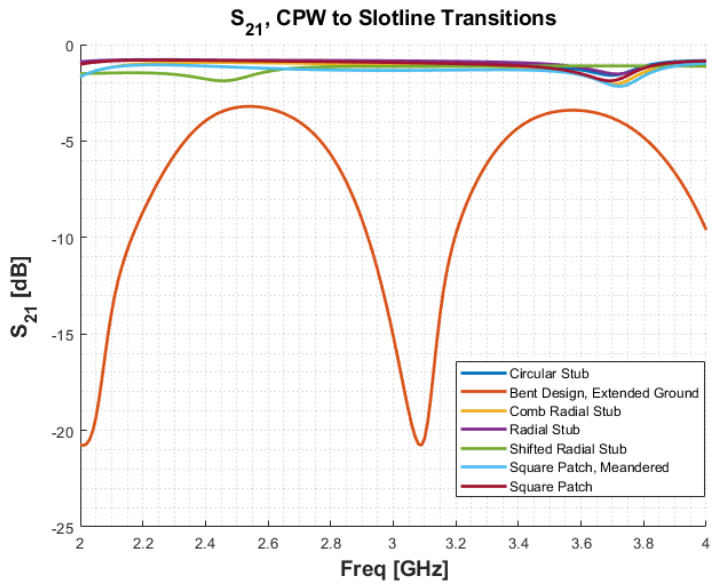

Figure 2.35: A comparison of the S_{21} of all of the simulated designs

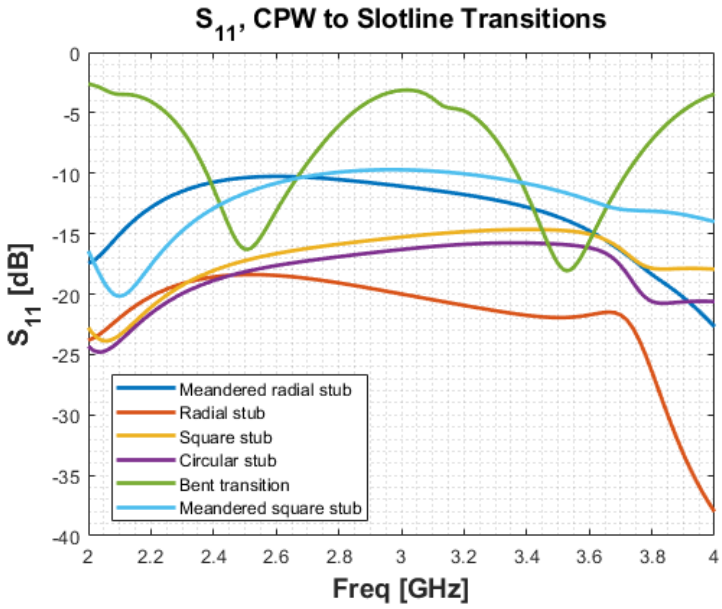

Figure 2.36: A comparison of the S_{11} of all of the simulated designs

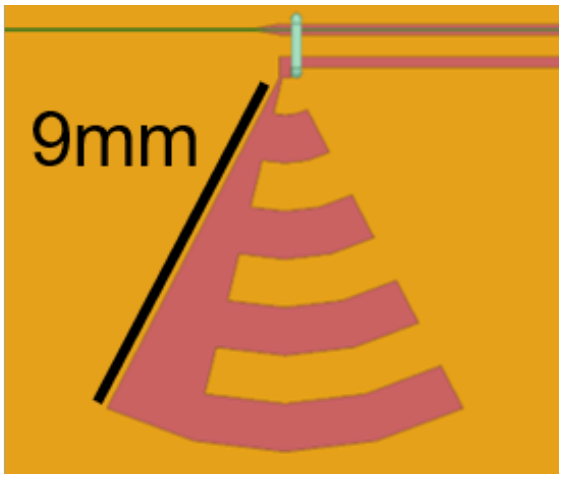

Figure 2.37: The radial stub with a 9 mm radius with meandering; This stub has a much larger perimeter (41.64 mm) than the 9 mm stub without meandering (26.64 mm).

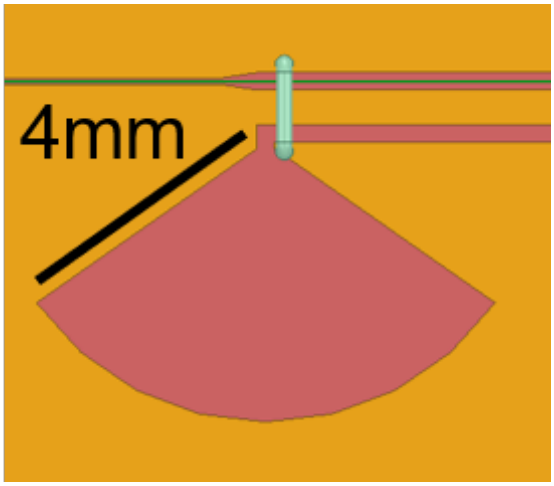

Figure 2.38: The radial stub with a 4 mm radius without meandering; This stub has a much smaller perimeter (15.68 mm) than the 4 mm meandered stub (26.64 mm).

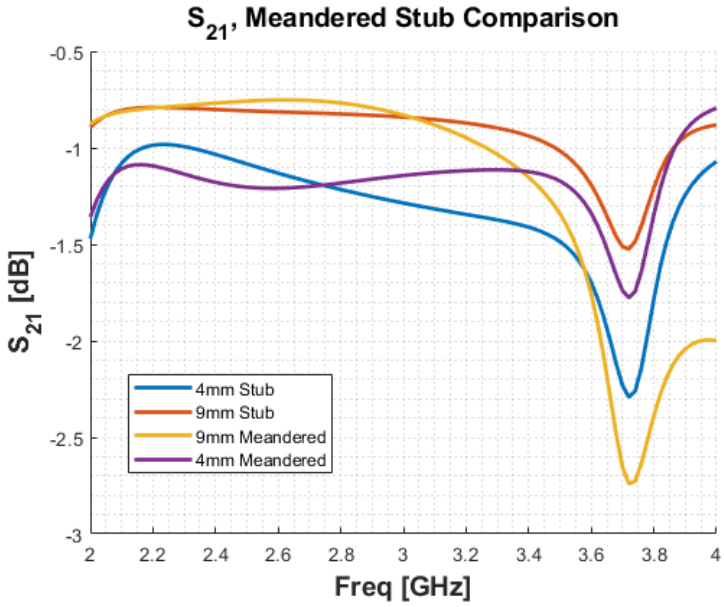

Figure 2.39: The compared S_{21} of the perimeter tested stubs; The 9 mm meandered stub and the 4 mm nonmeandered stub exhibit the greatest drop in transmission at the radiation dip, but otherwise indicate performance on-par or better than their 9 mm nonmeandered and 4 mm meandered counterparts.

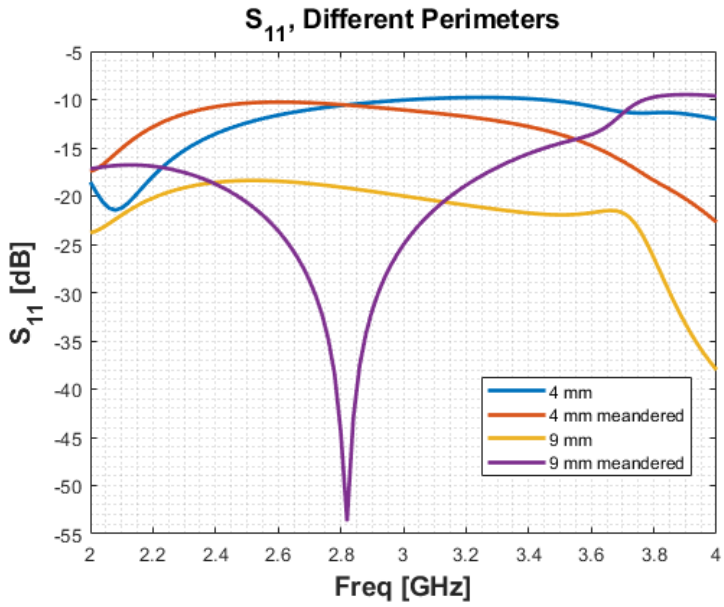

Figure 2.40: The compared S_{11} of the perimeter tested stubs

Stub Type	Max Loss (dB)	Avg. Loss (dB)	Perimeter (mm)
9mm meandered radial	2.72	1.17	41.64
4mm meandered radial	1.78	1.18	26.64
9mm radial	1.52	0.92	26.64
4mm radial	2.29	1.32	15.68
Circle	1.59	0.95	26.64
Square	1.88	1.02	26.64

Table 2.1: A comparison of the max loss, average loss, and perimeter of the different stub shapes and different perimeter stubs

comparing these four stubs with the different stub shapes in Table 2.1, it can be seen that the dip in S_{21} is much greater in these two transitions, which could cause decreased tuning capabilities in the region around the dip when the transition is used to connect the cavity resonators. The 9 mm stub with meandering also exhibited a sharp dip in S_{11} around 2.5 GHz, which is likely the reason for the increased performance of the stub in that region.

The original 9 mm radial stub, the circular stub, and the meandered 4 mm radial stub appear to be the best stubs for general use of this transition, as these have the lowest peak transmission loss of the tested transitions. The 4 mm meandered stub is the best of these for applications where the size of the stub needs to be kept to a minimum, while the others give slightly better performance if space allows for them. In applications focused more on the lower portion of the band or that can handle the dip in transmission, the 9 mm meandered stub has the best performance other than the dip and would be best. This also holds true if the radiation dip can be addressed.

2.6 Conclusion

This chapter discussed the development of a miniaturized coplanar waveguide to slotline transition for the purposes of connecting a tunable cavity resonator to a slot antenna. This was in an effort to create a tunable slot antenna, using the cavity as a load to shift the

operating frequency of the antenna. Designs for coplanar waveguide to slotline transitions had already been developed in previous works, but this thesis presented a novel way to miniaturize the stubs most of these designs used while maintaining low transmission loss through the transition. This miniaturization method was used with several stub shapes, and yielded similar levels of miniaturization without significant increases in loss. In the future, other transitions and even smaller miniaturized stubs could be investigated to discover the applications of this method and gauge its limitations. From this point in the project, the meandered transition from Figure 2.24 needed to be used in a tunable slot antenna setup to see if it would fix the radiation efficiency issues the previous tunable slot design had faced.

Chapter 3

Tunable Antenna Designs

3.1 Introduction

With the development of the miniaturized coplanar waveguide to slotline transition discussed in Chapter 2, a new method of coupling between the cavity resonator and slot antenna was available. This would ideally address the issue with poor radiation efficiency at the resonance of the antenna that the previous design faced. From this point, the coplanar waveguide to slotline transition needed to be implemented into the antenna design to see if it maintained high radiation efficiency at resonance while maintaining tuning capabilities.

3.2 Coplanar Waveguide to Slotline Transition Based Slot Loading

3.2.1 End Loaded Dual Cavity Design

This design in Figure 3.1 was essentially the same as the original slotline based connection, but used coplanar waveguide to couple into the cavity rather than slotline. As a note, all simulated antenna designs in this chapter are fed at the center of the antenna, possible due to the symmetry of the antenna designs, with a lumped port.

This design did not exhibit the sharp dip in radiation efficiency at the resonance of the antenna seen in the previous slotline based design, but had tuning issues. These factors

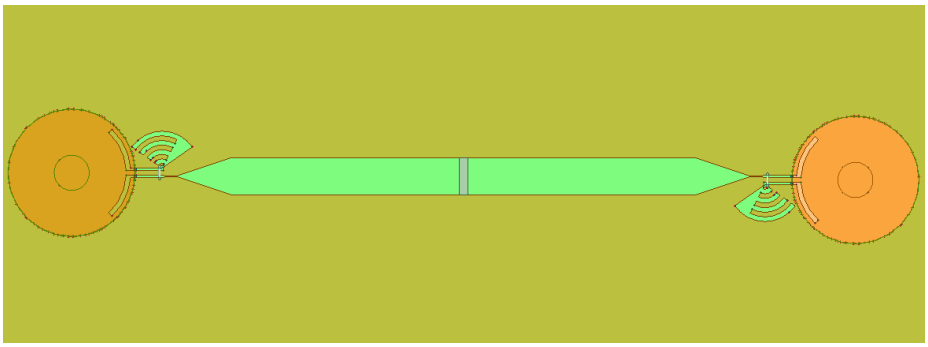

Figure 3.1: A modification of the original cavity-end-loaded slot that uses the coplanar waveguide to slotline transition to couple between the slot and the cavities

indicated that the slotline was not being significantly loaded by the cavities.

Looking at the fields, it was seen that the cavity was operating in a higher order mode. This indicated that the resonant frequency of the cavity was not within the 2 GHz to 4 GHz band, and as such the range of gap sizes of the cavity needed to be adjusted to tune across S-band. This tuning range is found using the equations

$$\lambda = 2\pi\sqrt{r_0 h\left(\frac{r_0}{2d} + \frac{2}{\pi}\ln\frac{el_M}{d}\right)\ln\frac{r_1}{r_0}}$$

and

$$l_M = \frac{\sqrt{(r_1 - r_0)^2 + h^2}}{2},$$

with variables defined as shown in Figure 3.2 [17]. The gap size range was found to be 3 μm to 17 μm, which resulted in the 2.4 GHz to 3.9 GHz tuning range shown in Figure 3.3. Figure 3.4 shows stronger resonances present above 4 GHz as well, but these did not have a wide tuning range like the lower resonances.

This design seemed promising at first, but looking at the radiation efficiency in Figure 3.5, this design proved unviable, as there were significant dips in radiation efficiency. These radiation efficiency drops occurred at the resonance of the antenna, with Figure 3.6 showing the resonances of the antenna and the dips in radiation efficiency lining up, similar

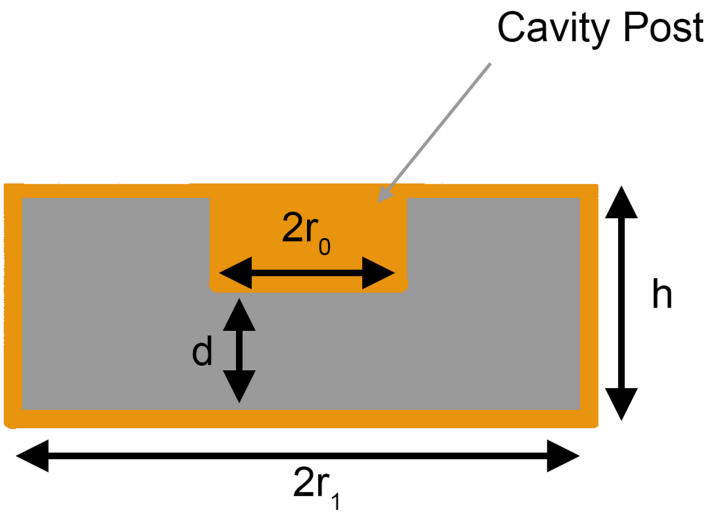

Figure 3.2: The dimension definitions used to find the cavity tuning range

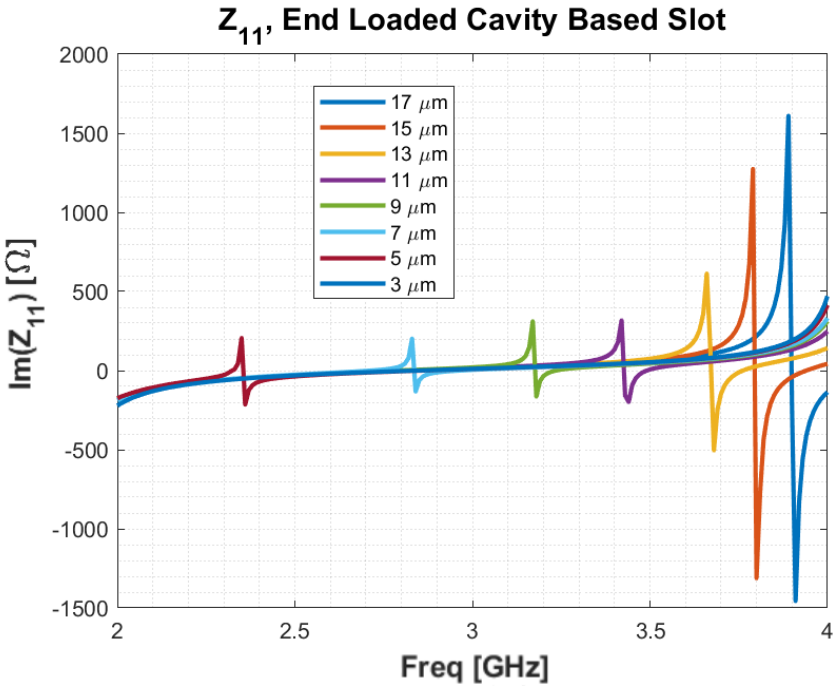

Figure 3.3: The tuning observed in the 2 GHz to 4 GHz band; These resonances seemed to be capable of working for tuning across most of S-band.

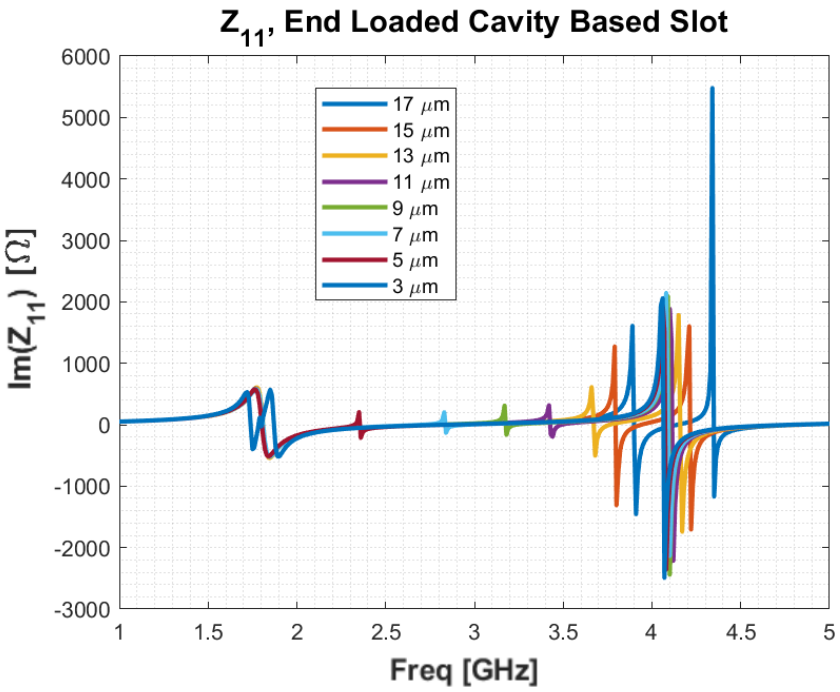

Figure 3.4: The expanded range of frequencies, showing the higher antenna resonances with a smaller tuning range

to the initial slotline-connected design. This indicated that there may be an inherent issue with end-loading the slot using the cavity resonators.

3.2.2 Center Loaded Single Cavity Design

Next, the design seen in Figure 3.7 was investigated. It involved using a single cavity in the center of the slot rather than two cavities at the ends of the slot. This antenna design was based on the use of coplanar waveguide to feed slot antennas, as this location should be viable for loading as well.

Figure 3.8 shows that this design yielded about 0.35 GHz of tuning. It also managed to maintain radiation efficiency levels above 90% at the tuned resonances, avoiding the radiation efficiency dip issue the initial slotline based design faced. This radiation efficiency can be seen in Figure 3.9. There were slight dips in radiation efficiency at the resonance

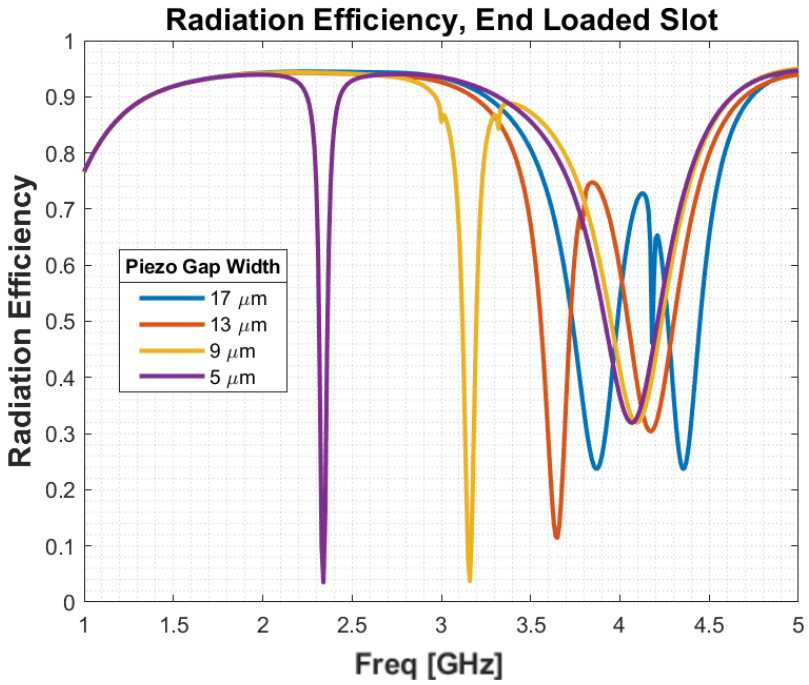

Figure 3.5: The radiation efficiency of the end-loaded design that used the coplanar waveguide to slotline transition

of the slot, but they were shallow enough (only 3-5% drops) to not pose issues to the function of the slot. However, there did not seem to be a way of significantly increasing the tuning range of this design without needing significant swings in the capacitive gap in the cavity, which ran into physical issues with both cavity integrity and piezoelectric device capabilities.

3.3 Trapped Dipole Applications to Cavity Tuned Slots

While these antenna designs were being developed, it was discovered that end-loading a slot maximizes tunability while also causing the radiation efficiency to dip at the resonance of the antenna, while center-loading the slot maximizes radiation efficiency at the cost of tunability [18]. This matches the behavior seen by the slotline-loaded antenna simulated previously. This also explains the low tunability and high radiation efficiency of the center-

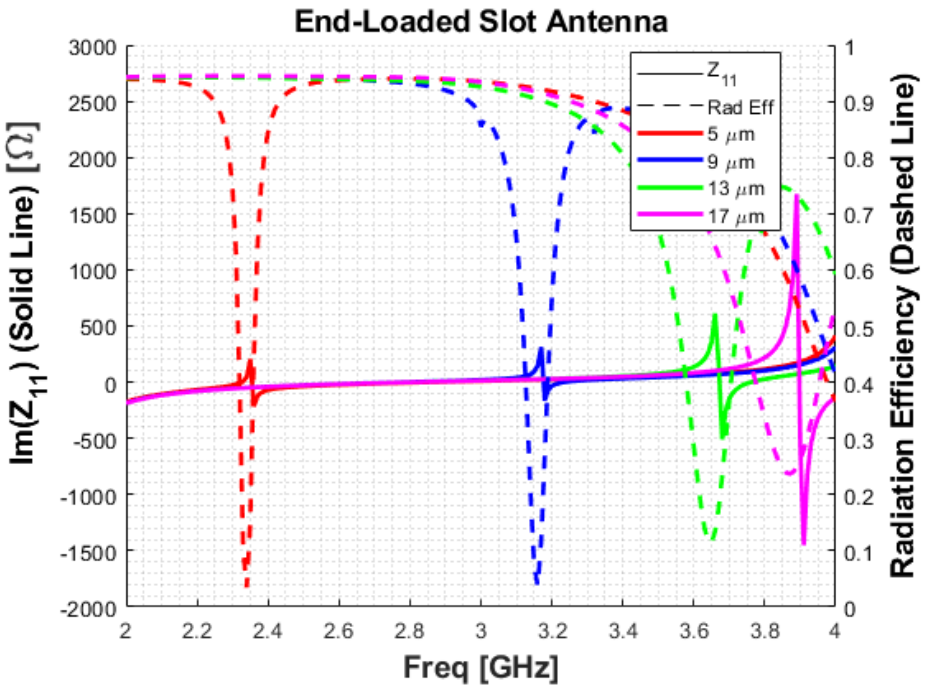

Figure 3.6: The radiation efficiency and imaginary Z_{11} plotted together; This shows that the radiation efficiency dips occur at the resonances of the slot, exhibiting the same issues that the previous end-loaded slot design experienced.

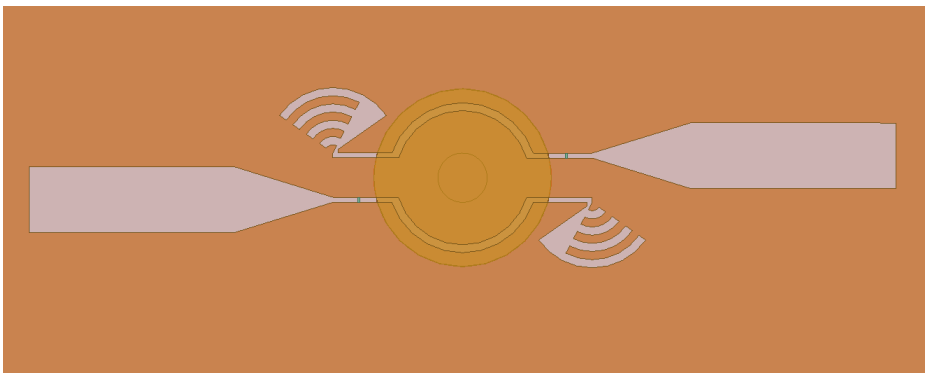

Figure 3.7: A design that uses the coplanar waveguide to slotline transition to load the antenna with a single cavity in the center of the antenna

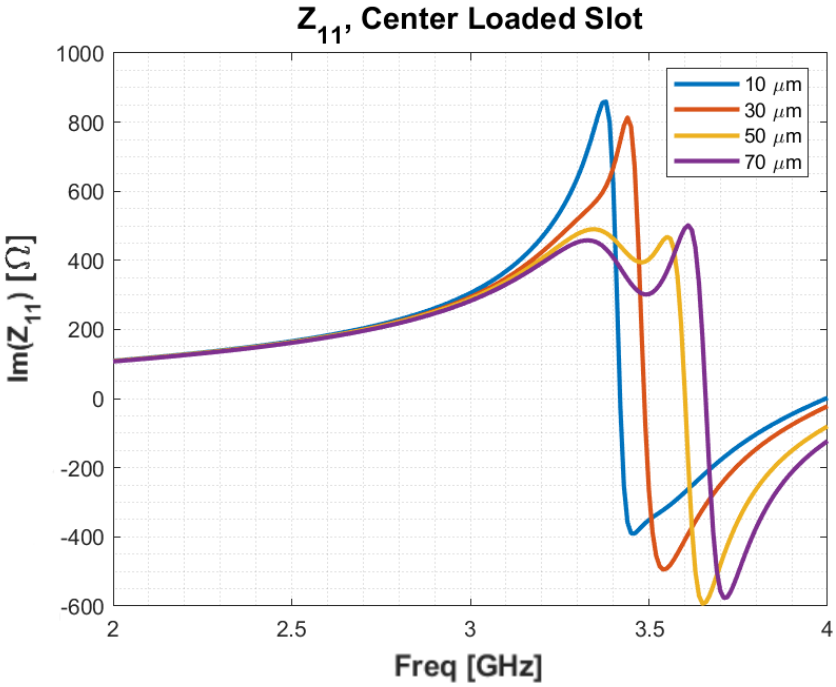

Figure 3.8: The frequency tuning range of the center-loaded slot design; This design exhibits about 0.35 GHz of tuning.

loaded slot.

3.4 Alternative Slot Loading Methods

3.4.1 Coplanar Waveguide Side Loaded Slot

Because of this discovery, the design of the tunable slot antenna changed to the design in Figure 3.10 that loaded the slot with cavities located on the sides of the antenna. The simulations in HFSS for this design use lumped capacitance elements to represent the cavities for lower simulation times. With this side loaded slot design, the coplanar waveguide to slotline transition was unnecessary, as coplanar waveguide can be used to directly couple to the side of a slot.

This design was investigated, both with the standard coplanar waveguide loaded design

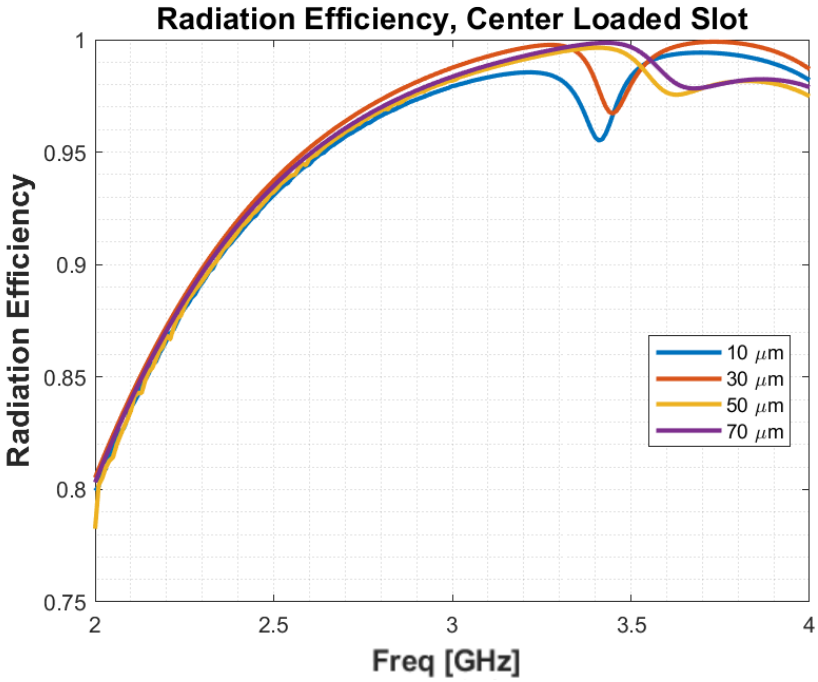

Figure 3.9: The radiation efficiency of the center-loaded slot design; There are slight nulls in radiation efficiency at the resonances of the antenna, but they only drop by about 2 to 5%.

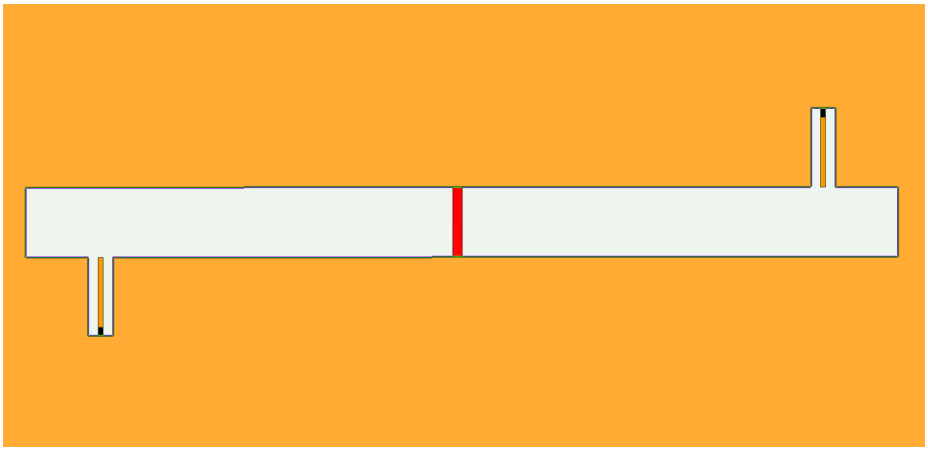

Figure 3.10: A slot side-loaded with coplanar waveguide; This was intended to allow for higher frequency tuning range while lowering the dip in radiation efficiency.

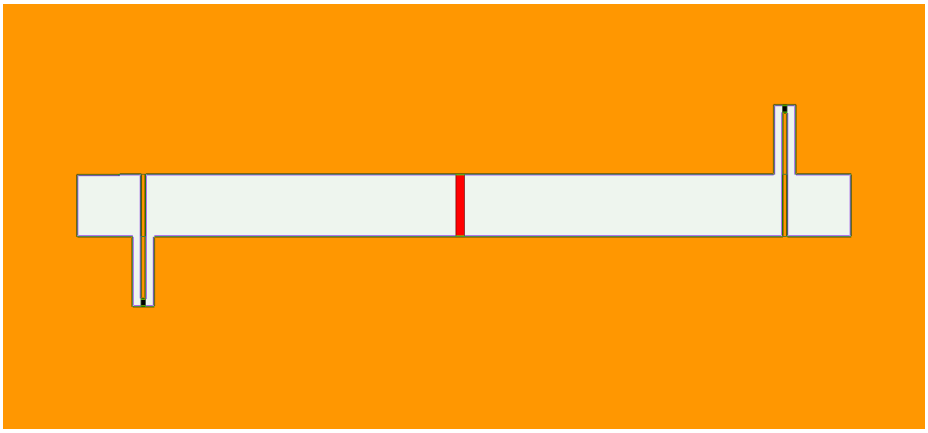

Figure 3.11: The side-loaded slot design with the signal line of the coplanar waveguide shorted across the slotline

and the design in Figure 3.11 with the signal line shorted across the slot, but yielded almost no tuning of the resonance of the slot with either design. This trend for the non-shorted design can be seen in Figure 3.12.

After some further investigation, it was realized that coplanar waveguide can only directly couple to the side of a slot at the center of the slot, as the currents induced by the slot conflict with the currents of the offset coplanar waveguide. This trend can be seen in Figure 3.13. The only offset CPW connections to slots have extra transmission line offshoots allowing the currents to match up correctly, or to shift the load point away from the center by a wavelength, which is not possible with the antennas used for this project [19].

3.4.2 Microstrip Loaded Slot Antenna

While these designs were being investigated, the design in Figure 3.14 that loaded the antenna with a microstrip to coplanar waveguide line was explored. This design resulted in the 1.4 GHz of tuning (from 2.1 GHz to 3.5 GHz) seen in Figure 3.15 using a capacitance range of 0.1 pF to 11 pF. At a 60:1 ratio of capactiance (pF) to tuning frequency (GHz), this requires a large change in capacitance to achieve.

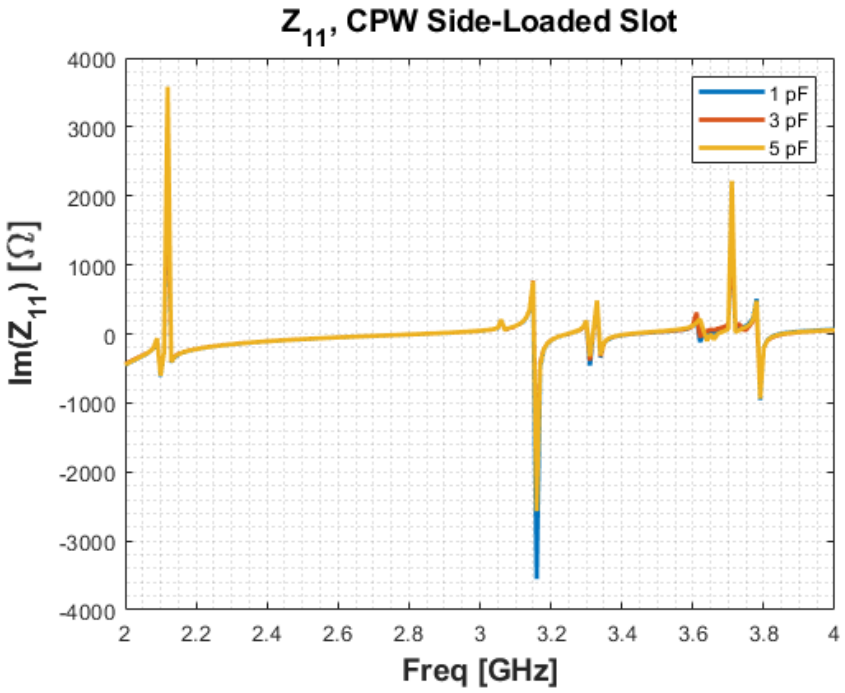

Figure 3.12: The Z_{11} response of the coplanar waveguide side-loaded slot; This design exhibits no tuning, indicating that loading method does not allow the cavity impedance to be seen by the slot.

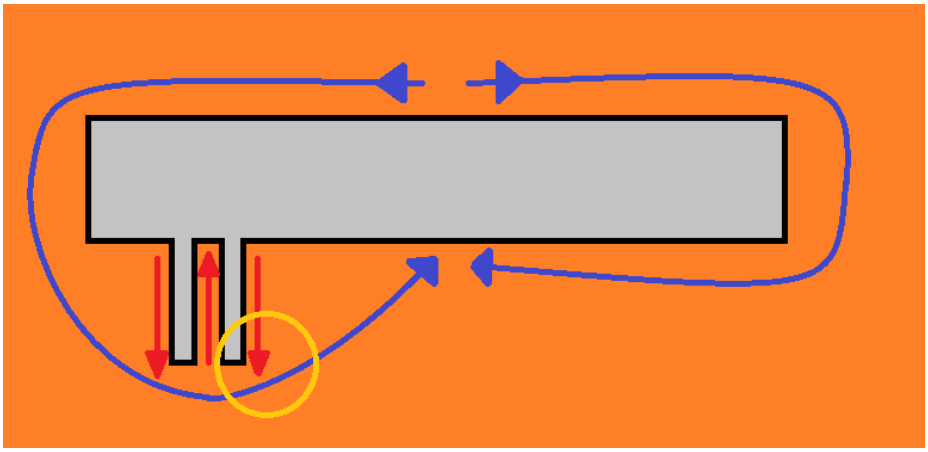

Figure 3.13: The conflicting currents of the slot antenna (blue) and connected coplanar waveguide (red); the area of conflict is circled in yellow, and only one coplanar waveguide connection is shown.

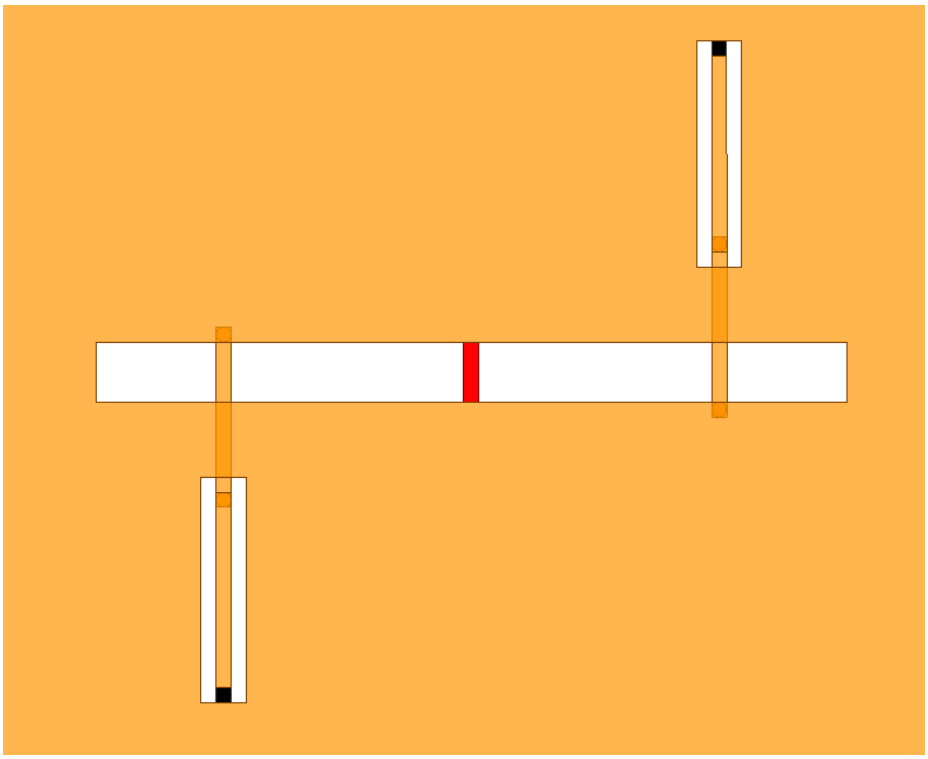

Figure 3.14: A slot antenna side-loaded with a microstrip-to-coplanar loading structure

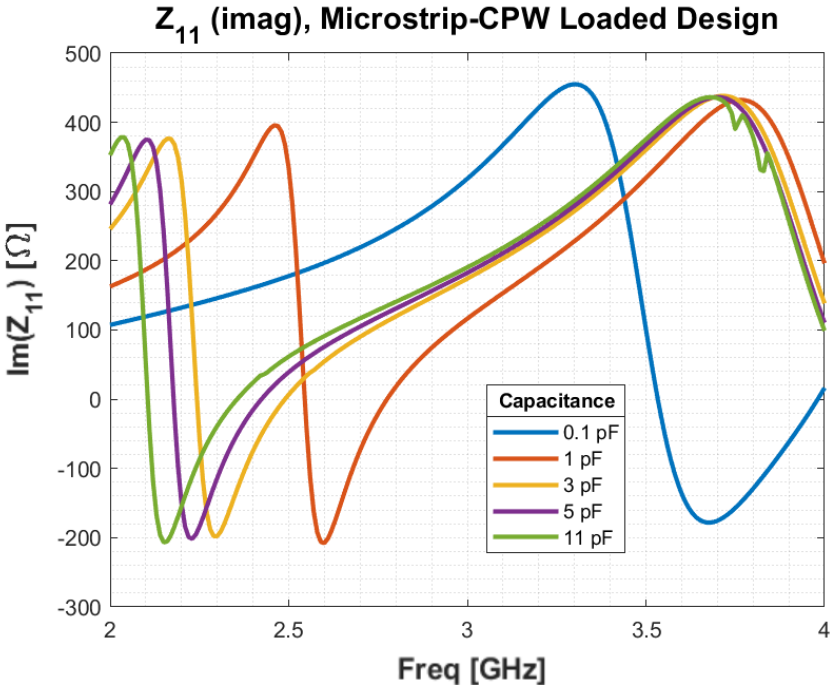

Figure 3.15: The initial tuning response of the microstrip loaded slot antenna

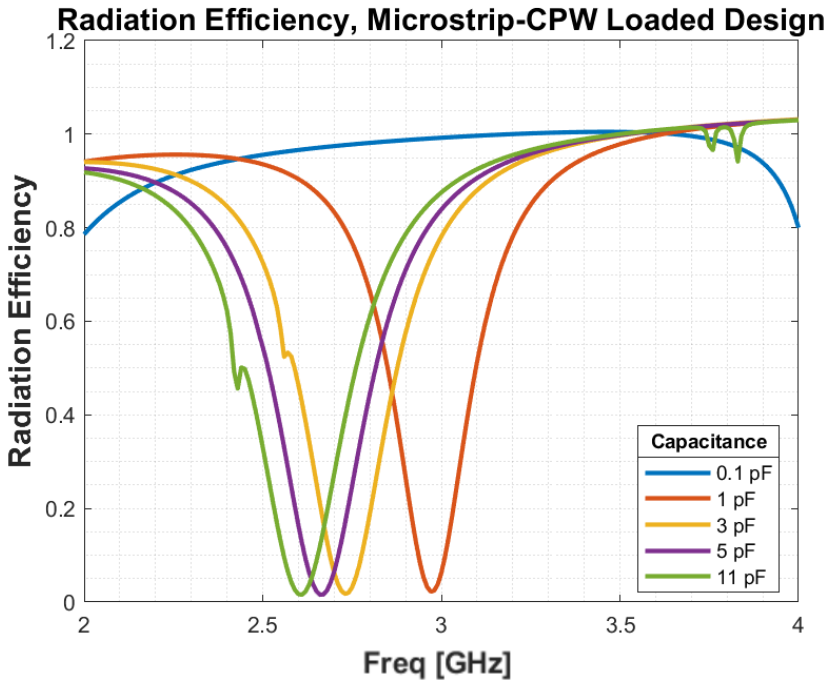

Figure 3.16: The radiation efficiency of the microstrip loaded slot antenna

When the radiation efficiency was investigated, however, it seemed a similar problem to the one the end-loaded slots faced had arisen with this design. There were major dips in radiation efficiency, effectively hitting zero at certain points along the band. This can be seen in Figure 3.16. However, upon further inspection, it was found that these dips in radiation efficiency were off-resonance, with their alignment shown in Figure 3.17. This indicated that this antenna was viable as a tunable slot for this project.

3.5 Tunable Antenna Design Analysis

With several tunable antenna designs developed, they needed to be analyzed to determine which antenna had the most promise for implementation. First, looking at the end loaded slot design (Figure 3.1), the tuning range seemed promising, but the issues with radiation efficiency at resonance made it difficult to move forward with this design. Based on work

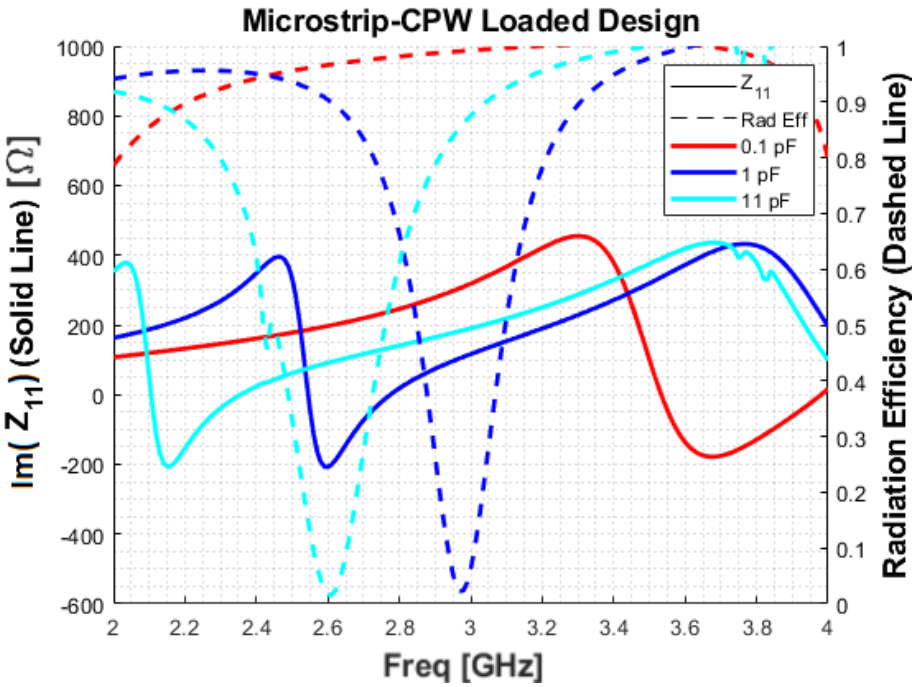

Figure 3.17: The radiation efficiency nulls and the resonances of the slot; These do not line up, yielding a viable tunable slot.

with trapped dipoles, it was thought that the end loading of the slot was the issue causing the radiation efficiency problems, but significantly more work would be needed to further back up this theory, and other antenna designs showed promise with significantly less theory work needed to fix the issues.

The second design, the center-loaded slot (Figure 3.7), did not experience the same issues with coupling as the end-loaded slot design, but had a significantly smaller tuning range. Several dimension adjustments were attempted to achieve greater tuning capabilities out of this antenna, but none of the efforts yielded a significant enough increase in tunability to indicate that this design would be worth pursuing over others, as any modifications necessary would be much more complicated than those needed for other antenna designs, and the design might even prove to be incapable of achieving full S-band tuning.

The final design, the coplanar waveguide to microstrip loaded slot (Figure 3.14), seemed

to be the most promising candidate moving forward. It had exhibited up to 1.5 GHz of tuning range without the drop in radiation efficiency at resonance. However, the design also needed a very high tuning ratio, 100:1, in order to achieve those levels of tunability. It could provide 1 GHz of tunability with only a 10:1 ratio, but this aspect of the antenna would need to be investigated further in order to both cover the full frequency band and reduce the tuning ratio as much as possible. Radiation efficiency could also pose a problem with this design. Despite the dips in radiation efficiency being off-resonance for the antenna, they could still have an effect on the efficiency at resonance if they were sufficiently close or covered a wider frequency band. This behavior was not the most pressing concern, but in future iterations on this design, care should be taken to ensure that any modifications do not make this radiation efficiency dip an issue with the behavior of the antenna.

3.6 Conclusion

Connecting the slot antenna to the cavity using the coplanar waveguide to slotline transition from Chapter 2 resulted in a slot capable of tuning across almost all of S-band, but still faced the radiation efficiency issues seen in the previous tunable slot design. Moving the load cavity to the center of the slot alleviated this problem, but resulted in a significantly decreased tuning range that made the antenna difficult to use for a tunable array. With these designs giving direction for antenna design for loading slot antennas, a novel tunable slot using a microstrip to coplanar waveguide connection was designed that attempted to use the properties of both the end loaded and center loaded slots in order to achieve a larger tuning range without the nulls in radiation efficicency at the antenna resonance. This resulted in an antenna with approximately 1.4 GHz of tuning that did not experience these nulls at the antenna's operating frequency. With a design that exhibited desired characteristics from both the end loaded and center loaded slots to be tuned to cover all of S-band in the future,

methods of fixing issues with array coupling could be investigated within a tunable slot array design.

Chapter 4

Mutual Coupling Tuning Mechanism

4.1 Introduction

With a functioning tunable antenna design (both the microstrip to coplanar waveguide loaded design and the design developed in [20]), arraying the tunable slots could proceed. However, before a successful array could be built with these tunable antennas, the issue of mutual coupling in the array needed to be addressed.

4.1.1 Mutual Coupling

Mutual coupling is the process of power from one element in an array being transmitted to another array element, typically through radiation [9]. A basic view of the process of the mutual coupling process can be seen in Figure 4.1. Power is input into one antenna and radiated. Some of this power is received by the secondary antenna, interfering with its signal and increasing the reflection seen by the feed of the second element. This can cause scan blindness and can also result in reradiation of the power applied to one antenna by another, cascading the power transfer through the array.

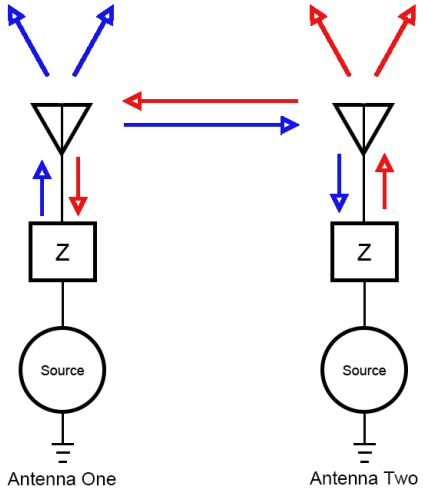

Figure 4.1: A diagram of the process of mutual coupling [21]; Power is transferred from the first element's supply to the antenna, then radiated both into free space and partially to the second array element. This radiated power affects the phase and magnitude of the second element's signal, leading to cancellations at certain angles due to phase mismatch.

4.1.2 Scan Blindness

This interference between antenna elements leads to an issue called scan blindness. When scan blindness occurs, the antenna elements are incapable of radiating into free space because all of the energy from that element is being transmitted into other antenna elements in the array, resulting in a reflection coefficient of 1 at the antenna [22]. This results in "blind angles" represented in Figure 4.2, which are regions where no transmission or reception can occur in the array pattern. In radar systems, this can result in missed detections and loss of tracking on targets that pass into the blind region.

Previous methods of cancelling out mutual coupling in arrays have been developed, such as those shown in [14] and [15], but only for patch antennas at static frequencies. Thus, a new method was necessary to work with tunable slot antennas.

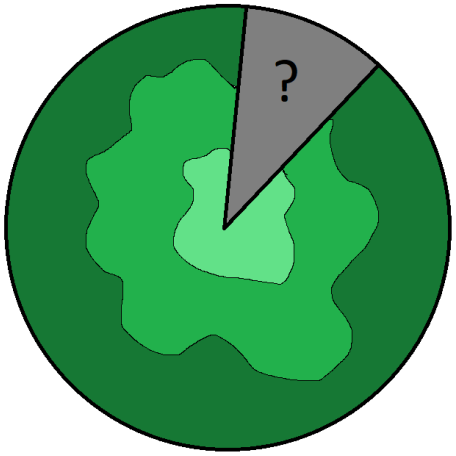

Figure 4.2: A visualization of scan blindness in array images; This phenomenon can cause loss of targets when tracking and inability to detect any new targets in certain regions.

4.2 Baseline Slot Array

In order to see the effects of the tuning mechanism on the mutual coupling of the slot array, the baseline S_{21} of a two element slot array depicted in Figure 4.3 needed to be determined. This baseline S_{21} can be seen in Figure 4.4 and would allow future tuning designs to be compared to see if they were actually causing nulls or peaks in mutual coupling relative to the normal coupling of the array. These slots were designed to be $\frac{\lambda}{2}$ long at 3 GHz. The currents and electric fields in this array also needed to be checked for comparison to later designs. These currents and electric fields can be seen in Figure 4.5 and Figure 4.6 respectively.

4.3 Initial Designs

There were a few designs that were investigated initially based around radiative coupling to the slots. These designs, such as the design seen in Figure 4.7, exhibited almost no mutual coupling tuning. It was thought that their method of coupling between the slots was not

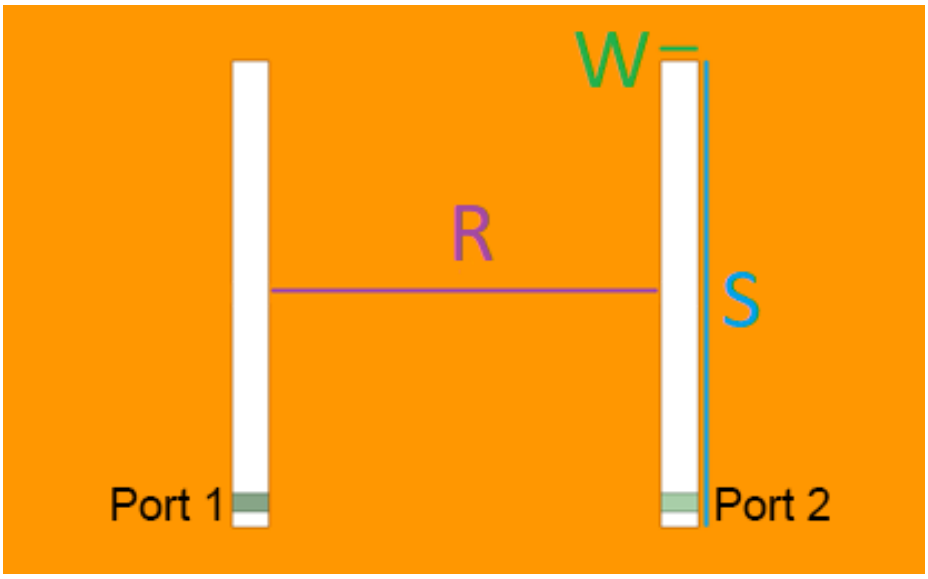

Figure 4.3: The two-element slot array without any mutual coupling tuning mechanism; In this design, S = 50 mm, R = 50 mm, and W = 4 mm.

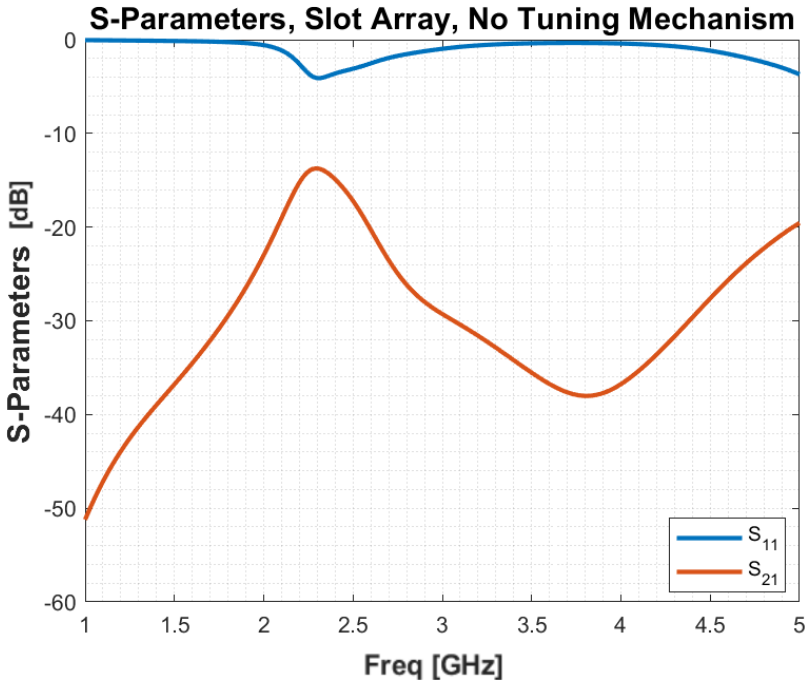

Figure 4.4: The S_{11} and S_{21} responses of the slots without any tuning mechanism; This is used as a baseline to evaluate mutual coupling tuning attempts.

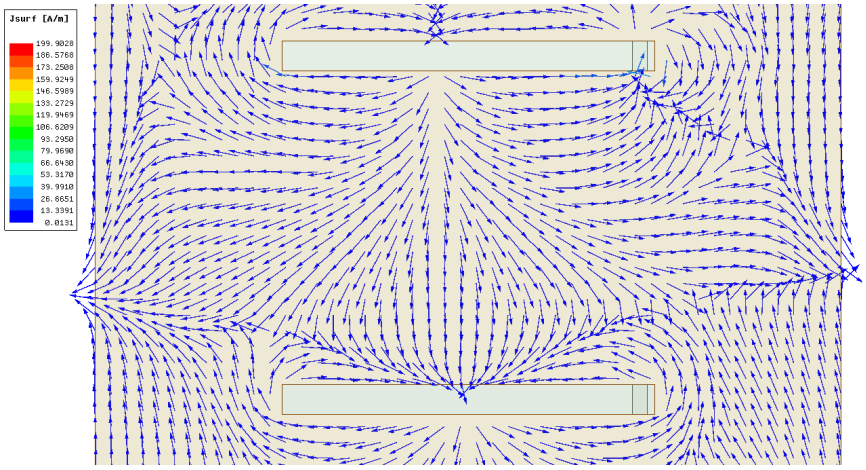

Figure 4.5: The current behavior on the array used to establish a baseline

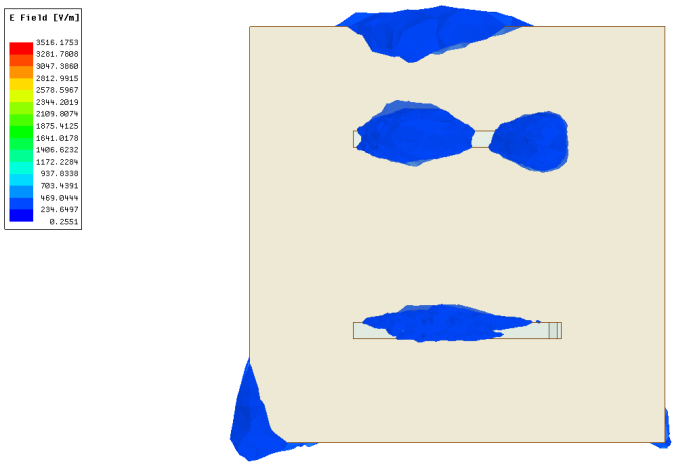

Figure 4.6: The electric field behavior on the array used to establish a baseline

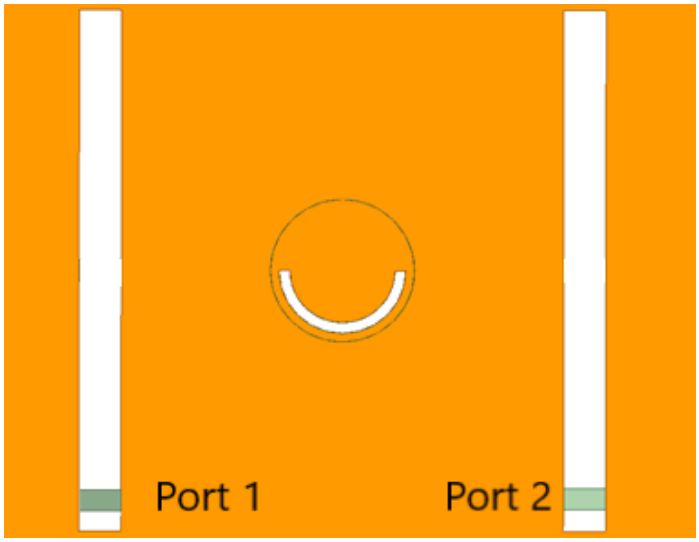

Figure 4.7: A mutual coupling tuning design based on a tunable cavity with a cutout using radiative coupling to tune the mutual coupling of the antennas; This method also exhibited no tuning, hinting that direct coupling or stronger coupling methods were needed to achieve mutual coupling tuning.

strong enough, as it relied on radiative coupling at a farther distance than other proposed ideas.

4.3.1 Slotline Based Design

In order to try to increase the effect of the tuning mechanism on the coupling between the slots, it was determined that the design would need a direct coupling path between the slots. The next attempted design in Figure 4.8 relied on a direct guided coupling path between the slots, achieved by running slotline loaded with shunt capacitances between the antennas.

This structure would not need to handle as much power as the slot antennas, as it only needed to cancel out mutual coupling between the antennas, which showed a maximum S_{21} at the operating frequency of the antenna of about -12 dB. This corresponded to a necessary power handling of about 3.155 W, making more tuning structures viable for use in place of the lumped elements. However, in the case that a higher power tuning structure

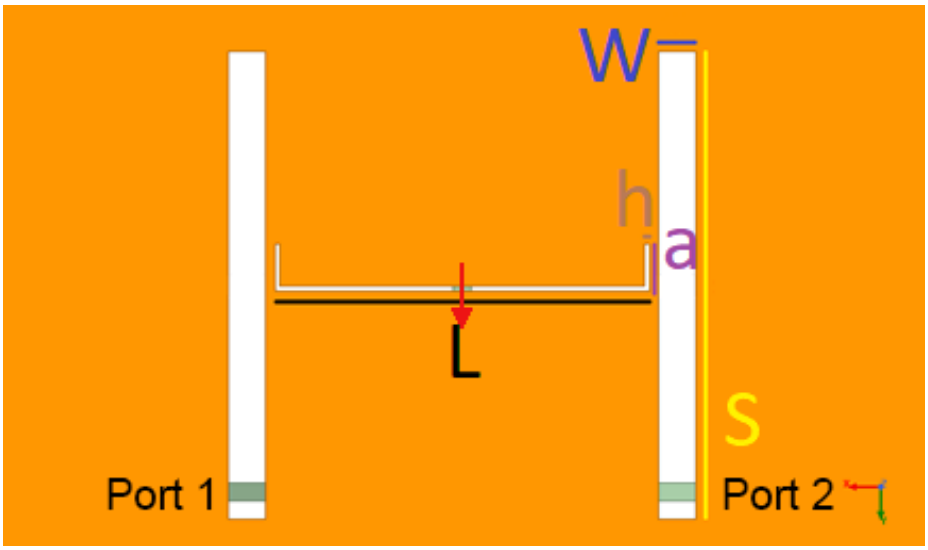

Figure 4.8: A slotline based design intended to tune mutual coupling that relied on direct coupling between the slots along the line; The arrow indicates the integration line across the lumped (shunt) capacitance. In this design, L = 40 mm, S = 50 mm, a = 5 mm, W = 4 mm, and h = 0.5 mm.

is needed, a proposed structure can be seen in Figure 4.9 that implements the microstrip loading mechanism from the side-loaded tunable antenna design. This would allow cavities to be used for tuning each element individually, but would also increase operation and fabrication complexity significantly.

This design managed to exhibit a small tuning response that can be seen in Figure 4.10, with deeper nulls around 4 GHz and shallower nulls around 2 GHz.

Once these nulls had emerged, their location and sensitivity needed to be adjusted in order to fully tune across S-band. The first step in increasing this sensitivity was moving the slotline from the center of the slot antennas to the end opposite the port. Because the magnetic field maxima of a slot are at its ends, as opposed to the magnetic field minimum at the center of the slot, moving the slotline to the end of the antenna would allow for increased coupling strength, and thus a stronger tuning response. This modification, as shown in Figure 4.11, resulted in the mutual coupling response seen in Figure 4.12. The

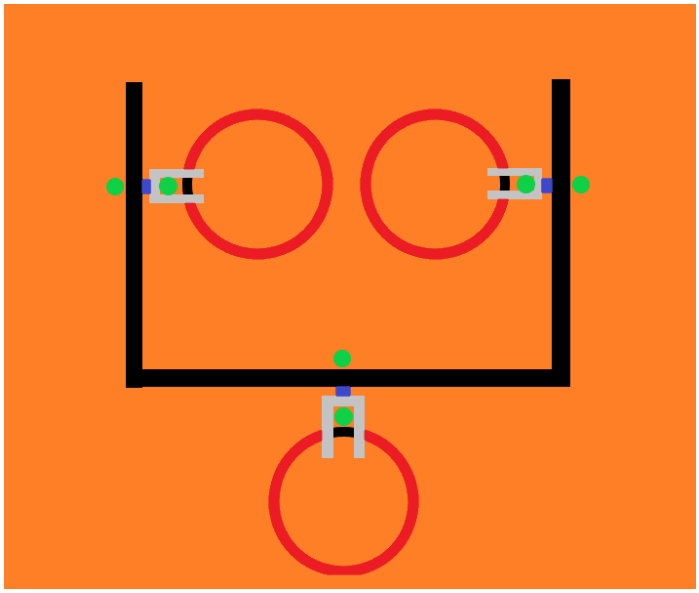

Figure 4.9: A proposed cavity loading mechanism for the slotline on the mutual coupling tuning mechanism; This design is adapted from the side-loaded antenna design discussed in Chapter 3. Green indicates vias, red indicates the cavities, grey indicates coplanar waveguide, black indicates slotline, and blue indicates microstrip (on the bottom side of the substrate connecting two vias. This could possibly be replaced with a single cavity coupled to each point on the slotline, but coupling paths through the microstrip could emerge, so further investigation would be needed.

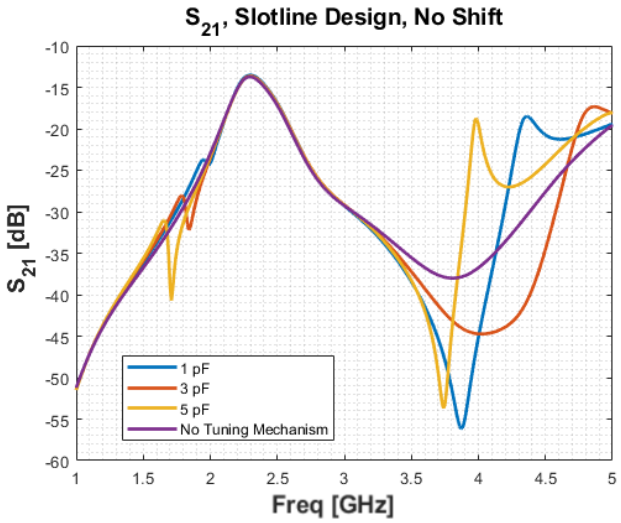

Figure 4.10: The S_{21} response of the slotline based design; This design developed some mutual coupling nulls, which made it promising as a mechanism for tuning the mutual coupling.

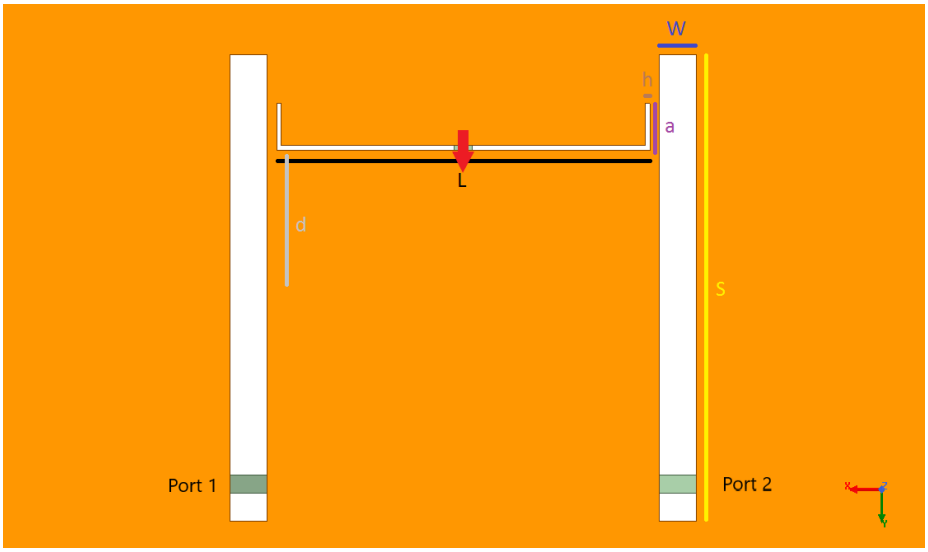

Figure 4.11: The shifted slotline based mutual coupling tuning design; This allowed for stronger coupling between the slotline and the slot antennas, as the slotline was coupling to a portion of the slot with the strongest magnetic field. The arrow indicates the integration line across the lumped (shunt) capacitance. In this design, L = 40 mm, S = 50 mm, a = 5 mm, W = 4 mm, h = 0.5 mm, and d = 14.75 mm.

shift in location of the slotline muted the nulls towards the top of the band while causing the nulls towards the bottom of the band to deepen, indicating stronger coupling between the transmission line and the antenna.

After some investigation into this new design, it was found that the currents on the slotline were not exhibiting the patterns that were typically present on slotline. There were some strange fringing effects at the end of the slot antenna that were interfering with the slotline, thus reducing its effectiveness as a loading mechanism due to current cancellation. This behavior can be seen in Figure 4.13. It was found that extending the slotline beyond the end of the slot antenna as in Figure 4.14 fixed this issue.. This resulted in a tunable mutual coupling null that covered the range from 3 GHz to 4 GHz. This is shown in Figure 4.15.

The next step was trying to get the mutual coupling nulls to cover the full S-band. In order to increase tuning sensitivity, the lumped capacitances along the slotline were moved.

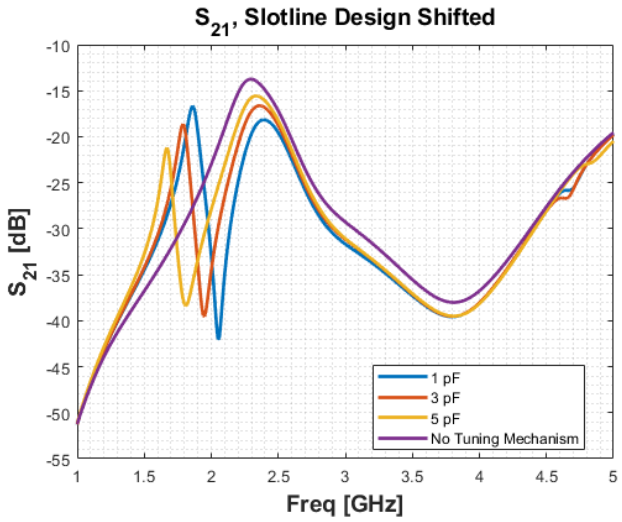

Figure 4.12: The S_{21} response of the shifted slotline design; The nulls towards the bottom of S-band (the lower order resonances) are significantly deeper due to the increased coupling strength between the slot and slotline.

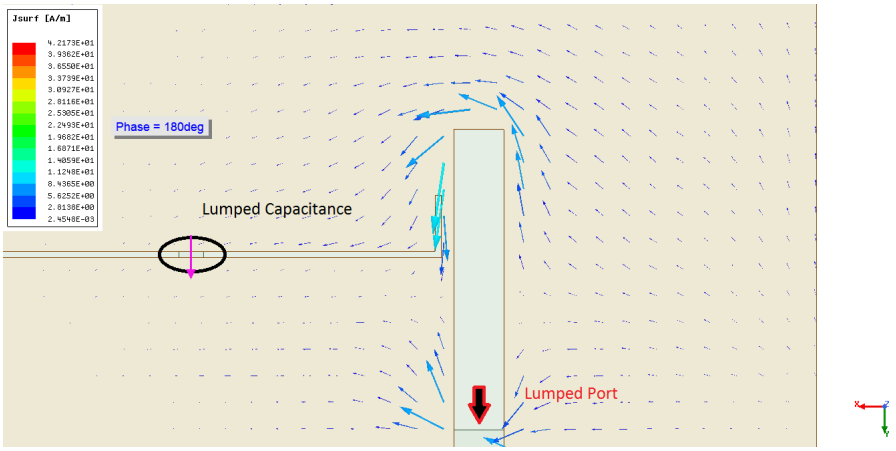

Figure 4.13: The current direction with the slotline not extending past the end of the slot antenna; This design was exhibiting abnormal current patterns on the slotline, as the currents on opposite sides of the transmission line were not 180 degrees out of phase from each other. The arrow across the slotline indicates the integration line across the lumped (shunt) capacitance.

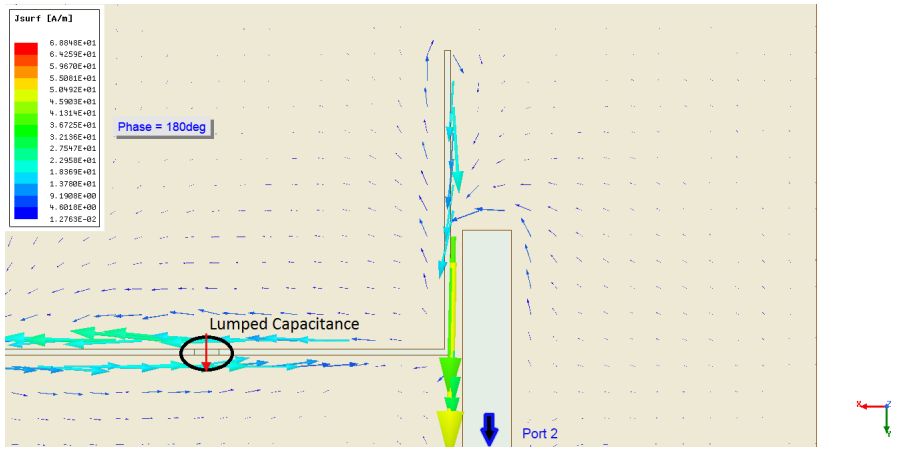

Figure 4.14: The fixed current patterns after the slotline was extended past the end of the slot antenna; The slotline was exhibiting normal slotline current patterns, with the currents on opposite sides of the slotline 180 degrees out of phase from each other. The arrow across the slotline indicates the integration line across the lumped (shunt) capacitance.

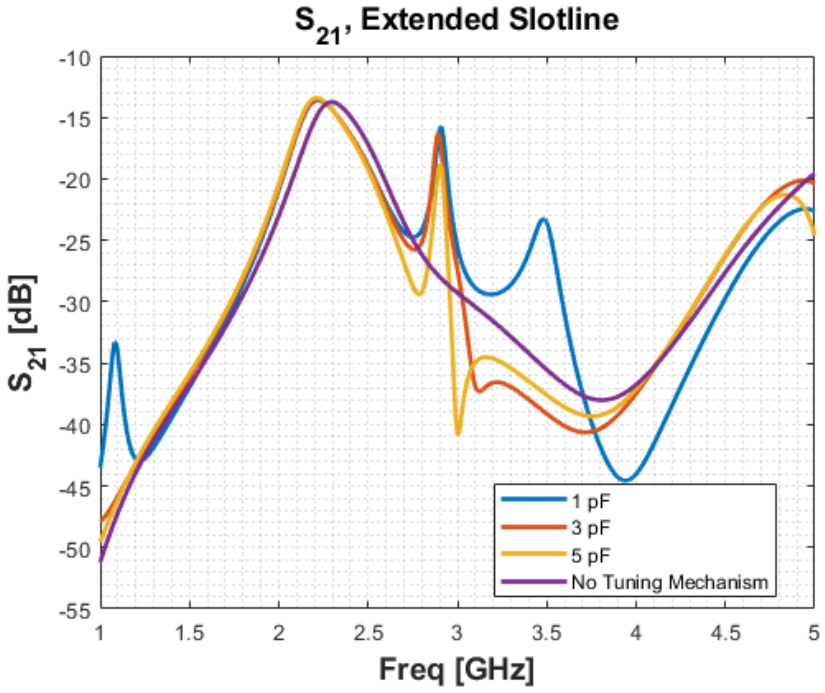

Figure 4.15: The mutual coupling response of the slot array with slotline extending past the ends of the slots; The tuning range was expanded to 1 GHz of tuning (from 3 GHz to 4 GHz).

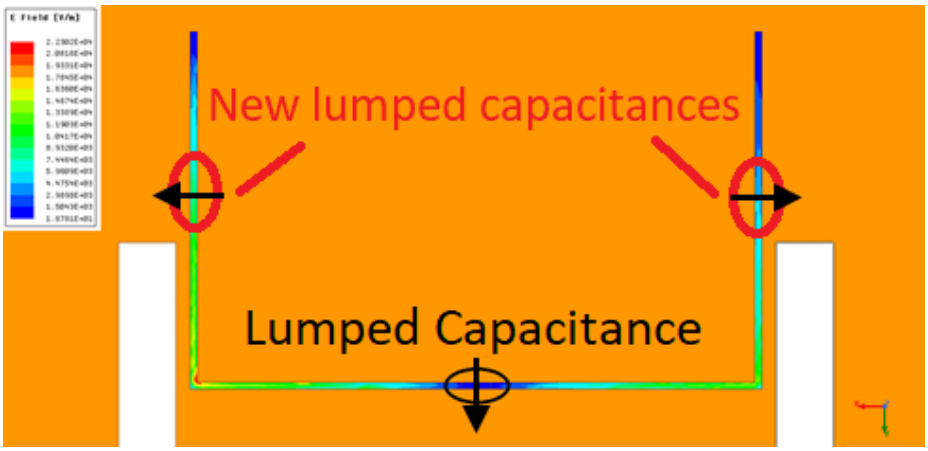

Figure 4.16: The electric field magnitudes along the lengthened slotline; Because lumped capacitances couple using electric fields, moving them to the electric field maxima would allow for an expanded tuning range using the same capacitance values. The arrows indicate the integration lines across the lumped (shunt) capacitances.

By looking at the electric field strength along the slotline in Figure 4.16, the electric field maxima could be located. The lumped capacitances couple using electric field coupling, so moving the lumped capacitances to these locations would allow for increased tuning sensitivity. This expanded the tuning range of the mutual coupling nulls to that shown in Figure 4.17, covering nearly the full S-band (2.2 GHz to 4 GHz).

This response was almost exactly what was desired for the mutual coupling tuning design between slots, but it was thought that the nulls could be deepened to create even more isolation between the slots. By widening the slotline between the antennas, the mutual coupling was decreased significantly at the nulls due to the decreased magnetic field cancellation across the slotline. This can be seen in Figure 4.18.

4.4 Spatial Design Adjustments

After the slotline based design was shown to work properly for tuning mutual coupling, the current design needed to be modified to fit properly within a slot antenna array. The

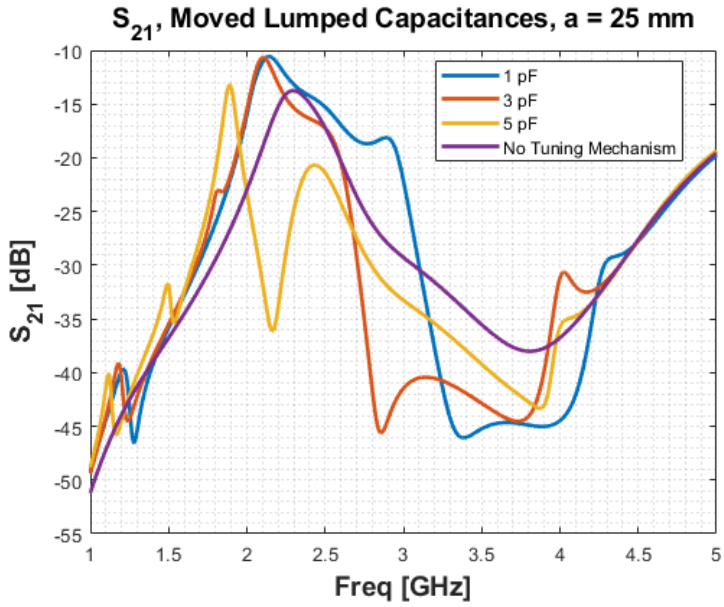

Figure 4.17: The mutual coupling response with the moved lumped capacitances; This change did indeed increase the tuning range to almost the full S-band, from 2.2 GHz to 4 GHz.

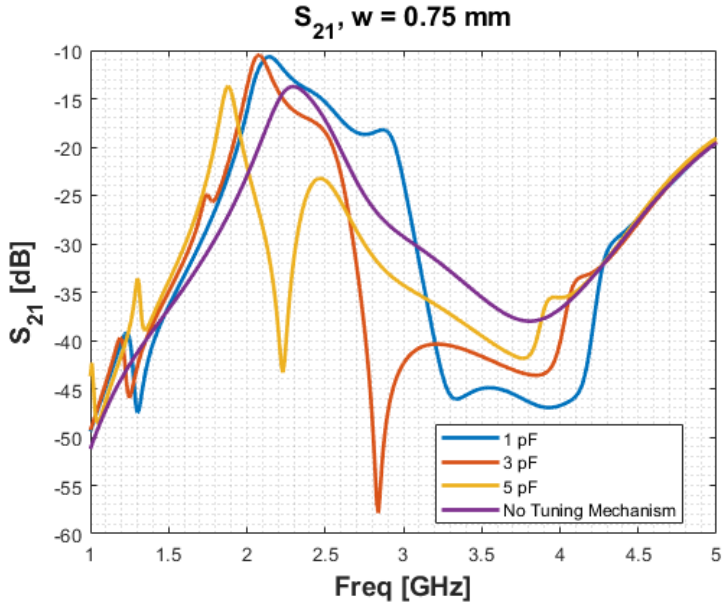

Figure 4.18: The mutual coupling response with widened slotline; This gave decreased magnetic field interference across the slotline, allowing for deeper nulls in mutual coupling.

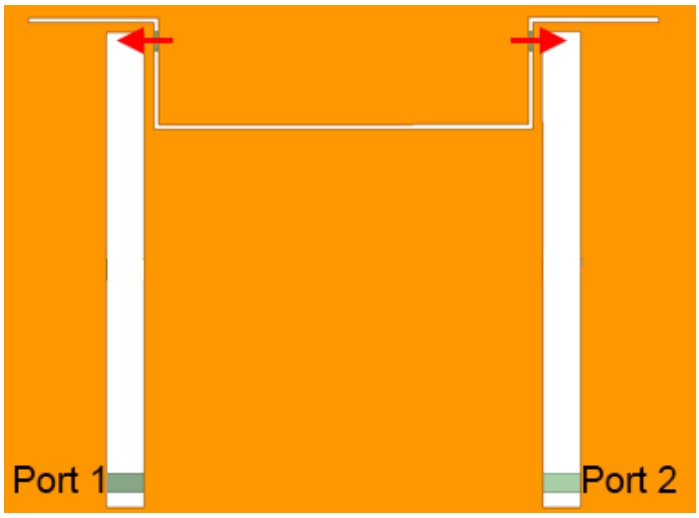

Figure 4.19: The modified mutual coupling tuning design to account for spacing issues that the old slotline based design would have when put into a full array; The arrows indicate the integration lines across the lumped (shunt) capacitances.

slotline extended too far past the end of the slot antennas and was coupling to other array elements that the tuning mechanism was not supposed to affect. In order to fix this issue, the ends of the slotline were bent 90 degrees around the end of the slot. This change can be seen in Figure 4.19. This modification, while fixing the spatial issues, did result in the smaller tuning range (from 2.4 GHz to 3.8 GHz) depicted in Figure 4.20.

With this design modifications, the lumped capacitances had to be moved slightly, so the electric field strength along the slotline was looked at again to see where these elements needed to be moved to. Figure 4.21 shows that the capacitances only needed to be shifted a bit to match up with the electric field maxima in the portion of the slotline parallel to the slot antennas, but another electric field maximum had developed in the center of the slotline. By adding another lumped capacitance at this location, the tuning range was extended to cover the full 2 GHz to 4 GHz range seen in Figure 4.22.

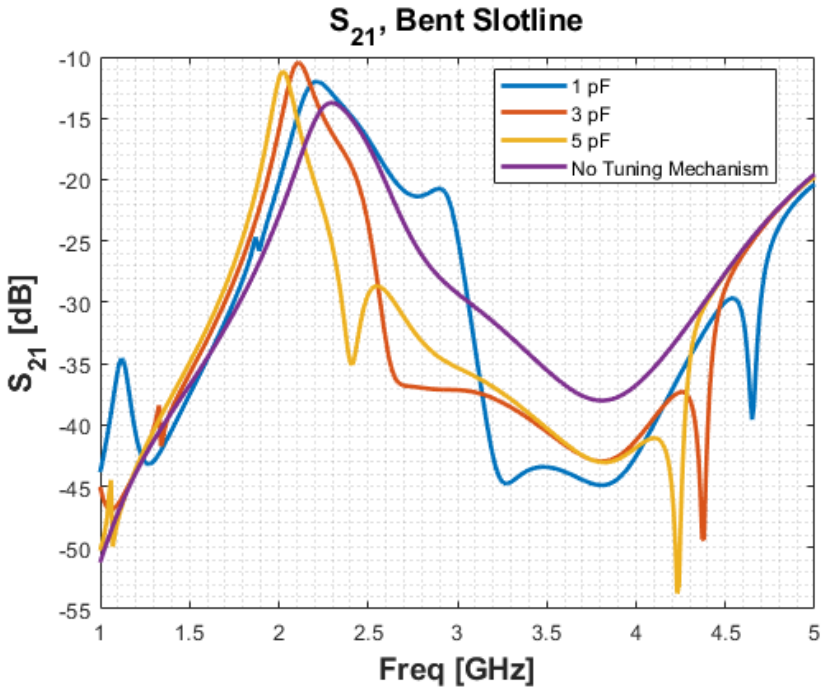

Figure 4.20: The mutual coupling response of the modified design; The tuning range was reduced some in exchange for necessary geometry modifications

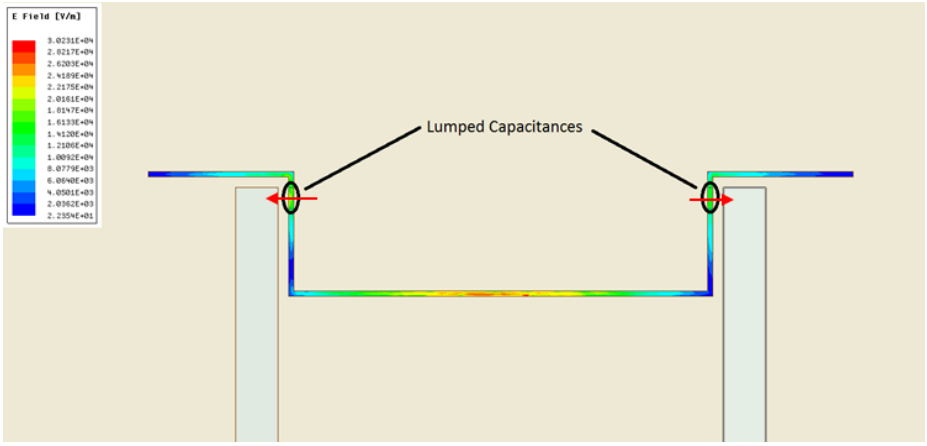

Figure 4.21: The electric field strength along the bent slotline; The design change moved the locations of the electric field maxima, and also caused the development of a maximum at the original lumped capacitance location, indicating where the lumped capacitances needed to be moved to on this new slotline shape. The arrows indicate the integration lines across the lumped (shunt) capacitances.

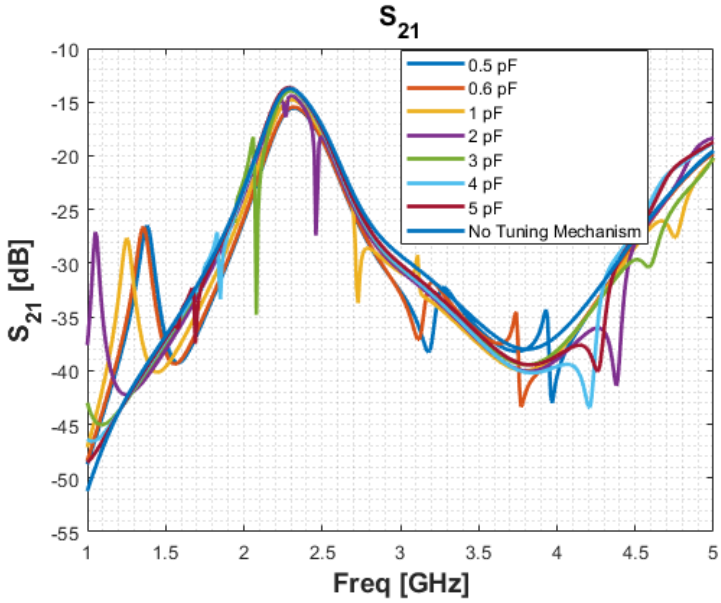

Figure 4.22: The mutual coupling tuning response with the adjusted lumped capacitance locations; This design achieved mutual coupling null tuning across the full 2 GHz to 4 GHz band.

4.5 Mutual Coupling Tuning in Tunable Antennas

With successful tuning at a set antenna frequency, this tuning device could then be used for a frequency reconfigurable antenna. A lumped RLC element was added to the center of the slot antenna, to represent a tuning mechanism for the slot. This change caused issues developing mutual coupling nulls along S-band.

After several modifications to unsuccessfully attempt to reintroduce these mutual coupling nulls, it was thought that the addition of the lumped RLC ports across the slot could be causing unexpected changes in mutual coupling, so a new tunable antenna design was introduced. Figure 4.23 shows this design, which relies on a circular metal plate to capacitively load the antenna at its center [20]. The disc could be moved vertically above the antenna in order to tune the operating frequency of the antenna in the 2 GHz to 4 GHz band.

First the baseline mutual coupling for a two element array made up of these antennas

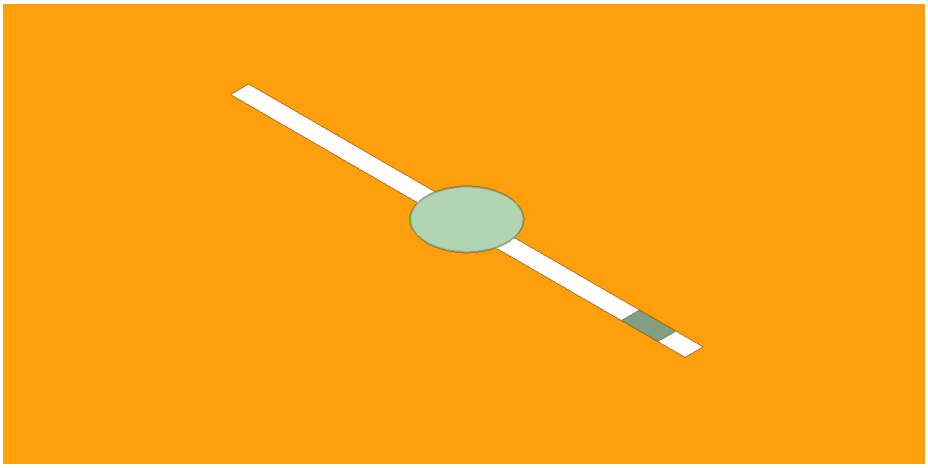

Figure 4.23: The new tunable antenna design that was shown to be achieve full 2 GHz to 4 GHz frequency tuning of the slot

with no tuning mechanism needed to be found across the tuning band. Several plate heights were simulated to get the mutual coupling response of several points along the 2 GHz to 4 GHz band. This range of mutual coupling responses can be seen in Figure 4.24.

From here, the slotline tuning mechanism was reintroduced and the effects of tuning the lumped capacitances along the slotline was investigated to see if mutual coupling nulls could be introduced to this mutual coupling response. From this, nulls were redeveloped along the tuning range and could be adjusted across the band with the slotline lumped capacitance. For this mutual coupling design to function as needed for the array, the nulls only needed to be developed at the tunable resonance of the antenna, so capacitance values were adjusted at each antenna resonant frequency simulated to find one that developed a mutual coupling null at those resonant frequencies. A few of these developed nulls can be seen in Figure 4.25 for an antenna tuned to 1.9 GHz, Figure 4.26 for an antenna tuned to 3.25 GHz, and Figure 4.27 for an antenna tuned to 3.85 GHz.

Figure 4.28 and Figure 4.29 show the currents and electric fields, respectively, of the array with the mutual coupling tuning mechanism. These indicate that the slotline is acting as a direct coupling path as suspected between the two slot antennas, allowing the cancellation

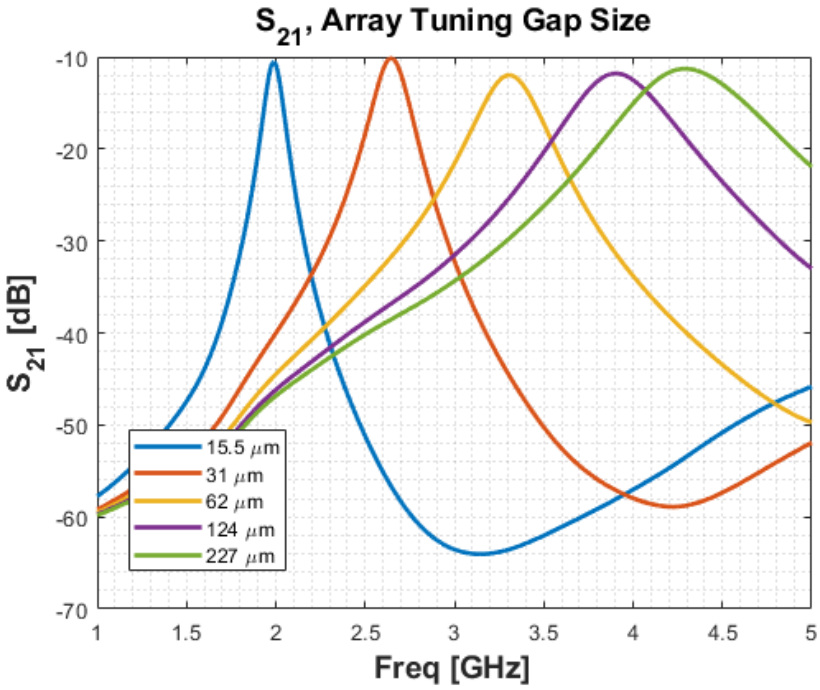

Figure 4.24: The baseline mutual coupling response of the tunable antenna at several different plate heights

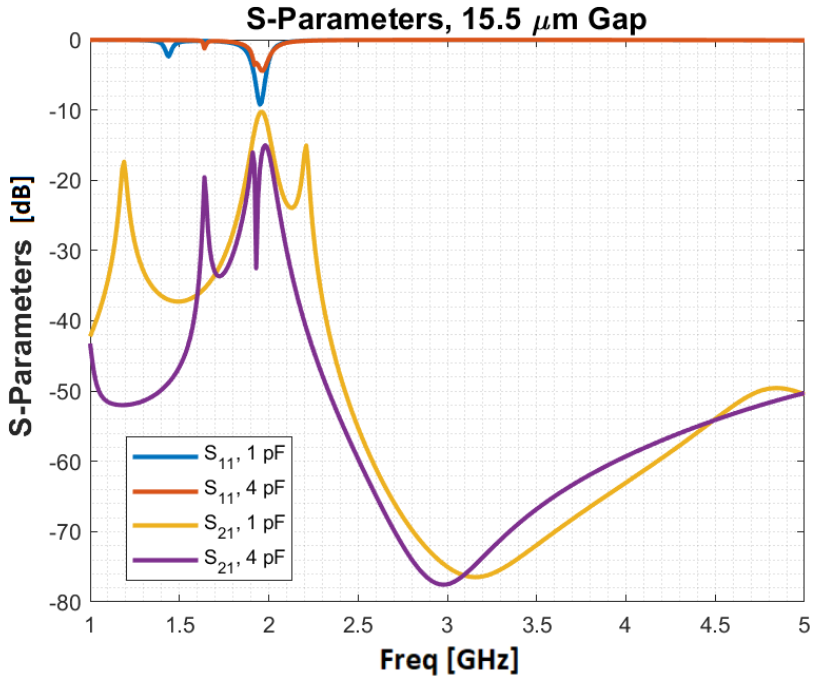

Figure 4.25: A mutual coupling null at the resonance of the antennas tuned to approximately 2 GHz

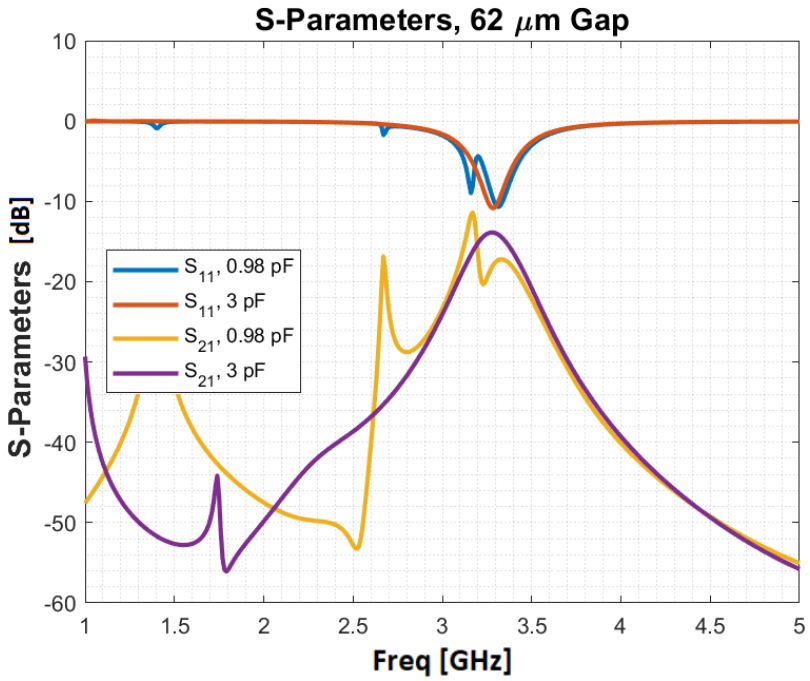

Figure 4.26: A mutual coupling null at the resonance of the antennas tuned to approximately 3.25 GHz

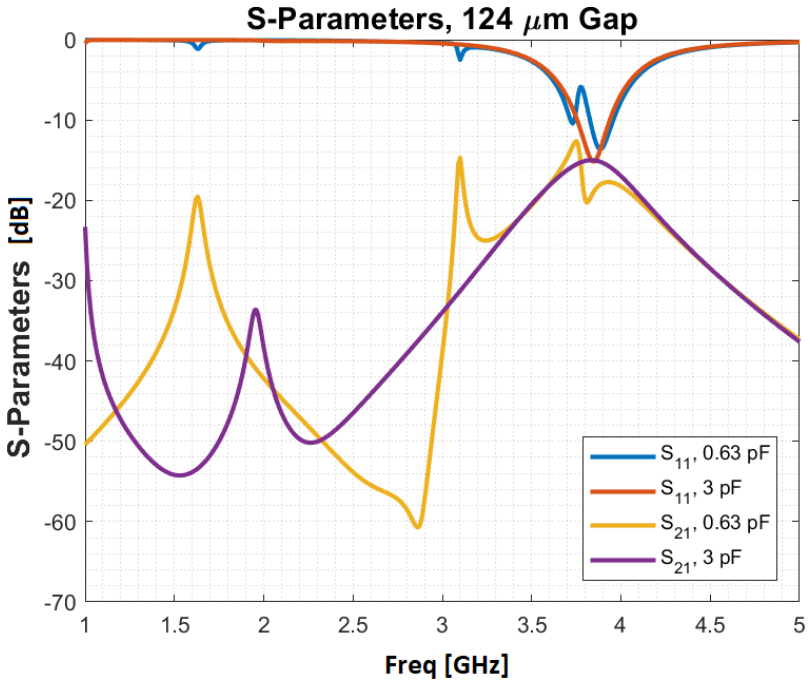

Figure 4.27: A mutual coupling null at the resonance of the antennas tuned to approximately 3.8 GHz

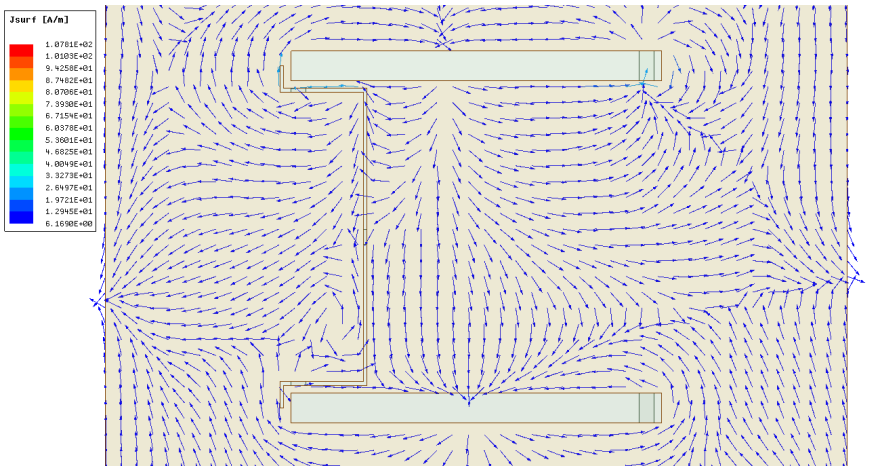

Figure 4.28: The currents on the array with the coupling mechanism; The slotline is directly coupling between the antennas.

to occur.

4.6 Radiation Behavior

In order to analyze the impact of the transition, the radiation behavior of the arrays seen in Figure 4.30 (without the mutual coupling tuning mechanism) and Figure 4.31 (with the mechanism) needed to be compared. This behavior is shown using the co-polarization and cross-polarization in Figure 4.32 for the XZ-plane and in Figure 4.33 for the YZ-plane. For these simulations, the operating frequency investigated was in a null in mutual coupling at 3.2 GHz developed by the mutual coupling tuning mechanism. In both cases, co-polarization in the Z direction of the array decreased by about 2.56 dB. The cross polarization in the XZ-plane stayed about the same as without the tuning mechanism, with a maximum of about -14 dB. In the YZ plane, co-polarization decreased by about the same amount in the Z direction (about 2.56 dB difference), with the cross-polarization of the array with the tuning mechanism having a maximum of about -16 dB compared to the maximum of about -18 dB for the array with no mechanism.

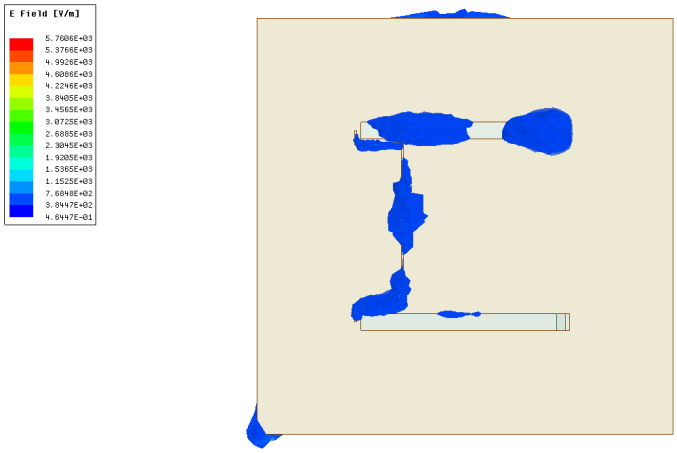

Figure 4.29: The electric fields on the array with the coupling mechanism; The slotline can be seen acting as a direct coupling path.

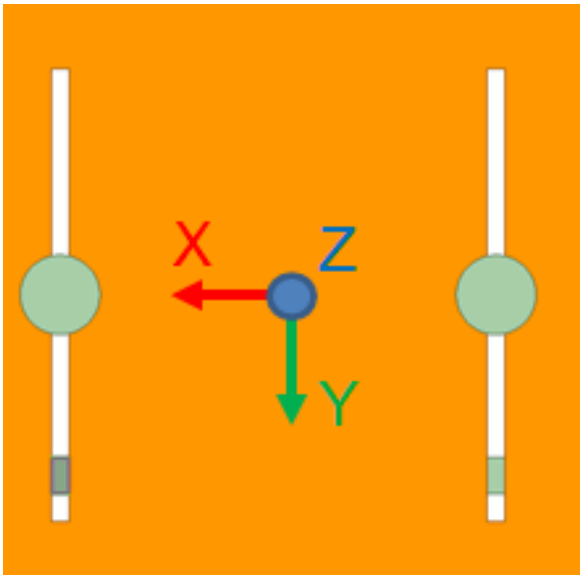

Figure 4.30: The array without a mutual coupling tuning mechanism, with defined axes

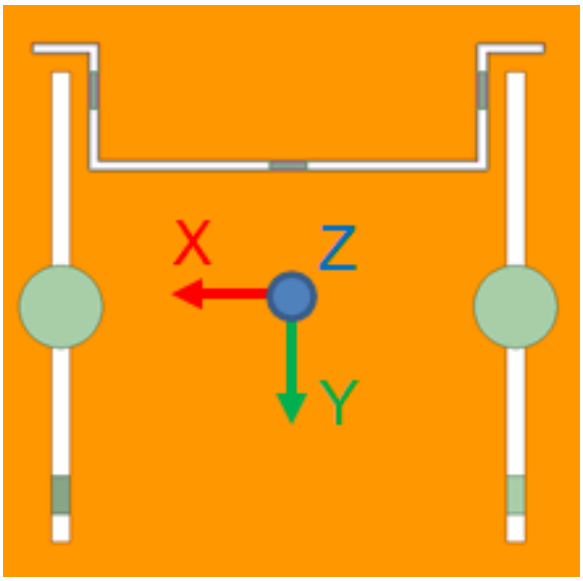

Figure 4.31: The array with a mutual coupling tuning mechanism, with defined axes

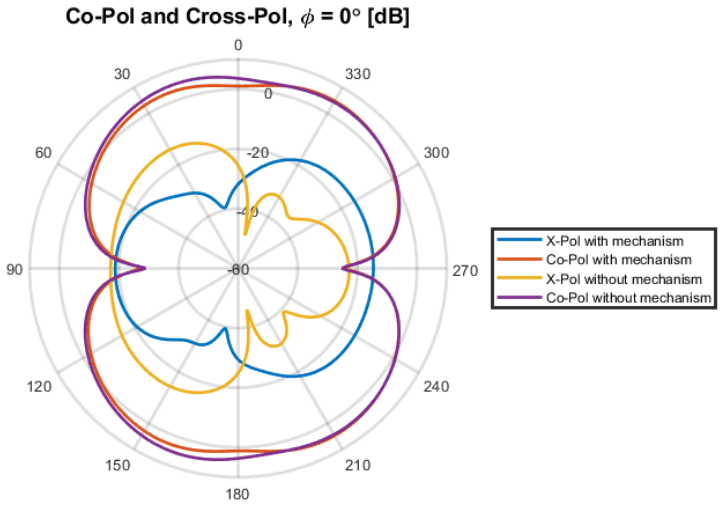

Figure 4.32: The co-polarization and cross-polarization of the two arrays in the XZ-plane; The tuning mechanism caused a decrease in co-polarization in the Z direction of about 2.56 dB. The cross-polarization remained below -14 dB at all angles.

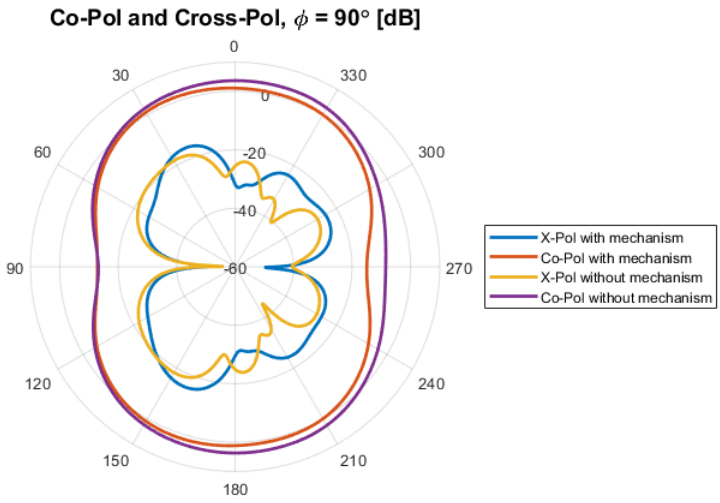

Figure 4.33: The co-polarization and cross-polarization of the two arrays in the YZ-plane; The tuning mechanism caused a decrease in co-polarization in the Z direction of about 2.56 dB. The cross-polarization remained below -16 dB at all angles.

These results showed that the array had little effect on cross-polarization, but the effects of the tuning mechanism on co-polarization. This decrease in co-polarization at the null frequency imparted by the tuning mechanism could be an indication that the tuning mechanism is repressing the radiation of the slots in order to accomplish the decrease in mutual coupling. This will need further investigation to determine further effects the mutual coupling tuning mechanism has on radiation.

4.7 Conclusion

This chapter discusses a novel method for tuning mutual coupling in slot antenna arrays. This design uses slotline as a direct coupling path to counteract the radiative coupling between the slots. This results in a reduction in static array mutual coupling by 7 dB to 10 dB at its operating frequency, and in tunable array mutual coupling by about 5 dB to

10 dB at its operating frequency. With this design in tunable arrays, however, tuning is a bit more difficult, as the capacitances loading the slotline require different values for each operating frequency. This will require either a table of values for operation or another mechanism for automatically shifting the null into place at the operating frequency. The null in mutual coupling is also connected to a peak in mutual coupling, which requires caution to avoid boosting mutual coupling rather than mitigating it. With this coupling tuning mechanism, a bandwidth of 80 to 90 MHz of cancellation at -3 dB was seen for the sample frequencies in the final mutual coupling tuning design. In order to increase the ability of this design to reduce mutual coupling and increase the bandwidth, a circuit model needed to be developed to allow capacitances and slotline dimensions to be calculated to best cancel out the mutual coupling.

Chapter 5

Mutual Coupling Tuning Transmission Line Model

5.1 Design Modifications

After some small nulls were developed at the resonances of the slot at different tuned frequencies, it was determined that a circuit model of the tuning structure would be useful for determining the exact dimensions of the structure that would be needed to properly cancel out the mutual coupling between antennas at the operating frequency of the array.

A few modifications to the structure were made to simplify modeling, with a visual depiction of the structure MATLAB is modeling seen in Figure 5.1. This modification did not remove the developed nulls in S_{21}, making it viable for use. Because current cancellation between the slot and slotline had caused issues with the current direction on the slotline previously (the slot currents had overridden the slotline currents, preventing typical slotline current patterns from occurring), the currents shown in Figure 5.2 on the modified model were checked. The main modification is the movement of the lumped capacitance elements from the coupled portions of the slotline to the non-coupled portion. This would make modeling easier, as the method of representing the coupled slotline portions of the design are significantly more complicated than just adding a lumped capacitance to a transmission line, which the new design allows. The width of the slotline was widened to be the same as the slot antenna (0.5 mm to 1 mm), as the method used could only account

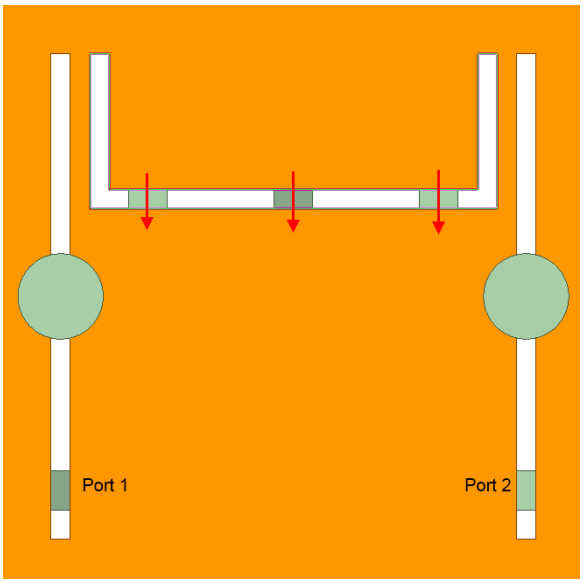

Figure 5.1: The modified coupling tuning design

for slotlines of the same width. Analysis of different widths of line would require c and π mode analysis, which is not well studied for slotline. However, this representation would be sufficient to gain an understanding of the behavior of the structure for application to a design with varied slotline widths.

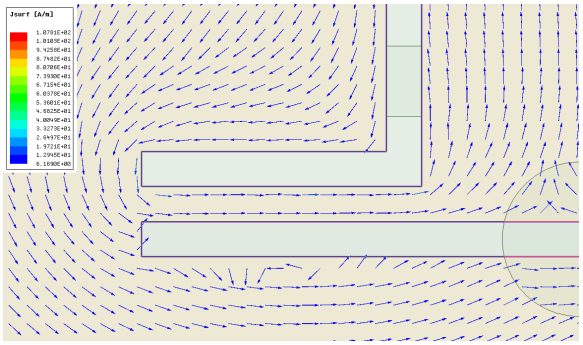

Figure 5.2: The current flow on the modified coupling tuning design; The slotline is exhibiting typical slotline current behavior, showing that the design functions as intended.

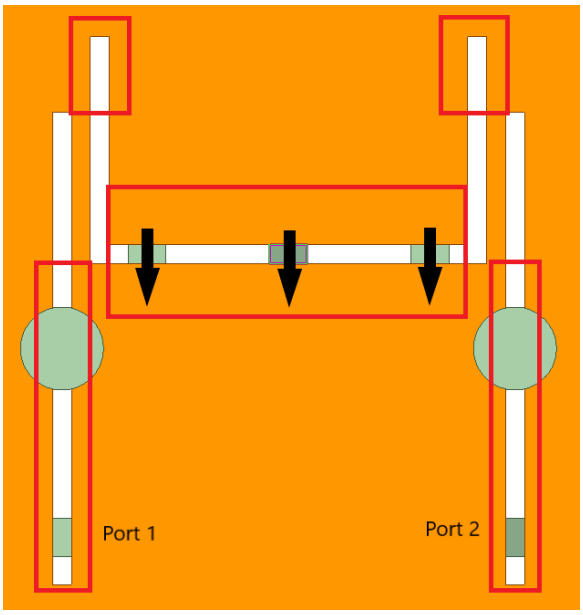

Figure 5.3: The areas that can be represented using ABCD matrices for slotline and shunt lumped capacitances; The plates above the slot antennas can be modeled as a lumped capacitance in a range from approximately 0.5 to 2.5 pF.

5.2 Slotline Impedance Calculation

A representation of both the slotline and the lumped capacitances as an ABCD or S matrix for the regions indicated in red in Figure 5.3 is necessary in order to properly cascade these structures with the rest of the portions of the model.

The capacitances are straightforward to model as ABCD parameters. The ABCD matrix for a lumped capacitance element is

$$ABCD_{cap} = \begin{bmatrix} 1 & 0 \\ j\omega C & 1 \end{bmatrix}, \tag{5.1}$$

which can be converted as needed to other parameters for cascading. The slotline representation is more complex, as outlined by Cohn in [23]. Using Cohn's method, the characteristic impedance can be determined for the slotline, then used in typical transmission

line ABCD parameter calculations to develop a matrix for cascading the transmission lines with the rest of the system:

$$ABCD_{TL} = \begin{bmatrix} cos\beta\ell & jZ_0 sin\beta\ell \\ jY_0 sin\beta\ell & cos\beta\ell \end{bmatrix}, \tag{5.2}$$

where $Y_0 = \frac{1}{Z_0}$, $\beta = \frac{2\pi}{\lambda}$, and ℓ is the length of line.

5.3 Coupled Slotline Impedance Matrix Calculation

The other major part of the mutual coupling tuning design that needed to be modeled was the region of coupling between the slotline and slot antenna. This could not use the previous slot coupling method, as that method relied on far-field approximations, whereas the slot and slotline were close enough to need near-field analysis. In order to find the impedance matrix of this section to properly cascade with the rest of the system, The even and odd mode impedance of the coupled slotline must be found. This can be accomplished using the method developed by Simons and Akora [24]. This calculation produces the even and odd mode impedances for the slotline, which can then be used to find the impedance matrix of the coupled slotline.

From here, these impedances need to be converted into a capacitance matrix built off of self and mutual capacitances for each line [25]. In order to make this conversion, even and odd mode impedances need to be converted to even and odd mode capacitances, using

$$C_{o,e} = \frac{1}{v_p Z_{0o,e}}. \tag{5.3}$$

Once these capacitances are obtained, the capacitance matrix can be determined. In this

case,

$$C_{self} = C_{11} = C_{22} = C_e \tag{5.4}$$

and

$$C_{mutual} = C_{12} = C21 = \frac{C_o - C_e}{2} \tag{5.5}$$

allow even and odd mode capacitance to be converted to self (C_{11} and C_{22}) and mutual (C_{12} and C_{21}) capacitance. From here, the capacitance matrix can be constructed:

$$[C] = \begin{bmatrix} C_{self,11} + C_{mutual} & -C_{mutual,12} \\ -C_{mutual,21} & C_{self,22} + C_{mutual} \end{bmatrix} \tag{5.6}$$

which can then be converted to

$$[y] = j\omega[C]. \tag{5.7}$$

After this capacitance matrix was found, an inductance matrix for the system needed to be found as well. However, this is straightforward to find from the previous method. Repeating the previous capacitance matrix calculation with air replacing the dielectric,then plugging that matrix into

$$[L] = \mu_0\epsilon_0[C_{air}]^{-1} \tag{5.8}$$

which can then be converted through

$$[z] = j\omega[L]. \tag{5.9}$$

to obtain the necessary matrix for calculation. From here, previously developed code can be used to take these matrices as inputs and produce an impedance matrix representing the coupled slotlines [26]. These are used to find characteristic impedance and admittance of

the system through

$$Yc = [z]^{-1} * [\hat{V}] * [\gamma]/[\hat{V}] \tag{5.10}$$

and

$$Zc = [y]^{-1} * [\hat{I}] * [\gamma]/[\hat{I}] \tag{5.11}$$

with $\hat{V}$ and $\hat{I}$ being the modal voltages and currents and γ being the square root of the eigenvalues for the system, based on modal analysis. After this is finished, an impedance matrix is produced for the coupled line system.

5.4 Four Port Simplification

The coupled slotline model does not fully represent the coupled slotline section of the mutual coupling tuning design. The produced Z-matrix is for a four port network, with a port at both ends of each slotline. However, Figure 5.4 shows that two of these ports are loaded in this model, turning the coupled section into a two port network. In order to properly represent this loading, the obtained four port parameters must be modified to represent the loaded version of this network.

In order to modify these parameters, Mason's Rule must be utilized, which necessitates the creation of a signal flow graph for this network, beginning with the unloaded four port network [27]. The graph works in terms of S-parameters, so each port is defined with an 'a' and 'b' node. Figure 5.5 shows these nodes connecting to one another, with every 'a' connecting to every 'b' in order to represent each of the parameters in the S-matrix. This results in a representation of the four port network, but does not yet reduce to the loaded two port network needed for the circuit model. In order to do this, a few additions need to be made to the signal flow graph. Adding another path to ports 3 and 4 allows the loads to be represented. This change can be seen in Figure 5.6. These paths flow in the opposite

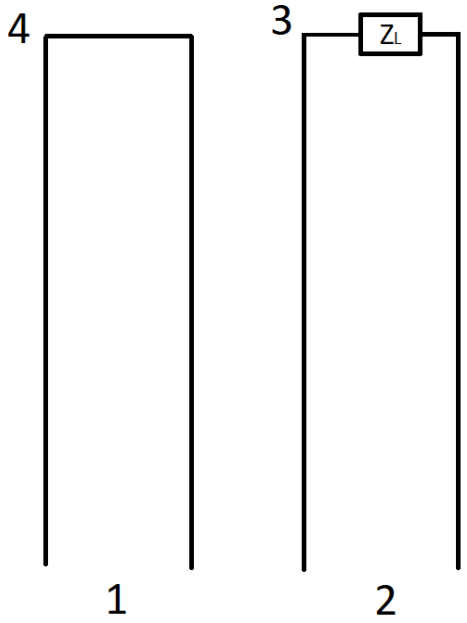

Figure 5.4: The four port coupled slotline network with two loaded ports (port 4 is shorted and port 3 is loaded with a transmission line stub.)

direction of the network parameters (from 'b' to 'a') to represent an external load on the port. However, to properly represent the effects of the loads, simply representing them as an impedance is not enough. These loaded ports must use the reflection coefficient from the load in order to properly represent the network. This reflection coefficient is calculated as

$$\Gamma_L = \frac{Z_L - Z_0}{Z_L + Z_0} \tag{5.12}$$

Once the network is defined, Mason's Rule can be used to produce equations for S_{11}, S_{12}, S_{21}, and S_{22}. This is done using MATLAB's mason.m program. This program uses defined nodes and connections to interpret a signal flow graph and produce equations to find network parameters based on those graphs. In order to use this code, the nodes in the

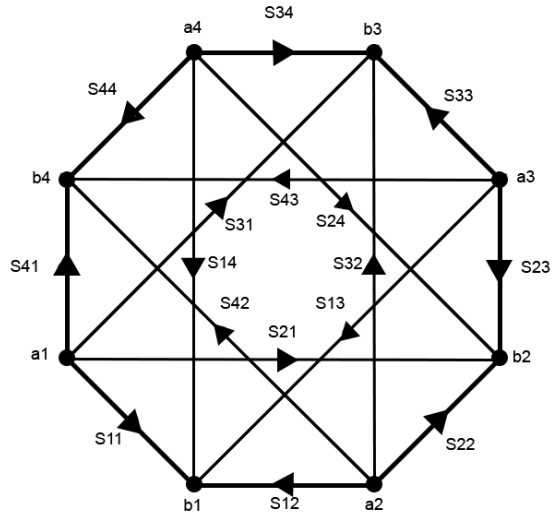

Figure 5.5: The signal flow graph of the unloaded four port network

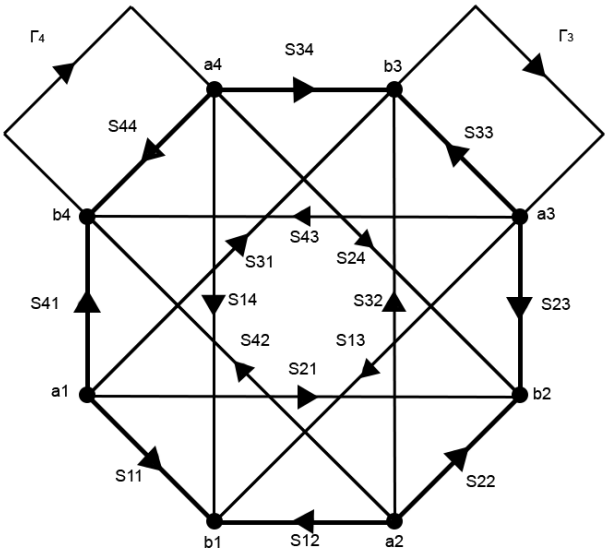

Figure 5.6: The signal flow graph of the loaded four port network

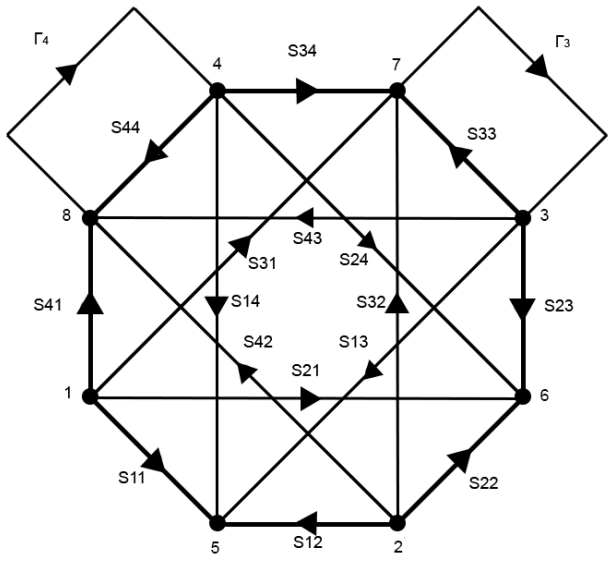

Figure 5.7: The signal flow graph with nodes labeled for use with mason.m

signal flow graph had to be redefined. This change can be seen in Figure 5.7. This could then be converted to the input format for mason.m:

Index	Start Node	End Node	Label
1	1	5	S11
2	1	6	S21
3	2	6	S22
...			

Running the program, using

```
[Numerator, Denominator] = mason(...
'Text File Name.txt', Starting Node, Stopping Node);
```

allows the specific desired S-parameter to be determined (thus this line must be run with the appropriate values for each S-parameter equation desired). Using this code results in

the the equations for S_{11}, S_{12}, S_{21}, and S_{22},

$$\begin{aligned}
S'_{11} = (&S_{11} * (1 - (S_{33} * \Gamma_3 + S_{43} * \Gamma_4 * S_{34} * \Gamma_3 + S_{44} * \Gamma_4) + \\
&(S_{33} * \Gamma_3 * S_{44} * \Gamma_4)) + S_{41} * \Gamma_4 * S_{34} * \Gamma_3 * S_{13} \\
&+ S_{41} * \Gamma_4 * S_{14} * (1 - (S_{33} * \Gamma_3)) + S_{31} * \Gamma_3 * \\
&S_{13} * (1 - (S_{44} * \Gamma_4)) + S_{31} * \Gamma_3 * S_{43} * \Gamma_4 * S_{14}) \div \\
&(1 - (S_{33} * \Gamma_3 + S_{43} * \Gamma_4 * S_{34} * \Gamma_3 + S_{44} * \Gamma_4) + \\
&(S_{33} * \Gamma_3 * S_{44} * \Gamma_4))
\end{aligned} \tag{5.13}$$

$$\begin{aligned}
S'_{12} = (&S_{12} * (1 - (S_{33} * \Gamma_3 + S_{43} * \Gamma_4 * S_{34} * \Gamma_3 + S_{44} * \Gamma_4) + \\
&(S_{33} * \Gamma_3 * S_{44} * \Gamma_4)) + S_{42} * \Gamma_4 * S_{34} * \Gamma_3 * S_{13} \\
&+ S_{42} * \Gamma_4 * S_{14} * (1 - (S_{33} * \Gamma_3)) + S_{32} * \Gamma_3 * \\
&S_{13} * (1 - (S_{44} * \Gamma_4)) + S_{32} * \Gamma_3 * S_{43} * \Gamma_4 * S_{14}) \div \\
&(1 - (S_{33} * \Gamma_3 + S_{43} * \Gamma_4 * S_{34} * \Gamma_3 + S_{44} * \Gamma_4) + \\
&(S_{33} * \Gamma_3 * S_{44} * \Gamma_4))
\end{aligned} \tag{5.14}$$

$$\begin{aligned}
S'_{21} = (&S_{21} * (1 - (S_{33} * \Gamma_3 + S_{43} * \Gamma_4 * S_{34} * \Gamma_3 + S_{44} * \Gamma_4) + \\
&(S_{33} * \Gamma_3 * S_{44} * \Gamma_4)) + S_{41} * \Gamma_4 * S_{34} * \Gamma_3 * S_{23} \\
&+ S_{41} * \Gamma_4 * S_{24} * (1 - (S_{33} * \Gamma_3)) + S_{31} * \Gamma_3 * \\
&S_{23} * (1 - (S_{44} * \Gamma_4)) + S_{31} * \Gamma_3 * S_{43} * \Gamma_4 * S_{24}) \div \\
&(1 - (S_{33} * \Gamma_3 + S_{43} * \Gamma_4 * S_{34} * \Gamma_3 + S_{44} * \Gamma_4) + \\
&(S_{33} * \Gamma_3 * S_{44} * \Gamma_4))
\end{aligned} \tag{5.15}$$

$$
\begin{aligned}
S'_{22} = (S_{22} * (1 - (S_{33} * \Gamma_3 + S_{43} * \Gamma_4 * S_{34} * \Gamma_3 + S_{44} * \Gamma_4) + \\
(S_{33} * \Gamma_3 * S_{44} * \Gamma_4)) + S_{42} * \Gamma_4 * S_{34} * \Gamma_3 * S_{23} \\
+ S_{42} * \Gamma_4 * S_{24} * (1 - (S_{33} * \Gamma_3)) + S_{32} * \Gamma_3 * \\
S_{23} * (1 - (S_{44} * \Gamma_4)) + S_{32} * \Gamma_3 * S_{43} * \Gamma_4 * S_{24}) \div \\
(1 - (S_{33} * \Gamma_3 + S_{43} * \Gamma_4 * S_{34} * \Gamma_3 + S_{44} * \Gamma_4) + \\
(S_{33} * \Gamma_3 * S_{44} * \Gamma_4))
\end{aligned}
\tag{5.16}
$$

where S'_{11}, S'_{12}, S'_{21}, and S'_{22} are the two port parameters of the network once ports 3 and 4 are loaded, and Γ_3 and Γ_4 are the reflection coefficients of the loads on ports 3 and 4 respectively, as calculated. These equations result in S-parameters able to be cascaded with the other portions of the circuit model, connected to both the center slotline of the design and the rest of the slot antenna (The four port to two port model includes the coupled portion of the slot antenna).

5.5 Slot Radiation Conductance

The final portion of the model needed is a representation of the losses on the slot due to radiation. The calculation involves finding the current on the slot using

$$
I = \int_0^{\pi} \left(\sin\left(\frac{\pi L'_s}{\lambda} \cos\theta \right) / \cos\theta \right)^2 \sin\theta^3 \, d\theta,
$$

then using

$$
G_r = \frac{I}{120\pi^2}
$$

to find the radiation conductance to be used as a lumped element across the port of the slot [28].

5.6 Admittance Calculations of Coupled Slot Antennas

Before the main part of the structure could be modeled, the coupling between the slots had to be found. This used previously developed code, based on [29], to find this coupling [30]. The paper goes into detail about finding mutual impedance between two dipoles, and through that derivation, adapts the equations for two slot antennas. Maxwell's equations must be used to find the magnetic field at each antenna from the other antenna, which can then be used in one of two equations depending on the parameters of the structure:

$$Y_{12} = \frac{I_{12}}{V_2} = \frac{-1}{V_1 V_2} \iint_{S_2} H_{21} M_2 \, dS_2 \tag{5.17}$$

if all materials are reciprocal and the currents are fully real functions, or

$$Y_{12} = \frac{I_{12}}{V_2} = \frac{-1}{V_1^* V_2} \iint_{S_1} H_{12} M_1^* \, dS_1 \tag{5.18}$$

for nonreciprocal materials or currents with non-real components. The code works on this principle, producing an N×N admittance matrix, with N being the number of coupled slots. In this case, the matrix will be 2×2.

5.7 Full Model

Cascading all of these components together yielded an S_{21} of the network that had some features of the S_{21} from HFSS simulations, but was significantly different overall from simulation data that an investigation needed to be conducted into issues with the model. The initial trace exhibited behavior that hinted that the coupling between the slot antennas was not correct. Looking into the slot coupling code further, it was found that the primary method of calculation yielded a coupling S_{21} of -500 dB, indicating that the code was not

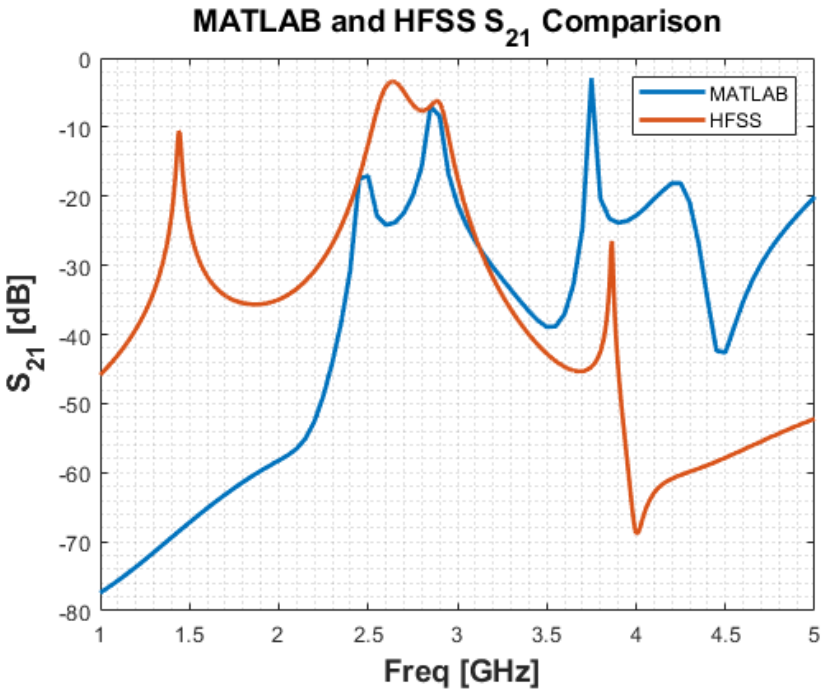

Figure 5.8: A comparison of the initial model between HFSS and MATLAB

calculating the coupling, as that value approaches the base noise level of MATLAB. After some investigation, it was found that the code produced voltage distributions along each slot that were stuck in a second order mode. This was the incorrect behavior, and based on information from [30], indicated that something in the code was not working properly.

After this discovery, updated code from [30] was used to produce reasonable slot mutual coupling responses. Figure 5.9 shows that the code performed as intended and matched the mutual coupling behavior of the slots relatively well. However, upon further investigation, it was found that the coupling generated in MATLAB was not tuning with the operating frequency of the slot antenna. In order to try to counteract this effect, a method of modifying the slot length to change the coupling behavior was theorized. Effectively, the slot length would need to be half of a wavelength long at the desired operating frequency, translating to

$$L = \frac{c}{2\sqrt{\epsilon_r} f}$$

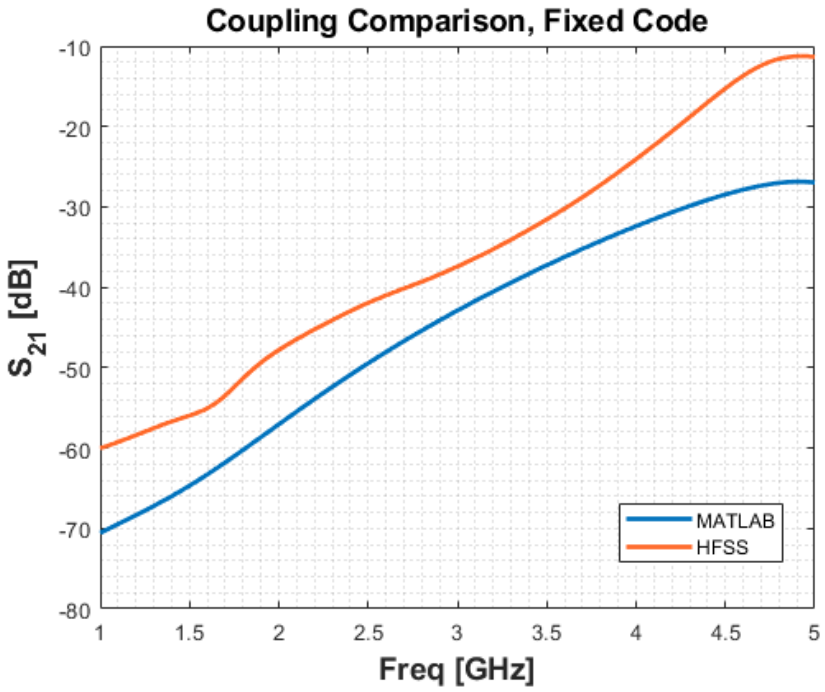

Figure 5.9: The mutual coupling from HFSS for a slot with no tuning mechanism versus the mutual coupling from MATLAB

in the mutual coupling code. After this change in slot length was implemented, as well as making sure the port was moved to the correct (50 Ω) point on the slot as it changed effective length, the model was re-simulated. This produced behavior that tuned in frequency, but did not match the mutual coupling of the baseline array from HFSS, as shown in Figure 5.10. When this coupling was applied to the overall model, it also yielded an S_{21} very different from simulation. This comparison can be seen in Figure 5.11.

It was theorized that the issue was mainly in this slot mutual coupling, so a case was constructed that did not rely on the MATLAB coupling code. The model of the rest of the structure without the base slot mutual coupling was constructed and S-parameter data was pulled, and was then combined with S-parameter data from the baseline array simulation in HFSS. Once these parameters were combined, an S_{21} graph was produced to compare to HFSS simulations of the full structure. This comparison can be seen in Figure 5.12. This

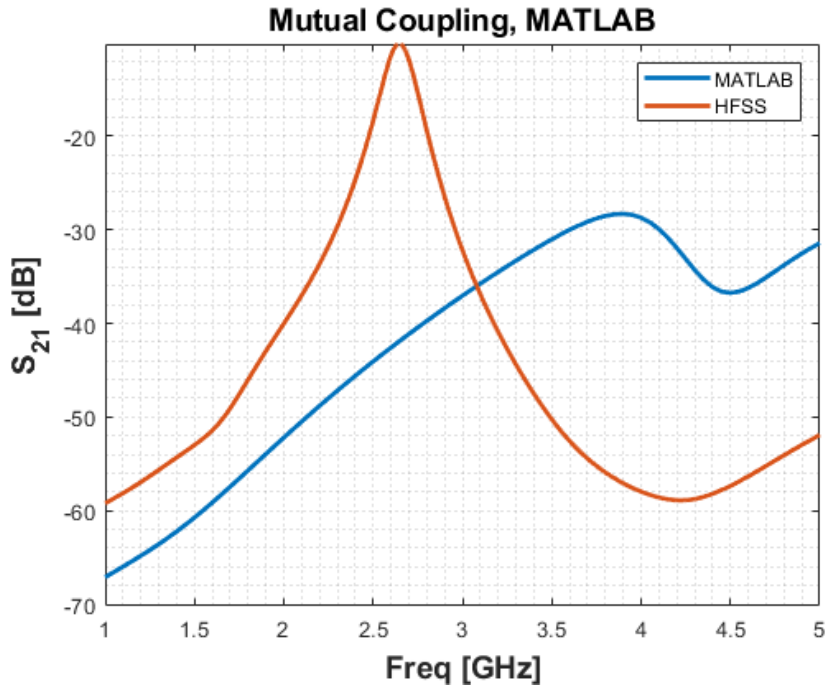

Figure 5.10: A comparison of the mutual coupling between HFSS and MATLAB

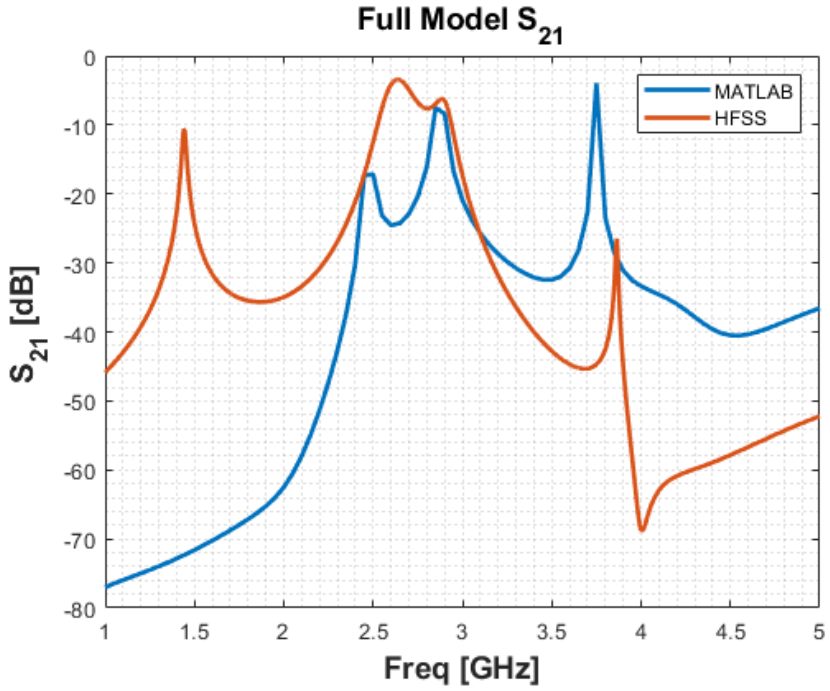

Figure 5.11: A comparison of S_{21} of the full model between HFSS and MATLAB

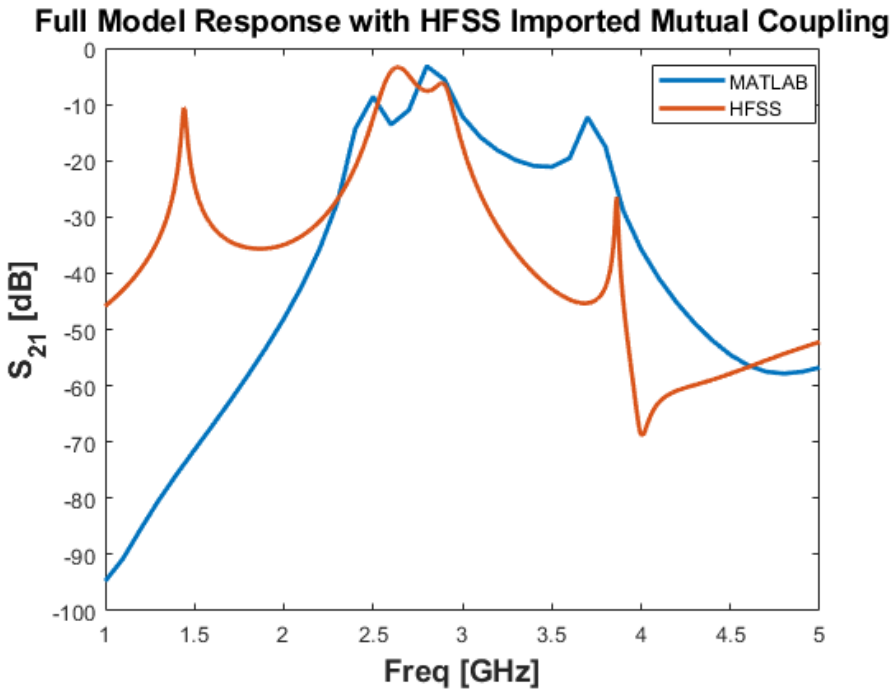

Figure 5.12: The full model using mutual coupling data from HFSS for a slot array with no mutual coupling tuning mechanism

plot had a few discrepancies, such as a missing peak just under 2 GHz created by mutual coupling tuning mechanism, but the most relevant portion of the model, the area around the antenna resonance, matched up very well. There were some slight frequency shifts in peaks and nulls, but this could be fixed with some minor tweaking of the transmission line and capacitance parameters in the slotline portion of the model.

Chapter 6

Conclusions and Future Work

6.1 Scientific Impact

In this thesis, several novel projects in high-power tunable filtenna arrays were demonstrated. First is the size reduction of slotline to coplanar waveguide stubs for smaller transition geometry. By meandering the perimeter of a stub on a planar coplanar waveguide to slotline transition, the performance of the transition can be maintained (to an extent) while reducing the stub size, typically defined by radius for a circular or radial stub and side length for a square stub, by 50% or more. This allows for easier implementation of these transitions into other designs, such as phased arrays, and can possibly be extended to other transmission line transitions that rely on balun structures.

A novel side-loaded slot antenna design was created that was capable of tuning 1.4 GHz (with a tuning ratio of 60:1 in terms of necessary capacitance) without experiencing significant loss in radiation efficiency at the operating frequency of the antenna. This design reinforced ideas about side-loading slot antennas while also providing a design that has potential for full S-band tuning without significant radiation efficiency loss at resonance.

A mutual coupling tuning design for slot antennas was developed, along with a transmission line model of the structure. This design expands previous knowledge about tuning mutual coupling between static patch antennas to arrays of tunable slot antennas, allowing

for more diversity in design while maintaining the ability to tune an array's mutual coupling. Using the model, it will be possible to characterize the behavior of the structure and apply it both the this tunable slot array as well as other tunable slot array applications.

6.2 Conclusions

In this thesis, a coplanar waveguide to slotline transition for use in tunable slot applications was developed, then miniaturized. This transition used a straightline design and a radial stub, but other stub shapes were shown to work as well, enabling flexibility in stub construction, including meandering of the perimeter to reduce stub size. Analysis was done to explain the loss in the transition, finding that it was caused by radiation of the structure due to common mode currents. Several stub shapes were also investigated for performance, including those with different perimeters to investigate the effects of meandering.

Several tunable slot antenna designs were simulated and information was gathered from their performances. The end loaded slot exhibited full S-band tuning, but faced similar issues with nulls in radiation efficiency at the resonance of the antenna as the previous end loaded design. The center loaded slot did not have these efficiency issues, but had a small tuning range. The side loaded design exhibited 1.4 GHz of tuning without radiation efficiency dips at resonance, showing promise for future development into an antenna capable of full S-band tuning.

A design for tuning the mutual coupling in both static and tunable slot antenna arrays was developed that utilized direct coupling through slotline to try to cancel out the mutual coupling between two slots. The design was capable of creating mutual coupling nulls across S-band, as well as being able to place them at the resonance of the array. This enabled some mutual coupling tuning on its own, but a transmission line model of the structure was developed to enable further study of its behavior.

6.3 Future Work

The next steps for the coplanar waveguide to slotline transition stub reduction are to investigate the lower limits of stub size that can support a successful transition, as well as investigation in expanding this idea into other transition structures that rely on stubs to act as baluns between transmission lines.

The tunable antenna designs need to be investigated further to see if larger tuning bands can be developed. The microstrip-loaded slot has the most promising tuning capabilities, and expanding the tuning range to cover the full S-band would allow for implementation of the cavity loading structures as tuning mechanisms for the slot.

The mutual coupling tuning mechanism has shown promise in reducing the mutual coupling between two tunable antennas, but the reductions are rather small at this point, with a small bandwidth of about 85 MHz for -3 dB of cancellation. The transmission line model needs to be used to determine proper values for capacitances and slotline dimensions in order to get as much mutual coupling cancellation as possible. There is also potential for separation of the nulls and peaks in mutual coupling, potentially leading to further refinement and ability from the model.

References

[1] F. C. Commission *et al.*, *United states frequency allocations*, 2003.

[2] L. Szolc, T. Poydence, and J. Ruyle, "Frequency-agile ring resonator end-loaded slot antenna", *Microwave and Optical Technology Letters*, vol. 59, no. 8, pp. 1876–1882, 2017.

[3] K. Buisman, C. Huang, A. Akhnoukh, M. Marchetti, L. De Vreede, L. Larson, and L. Nanver, "Varactor topologies for rf adaptivity with improved power handling and linearity", in *2007 IEEE/MTT-S International Microwave Symposium*, IEEE, 2007, pp. 319–322.

[4] S. Saeedi, J. Lee, and H. Sigmarsson, "Prediction of power handling in tunable, high-q, substrate-integrated, evanescent-mode cavity bandpass filters", *Electronics Letters*, vol. 52, no. 10, pp. 846–848, 2016.

[5] S. Moon, H. H. Sigmarsson, H. Joshi, and W. J. Chappell, "Substrate integrated evanescent-mode cavity filter with a 3.5 to 1 tuning ratio", *IEEE Microwave and Wireless Components Letters*, vol. 20, no. 8, pp. 450–452, 2010.

[6] S. Saeedi, S. Atash-Bahar, J. Lee, and H. Sigmarsson, "Control system for piezoelectric-actuator-based tunable evanescent-mode cavity microwave filters", *IEEE Transactions on Components, Packaging and Manufacturing Technology*, vol. 8, no. 11, pp. 1979–1989, 2018.

[7] P. Winniford, A. Schaeffer, J. Kennedy, S. Saeedi, C. Fulton, N. Goodman, H. Sigmarsson, and J. Ruyle, "Investigation of a tunable antenna for high-power phased array applications", in *Proceedings of the Allerton Antenna Conference, September 20, 2018*, Allerton Antenna Applications Symposium, 2018.

[8] H. G. Booker, "Slot aerials and their relation to complementary wire aerials (babinet's principle)", *Journal of the Institution of Electrical Engineers-Part IIIA: Radiolocation*, vol. 93, no. 4, pp. 620–626, 1946.

[9] C. A. Balanis, *Antenna theory: analysis and design*. Wiley-Interscience, 2005.

[10] H. Joshi, H. H. Sigmarsson, S. Moon, D. Peroulis, and W. J. Chappell, "High-q fully reconfigurable tunable bandpass filters", *IEEE transactions on microwave theory and techniques*, vol. 57, no. 12, pp. 3525–3533, 2009.

[11] T. Q. Ho and S. M. Hart, "A broad-band coplanar waveguide to slot line transition", Naval Command Control, Ocean Surveillance Center RDT, and E Division San Diego CA, Tech. Rep., 1992.

[12] Y. Li, Z. Zhang, W. Chen, and Z. Feng, "Polarization reconfigurable slot antenna with a novel compact cpw-to-slotline transition for wlan application", *IEEE Antennas and Wireless Propagation Letters*, vol. 9, pp. 252–255, 2010.

[13] M. Al Salameh, Y. M. Antar, and G. Seguin, "Coplanar-waveguide-fed slot-coupled rectangular dielectric resonator antenna", *IEEE Transactions on Antennas and Propagation*, vol. 50, no. 10, pp. 1415–1419, 2002.

[14] A. T. Wegener and W. J. Chappell, "High isolation in antenna arrays for simultaneous transmit and receive", in *2013 IEEE International Symposium on Phased Array Systems and Technology*, IEEE, 2013, pp. 593–597.

[15] ——, "Coupled antenna scheme using filter design techniques and tunable resonators to show simultaneous transmit and receive", in *2013 IEEE MTT-S International Microwave Symposium Digest (MTT)*, IEEE, 2013, pp. 1–4.

[16] C.-H. Ho, L. Fan, and K. Chang, "New uniplanar coplanar waveguide hybrid-ring couplers and magic-t's", *IEEE Transactions on Microwave Theory and Techniques*, vol. 42, no. 12, pp. 2440–2448, 1994.

[17] K. Fujisawa, "General treatment of klystron resonant cavities", *IRE transactions on microwave theory and techniques*, vol. 6, no. 4, pp. 344–358, 1958.

[18] P. Winniford, "A high-efficiency design for a resonator loaded slot antenna", in *Proceedings of the Allerton Antenna Conference, September 18, 2019*, Allerton Antenna Applications Symposium, 2019.

[19] S. Sierra-Garcia and J.-J. Laurin, "Study of a cpw inductively coupled slot antenna", *IEEE Transactions on Antennas and Propagation*, vol. 47, no. 1, pp. 58–64, 1999.

[20] M. Thibodeau, "Frequency tunable slot antenna by piezo-actuated capacitive loading", in *Proceedings of the Allerton Antenna Conference, September 18, 2019*, Allerton Antenna Applications Symposium, 2019.

[21] J. L. Allen and B. Diamond, “Mutual coupling in array antennas”, Massachusetts Institute of Technology Lincoln Lab, Tech. Rep., 1966.

[22] D. Pozar and D. Schaubert, “Scan blindness in infinite phased arrays of printed dipoles”, *IEEE Transactions on Antennas and Propagation*, vol. 32, no. 6, pp. 602–610, 1984.

[23] S. B. Cohn, “Slot line on a dielectric substrate”, *IEEE Transactions on Microwave Theory and Techniques*, vol. 17, no. 10, pp. 768–778, 1969.

[24] R. Simons and R. Arora, “Double-slot fin-line structure for millimeter wave applications”, *Proceedings of the IEEE*, vol. 67, no. 8, pp. 1159–1160, 1979.

[25] D. Pozar, “Microwave engineering, 3rd, 2005”, *Cited on*, p. 105,

[26] P. Winniford, “Analytical matrix method to analyze multiline transmission line structures”, Master’s thesis, University of Oklahoma, 2015.

[27] J. Ruyle and J. T. Bernhard, “Signal flow graph for a probe-fed microstrip patch antenna”, *IEEE Antennas and Wireless Propagation Letters*, vol. 8, pp. 935–938, 2009.

[28] H. Akhavan and D. Mirshekar-Syahkal, “Approximate model for microstrip fed slot antennas”, *Electronics Letters*, vol. 30, no. 23, pp. 1902–1903, 1994.

[29] B. K. Nauwelaers and A. R. Van De Capelle, “Integrals for the mutual coupling between dipoles or between slots: With or without complex conjugate?”, *IEEE transactions on Antennas and Propagation*, vol. 36, no. 10, pp. 1375–1381, 1988.

[30] S. F. Bass, “Investigation of a frequency and pattern reconfigurable slot array utilizing ring resonator end loads”, Master’s thesis, University of Oklahoma, 2017.